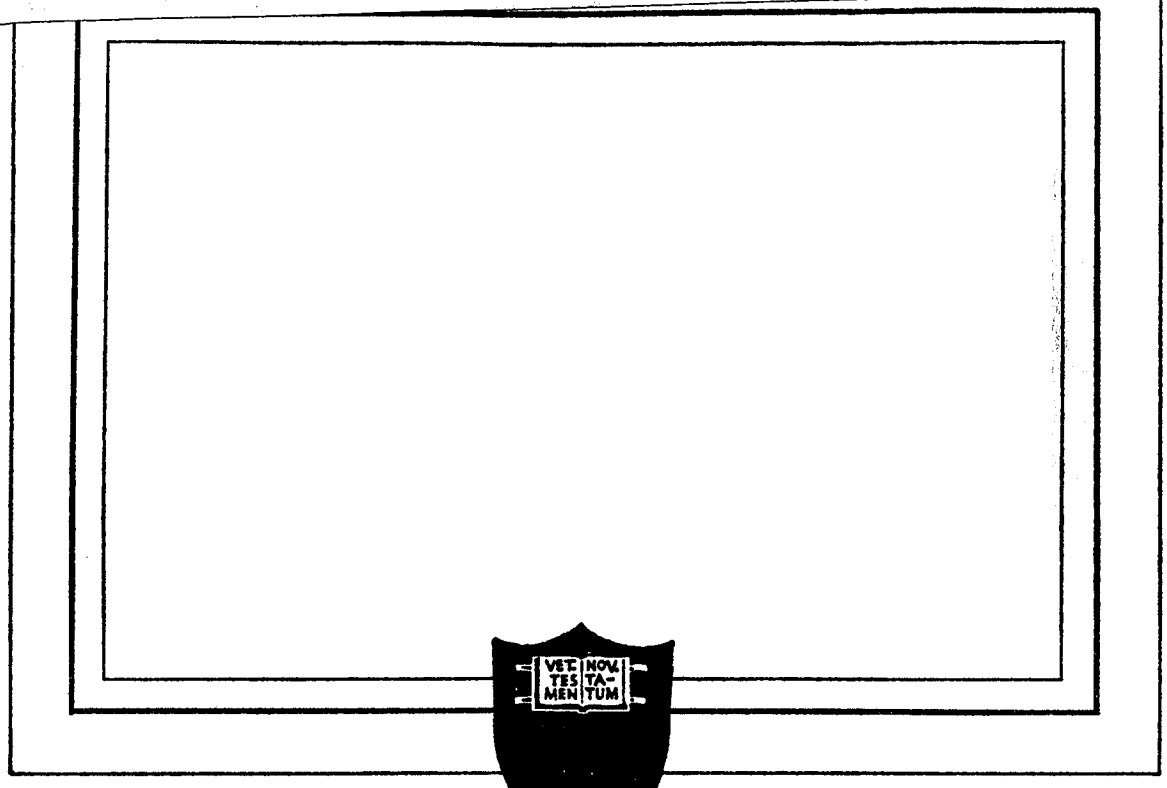

PRINCETON UNIVERSITY

DEPARTMENT OF

AEROSPACE AND MECHANICAL SCIENCES

NASA Research Grant NGL-31-001-005

Prepared for
National Aeronautics
and Space Administration

MASS, MOMENTUM AND ENERGY FLOW

FROM

AN MPD ACCELERATOR

Report 999

Prepared by John S. Cory
John S. Cory

Approved by R. G. Jahn
Robert G. Jahn
Professor of Aerospace Sciences,
Dean of Engineering
and Research Leader

*This report is a reproduction in entirety of the Ph.D. dissertation of Mr. John S. Cory. It is submitted to the sponsor and to the distribution list in this form both as a presentation of the technical material, and as an indication of the academic program supported by this Grant.

September 1971

School of Engineering and Applied Science
Department of Aerospace and Mechanical Sciences
Guggenheim Aerospace Propulsion Laboratories
PRINCETON UNIVERSITY
Princeton, New Jersey

ABSTRACT

The mass, momentum, and energy flows through a quasi-steady, self-field MPD accelerator are measured over a current range of 8 to 50 kiloamperes and inlet mass flows of 2 to 36 grams per second of argon. Time-resolved arc chamber pressure and impact pressure in the exhaust jet, measured with a piezoelectric pressure probe capable of operation with a flat response from 1 to 140 kilocycles, are used to calculate the momentum flux profiles, the gas-dynamic contribution to thrust, and the total thrust. The momentum flux profile indicates that the accelerator produces a uniform, 2-inch diameter axial jet at the anode which expands into a Gaussian profile at an axial station 11 inches from the anode. The electromagnetic component of the thrust is found to follow the familiar quadratic dependence on arc current, while a more complex empirical relation is needed to correlate the gasdynamic contribution with the current and mass flow rate. Using available time-of-flight velocity profiles at a current of 16 kiloamperes and a mass flow of 5.9 grams per second, calculated flux profiles of mass and kinetic energy exhibit a tendency for some fraction of the inlet mass flow to leak out at a low velocity around the central high velocity core. Discharge chamber geometry changes to eliminate the leakage will doubtless improve the arc performance.

TABLE OF CONTENTS

LIST OF ILLUSTRATIONS

TABLES

CHAPTER 1

INTRODUCTION

Experimental investigations of the operation of plasma accelerators can be divided into two classifications. In one, the accelerator is treated as a black box, and the output thrust is measured as a function of the input mass flow rate and the electrical power. This information is then used to calculate the thruster performance (Ref. 1-1). In the second type of investigation, the detailed structure of the electrical fields, magnetic fields and the thermodynamic state of the plasma are measured as a function of the input mass and energy and also as a function of time and position in the acceleration region. This more detailed information is used to study the acceleration processes and losses in the plasma accelerator (Ref. 1-2). Both types of investigation have a common goal, the development of improved thrusters, but until recently, neither has been of much help to the other in achieving that goal.

The reason for this division has been the rapid evolution of plasma accelerators and their theory and measurement techniques. Each individual laboratory investigated its own unique operating conditions and accelerator geometry (eg. "T" gun, Faraday accelerator or Hall thruster) (Ref. 1-3,4,5,6). Theoretical understanding of accelerator operation was insufficient to allow reasonable comparisons of the widely disparate results, and frequently the measurement techniques were later found to be incorrect. Progress in finding better thruster geometries was rapid, and those who concentrated on improved detailed diagnostics and theoretical models were furnished with new geometries faster than they could be analyzed. At the same time, those who measured performance, and then went on to a new geometry found the cut and try method was much more successful and faster than relying on suggestions from the

analytically inclined laboratories. This led naturally to a deep division between the two types of experimental investigations of plasma accelerators.

The pace of change has slowed considerably since the invention of the MPD accelerator in 1964 (Ref. 1-7). Most of the work on alternate geometries has been dropped. One of the three forms of the MPD accelerator (steady-state applied field, steady-state self field and pulsed self field, (Ref. 1-8) are studied in most plasma accelerator laboratories. No other radically different geometry or set of operating conditions has been found that provides a major improvement in performance. The emphasis has shifted to relatively minor geometry changes, such as the hollow cathode (Ref. 1-9), or to the search for the optimum value of operating parameters such as applied field strength or current-to-mass flow rate ratio (Ref. 1-10). This has also allowed the more analytically inclined investigators to make an increased contribution to plasma accelerator development, since further improvements must be based firmly on validated experimental measurements. The division between the two types of experimental investigations is becoming less pronounced.

The investigation described in the following chapters is a continuation of this process. Clark (Ref. 1-11), Turchi (Ref. 1-12) and Oberth (Ref. 1-13) have measured the detailed structure of the electric and magnetic fields in the acceleration region of the Princeton MPD accelerator and used this information to study acceleration processes and losses. On this same accelerator, Clark (Ref. 1-11) has also measured input mass flow rates and electrical power to the accelerator and in addition, time-of-flight velocity profiles were obtained (Ref. 1-14) in the exhaust plume. The present investigation was designed to augment this information by providing a detailed picture of the mass, momentum and kinetic energy flow to and from the accelerator. This information, coupled with the detailed picture of the acceleration region, brings us one step nearer the goal of the analytical type investigation:

gaining sufficient understanding of MPD acceleration so that improved thrusters can be built. At the same time, the new knowledge of the momentum flux can be used to calculate thrust. This completes the set of measurements required and used to evaluate performance: that is, thrust, inlet mass flow rate and electrical power. The investigations described in the following chapters, therefore, provide a link between the performance and analytical types of investigation.

The specific approach for determining mass, momentum and energy flow was determined from a control volume analysis. For the steady state time period (Ref. 1-11), a control volume enclosing the entire acceleration region contains a constant amount of mass, momentum and energy. During this time, therefore, the inlet and exit mass and energy flow rates must be equal and the surface and volume forces on the plasma must equal the rate at which momentum leaves the control volume. The dominant contributions to mass, momentum and energy input to and output from the control volume were estimated, and the measurements to be taken were selected to complete the picture.

Figure 1-1 shows the control volume selected and the best estimate as to the dominant contributions to inlet and outlet mass, momentum and energy. The control volume was selected to make a mass, momentum and energy balance as easy as possible. Its surface coincides with the electrode and insulator surfaces in the acceleration chamber and extends downstream sufficiently far so that all plasma currents are included and far enough to the sides to include the expanding plasma plume. With this control volume, there are no surface forces or flux through the sides of the volume and the entire $\vec{j} \times \vec{B}$ body forces and I V electrical energy is contained in the volume.

The mass balance over this control volume was assumed to be dominated by argon mass flow supplied to the chamber and the mass flux in the accelerated jet. Ablated mass

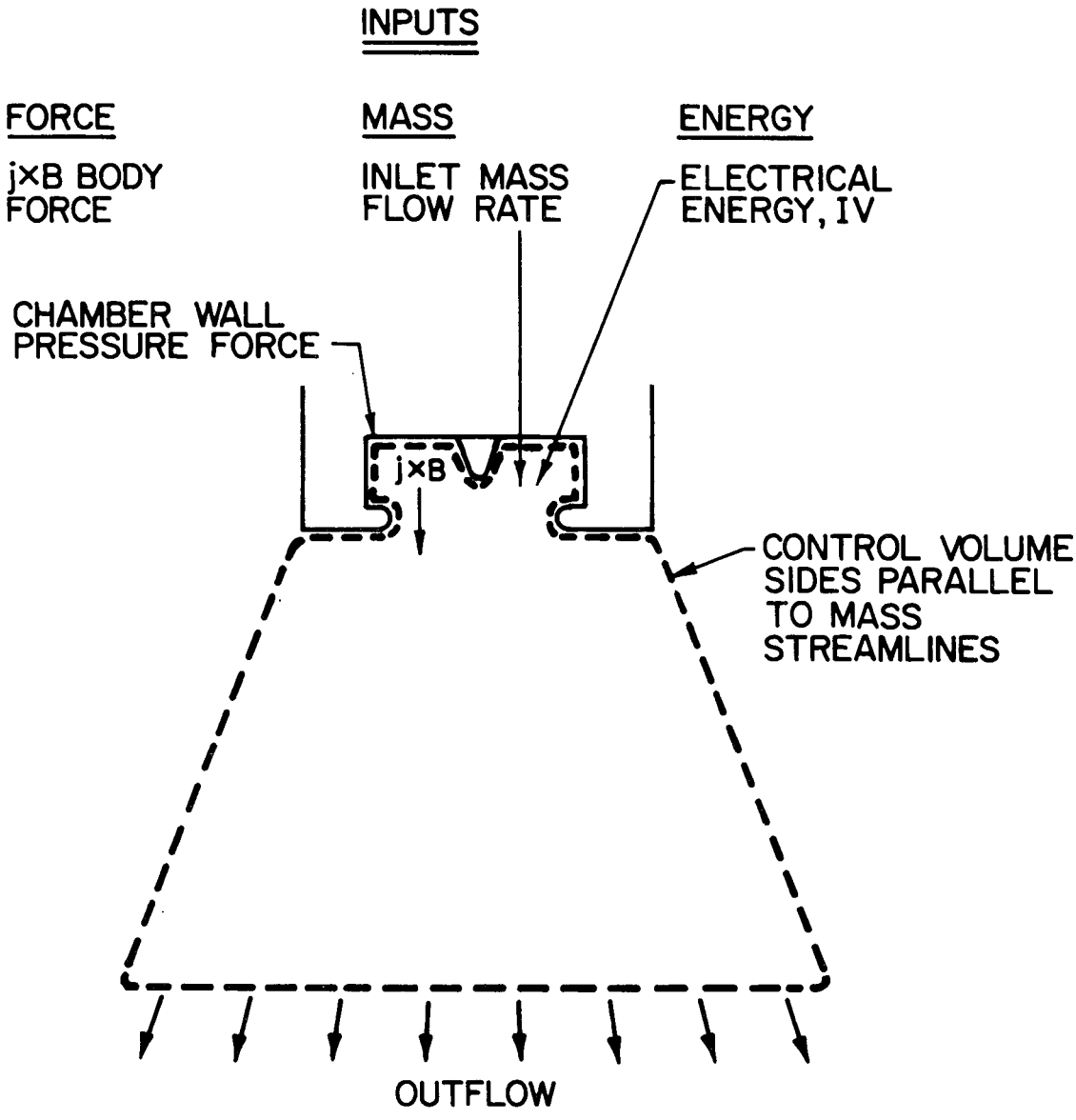

CONTROL VOLUME

FIGURE 1-1

AP25-4750

was assumed to be negligible. Clark (Ref. 1-11) obtained approximate values for the inlet argon flow (hereafter referred to as "nominal" mass flow rate) so only the mass flow in the jet was required to complete the mass balance. This mass balance was expected to show any errors in the "nominal" inlet flow or ablative mass (but did not because of mass leakage).

The principal axial force accelerating the plasma was assumed to be the $\vec{j} \times \vec{B}$ body force producing a net axial momentum flux in the exhaust plume. Since the field studies (Ref. 1-11) showed axial symmetry, the $\vec{j} \times \vec{B}$ contribution could be calculated (Ref. 1-8). Surface forces were assumed to be small except possibly for the axial pressure force exerted by the rear chamber wall on the plasma. In arc jets, the evolutionary ancestor of the MPD accelerator, this surface force was much greater than the integrated $\vec{j} \times \vec{B}$ body force and there is still some debate as to the relative contribution of these two forces. Therefore, to achieve a momentum balance over the control volume (and incidently thrust), it is necessary to measure the momentum flow out of the downstream face of the control volume and also the upstream surface force (or gasdynamic contribution).

The principal energy flow into and out of the control volume were assumed to be the input electrical power, I V (Ref. 1-11), the cathode and anode losses (Ref. 1-12,13), and the kinetic and internal energy flows out of the downstream face of the control volume. The first three have been measured so if the kinetic and thermodynamic flux can be determined, an energy balance can be made.

To complete a mass, momentum and energy balance, therefore, measurements of the exit flux of these quantities plus the electrothermal thrust are required. Measurements of other dominant terms were already available. The outflow quantities to be measured are listed at the bottom of Fig. 1-1 and it is apparent that measurement of two properties, velocity and density would be sufficient to determine most of the outflow quantities.

Since velocity profiles were already available (Ref. 1-14), only three additional measurements were required. These were: 1) electrothermal thrust; 2) frozen flow power, and 3) some quantity related to the density at the downstream face of the control volume. It was decided to neglect frozen flow power and concentrate on developing and using a diagnostic tool for measuring the other two quantities.

The diagnostic tool selected for development was a pressure probe. This development of a probe satisfying the environmental, sensitivity, time response and accuracy requirements, represents one of the major contributions of this investigation. This development is described in Chapter 2. The probe was used to provide a measurement of the electrothermal contribution of thrust by determining the plasma pressure in the acceleration chamber. The surface force on the plasma was then determined by multiplying this pressure times the surface area over which it acts. This use of the pressure probe and the results obtained are described in Chapter 4. The same probe could also be used to determine the flux of momentum, mass and kinetic energy from the downstream face of the control volume. Used as the pressure sensor in an impact (pitot) probe, the quantity ρu^2 could be measured as a function of radial position. By integrating over the downstream face of the control volume, the momentum flow (or total thrust) can be calculated. This use of the pressure probe and the results of the measurements are given in Chapter 3. The impact pressure, ρu^2, can be combined with the available velocity profile data to calculate the mass flux, ρu, and kinetic energy flux, $\frac{1}{2}\rho u^3$. In Chapter 5, the results of these calculations are presented, a mass, momentum and energy balance around the control volume discussed and an MPD thruster development program suggested based on this new information.

The investigation described in the following chapters lived up to expectations. The new information is significant: not only providing an improved understanding of MPD accelerators,

but also offering a new method of measuring performance which should improve communication between the performance and analytical type of investigations.

CHAPTER 2
EXPERIMENTAL APPARATUS

2.1 MPD Accelerator

The facility used to simulate a pulsed, self field, MPD electric thruster is described in detail in Refs. 2-1 and 2-2. This device accelerates a slug of gas through an MPD arc to form a limited duration, but steady flow (after the initial transient) exhaust plume which is the subject of the present study. A schematic diagram of the facility is shown in Fig. 2-1. The elements of this facility which are of particular interest are 1) the cylindrical discharge chamber (Fig. 2-2), consisting of a 3/4 inch conical tungsten cathode, an aluminum anode with a 4 inch orifice and a 2x5 inch ID Pyrex chamber wall; 2) the mass injection system (Fig. 2-3), consisting of the driver and driven sections of a vacuum shock tube and three sets of six calibrated orifices for injecting argon into the chamber at nominal rates of 1.9, 3.8, 5.9, 23, or 36 grams per second; 3) the 160 kilojoule capacitor bank and network (Fig. 2-4, Refs. 2-2) for providing a nearly square current pulse to the arc; and 4) a 3 ft diameter by 6 ft long Plexiglas vacuum tank (Fig. 2-5) for providing a 10^{-5} torr region into which the exhaust plume may expand without being perturbed by EM fields generated by currents in the tank wall.

The operation sequence of the facility begins with the pressurization of the shock tube driver section to 45 or 30 psig (depending on the mass flow desired, Ref. 2-1, page 122), and charging of the capacitor bank to a voltage from 2 to 6.5 kV, depending on the current desired. The shock tube diaphragm is ruptured and a portion of the resulting pressure wave is first bled into the gas triggered switch and the remainder establishes a pressure reservoir at the end of the driven section (Ref. 2-1, p. 106), which in turn feeds the argon gas into the chamber through the six calibrated orifices. The length of the bleed line to the gas triggered switch is adjusted so that the gas in the switch reaches the Paschen voltage, fires, and transfers the

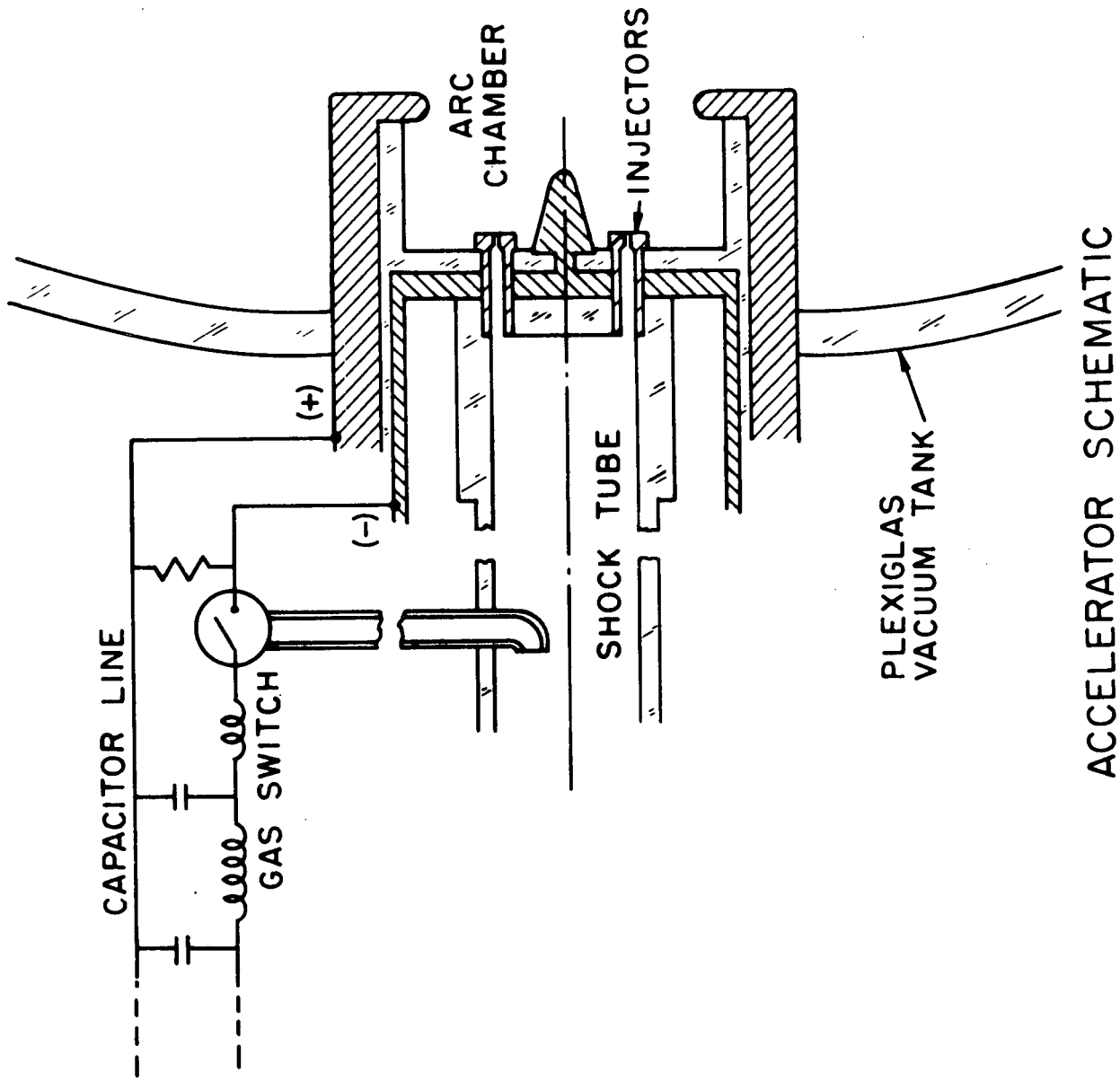

FIGURE 2-1

AP25 · 4558

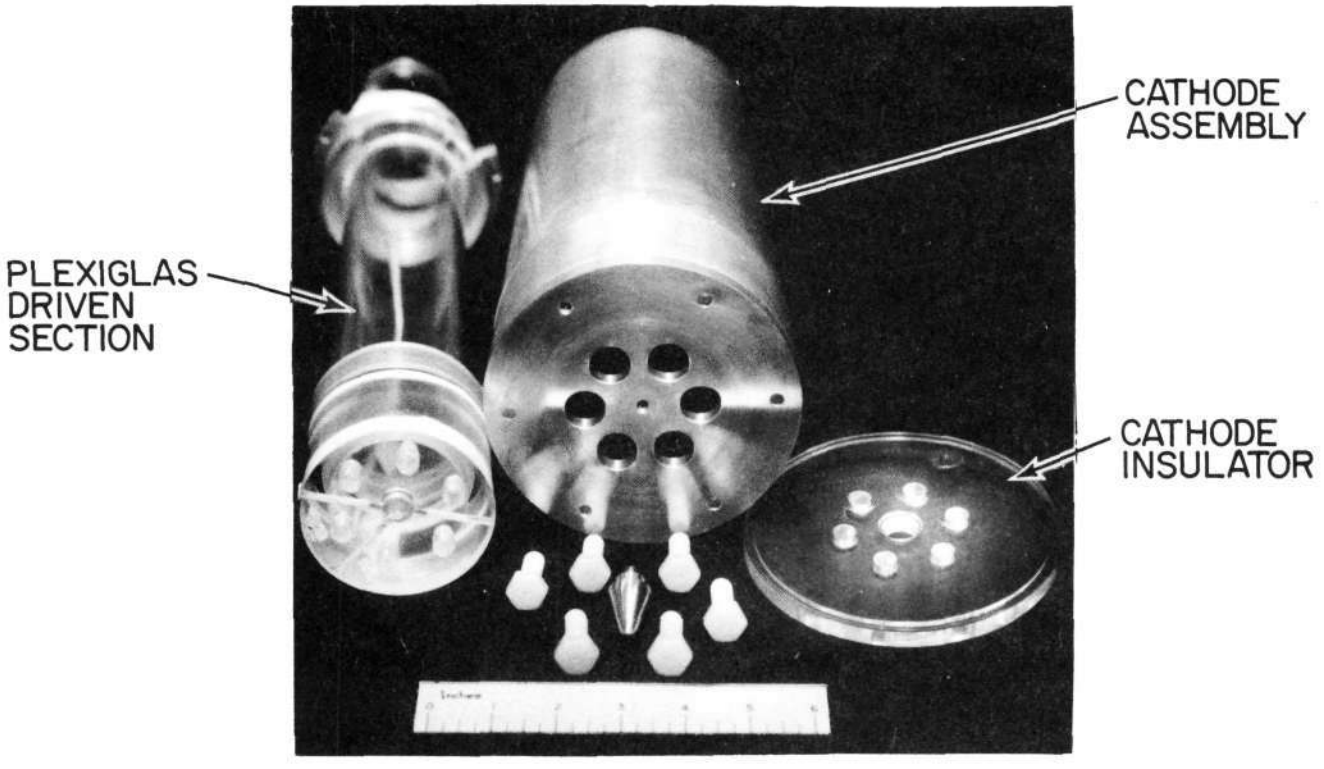

a) EXPLODED VIEW

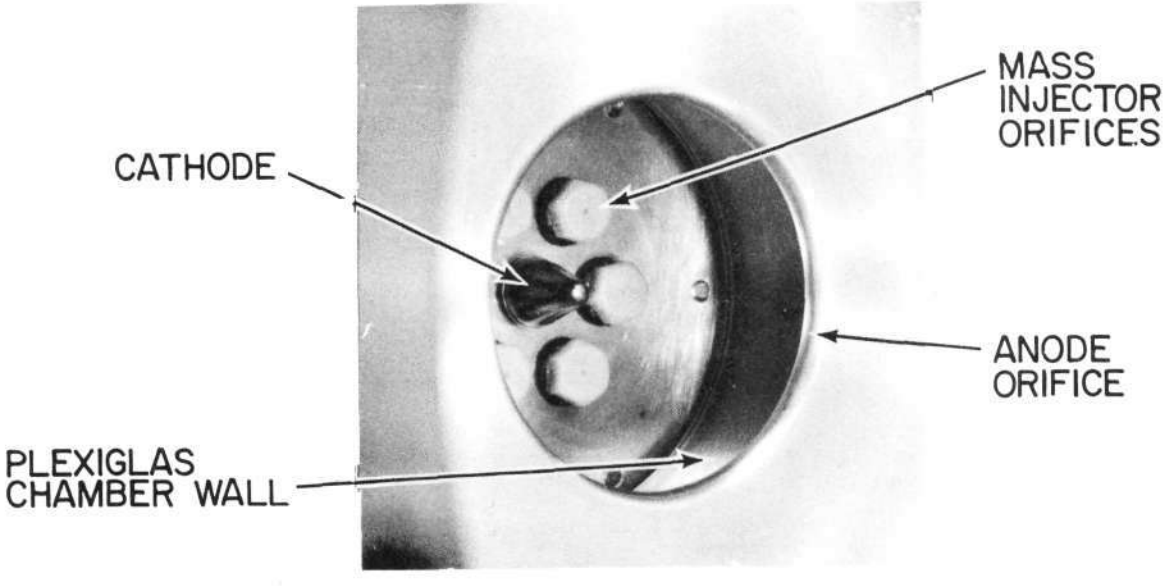

b) PERSPECTIVE VIEW OF ASSEMBLED CHAMBER

MPD ACCELERATOR CHAMBER

FIGURE 2-2

AP25 · P·387

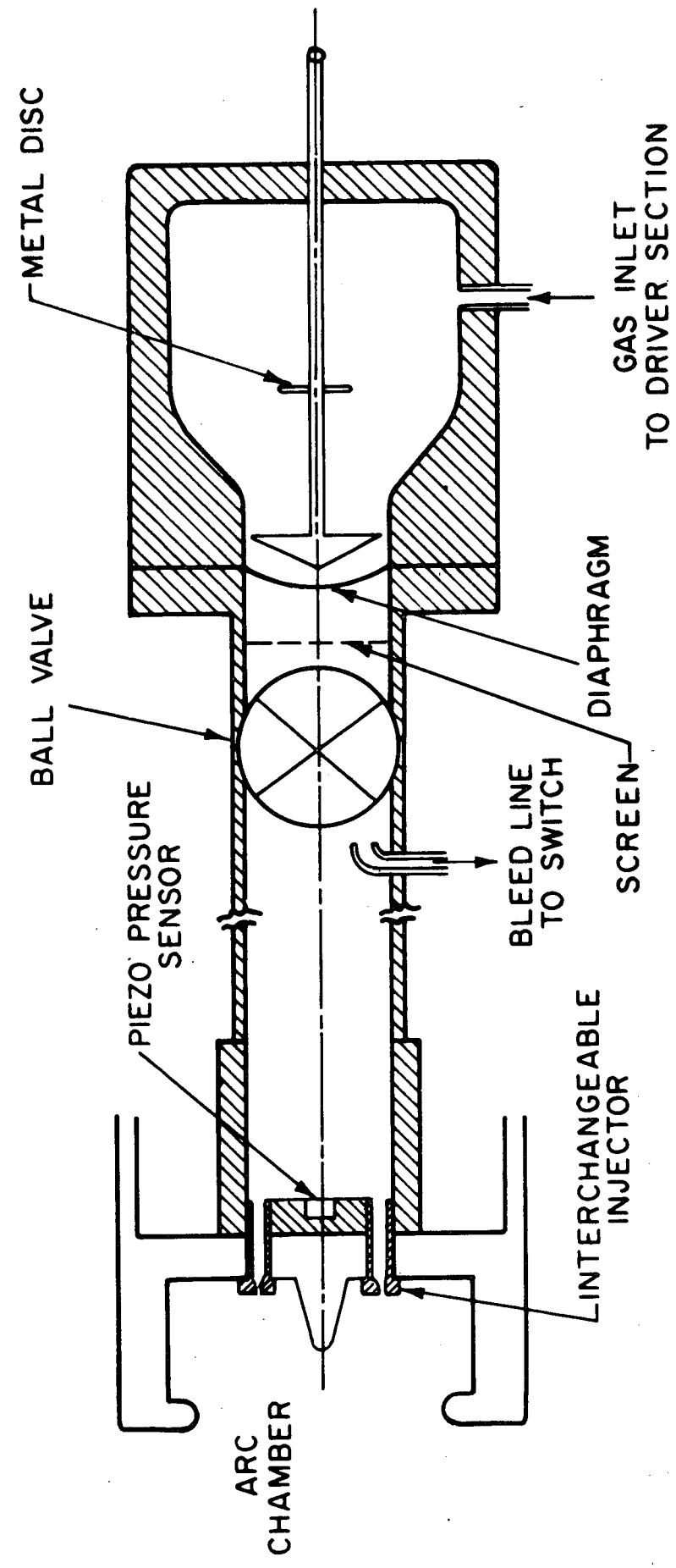

SCHEMATIC OF MASS INJECTION SYSTEM

FIGURE 2-3

AP25·4489

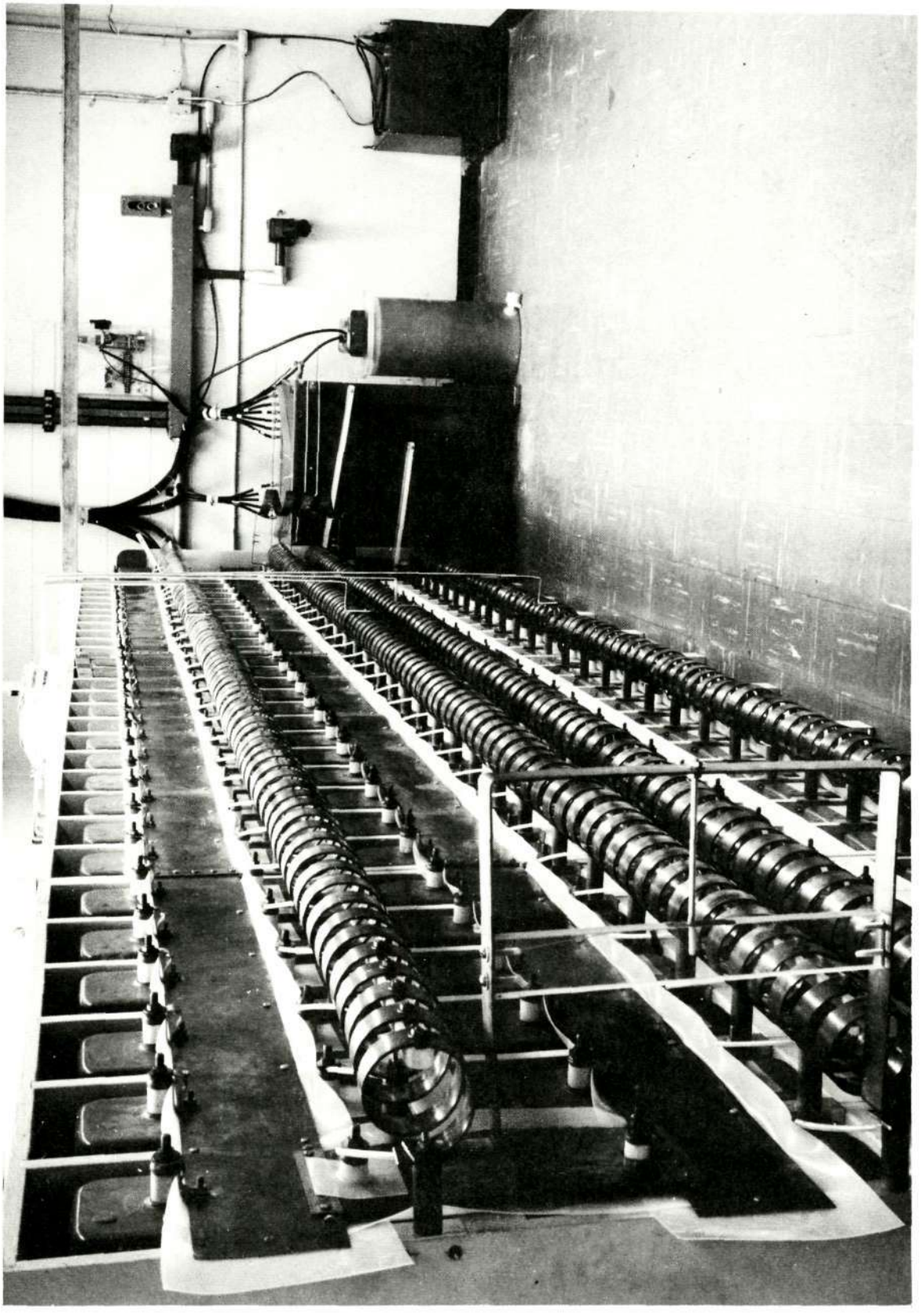

160 KILOJOULE ENERGY STORAGE AND PULSE FORMING NETWORK

FIGURE 2-4
AP25 · P · 388

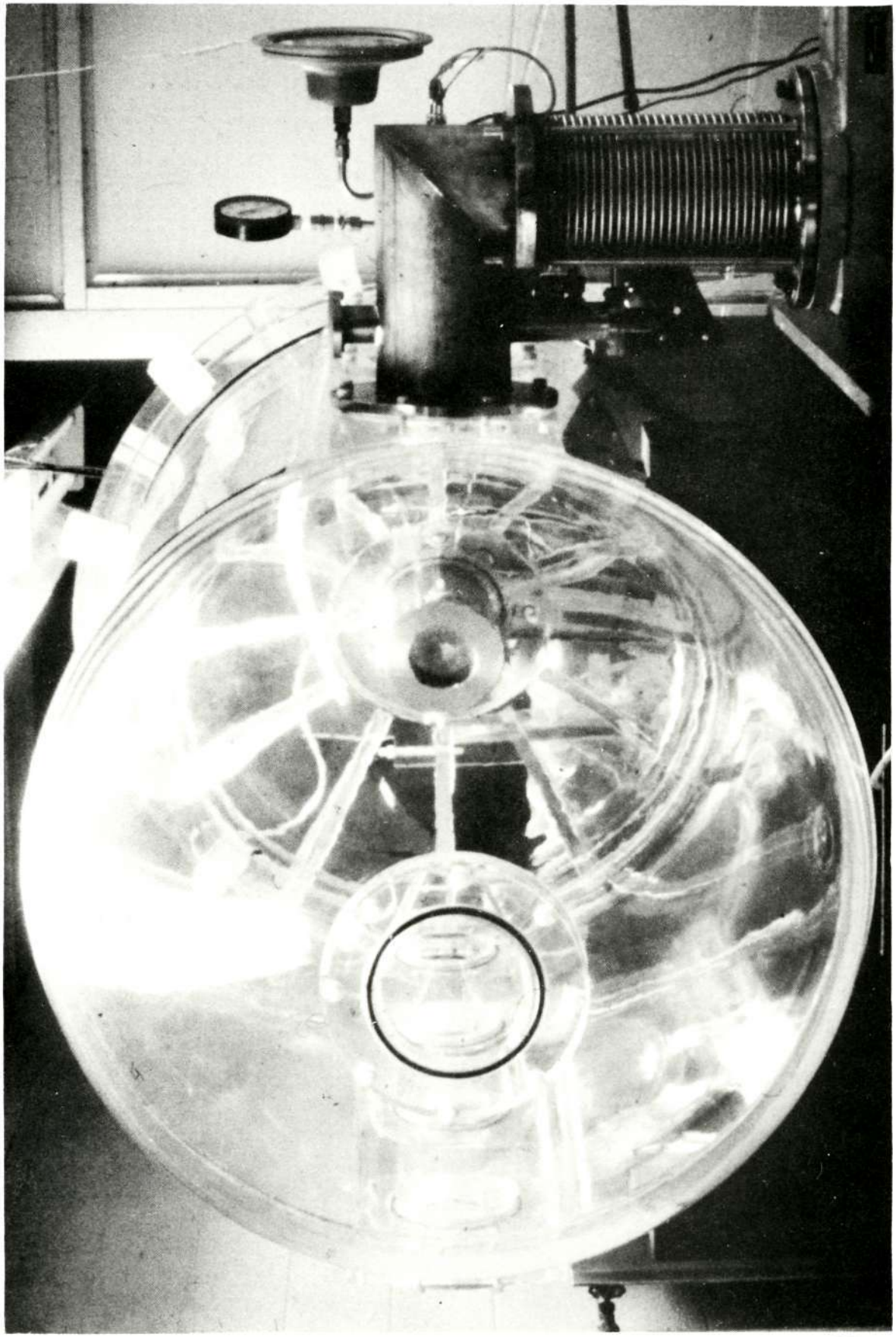

VACUUM SYSTEM CONTAINING MPD ACCELERATOR

FIGURE 2-5
AP25·P·389

capacitor bank potential to the accelerator electrodes only after a steady mass flow has been established in the arc chamber (Ref. 2-1, pp. 118). A coaxially symmetric discharge (Refs. 2-3,2-4) forms in the discharge chamber which, after an initial transient phase, steadily accelerates the incoming gas to form an exhaust plume (Fig. 2-6, Ref. 2-3).

The terminal voltage of the discharge was measured using a Tektronix 6013A high voltage probe in conjunction with a Tektronix 555 oscilloscope. The probe was calibrated with the square wave calibration generator built into the scope. Overall accuracy of $\pm$ 5% is expected (Refs. 2-5,2-1).

The discharge current was measured for each shot using a Rogowsky coil mounted in the anode barrel (Fig. 2-7) and a passive integrator. This coil and integrator were calibrated against a precision current transformer using a 555 oscilloscope to record the voltages from both the Rogowsky coil and the current transformer. The calibration constant was determined to be 1.53 kA/mV, and the accuracy estimated to be $\pm$ 7%.

2.2 Pressure Transducer Design

The requirements for a pressure transducer to measure chamber and jet dynamic pressure in an MPD accelerator are sufficiently stringent that a special design is necessary. The sensitivity, time response, and noise discrimination follow directly from the anticipated signal strengths and duration. Pressures on the order of ten torr are expected, so a sensitivity of about one torr is required, and the noise-equivalent-signal induced in the transducer must not exceed one torr to maintain a reasonable signal-to-noise ratio. Since the pressure is expected to attain a steady value in a few tens of μsec, and retain it for about one msec, it is possible to use an acoustically simple system, where reflected stress waves are held away from the piezoelectric crystal in an acoustic delay line until after the time of interest. The noise level in a pulsed MPD accelerator is very high, and the noise rejection ratio required was found experimentally to be far

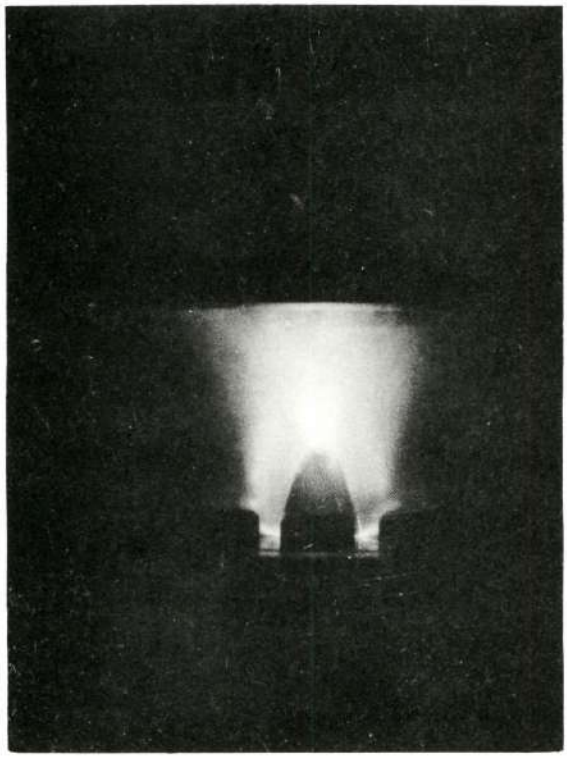

b) DISCHARGE INITIATION t = 13 μsec

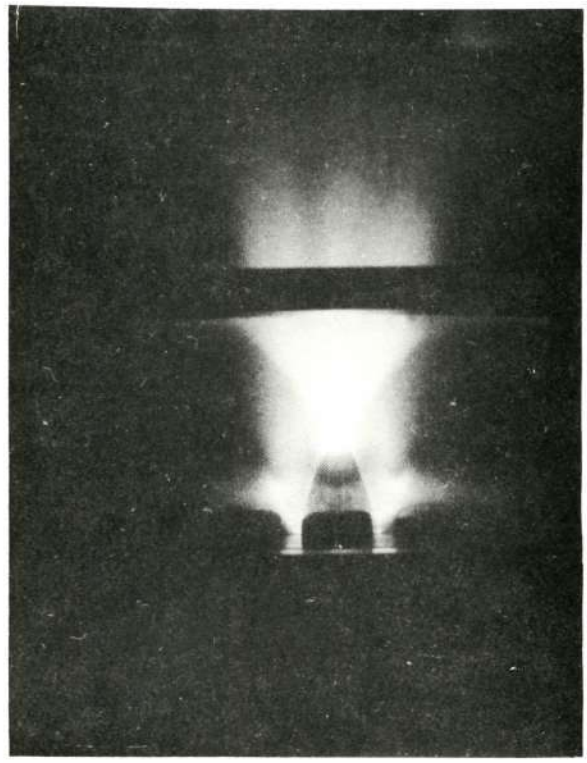

d) QUASI-STEADY OPERATION t = 100 μsec

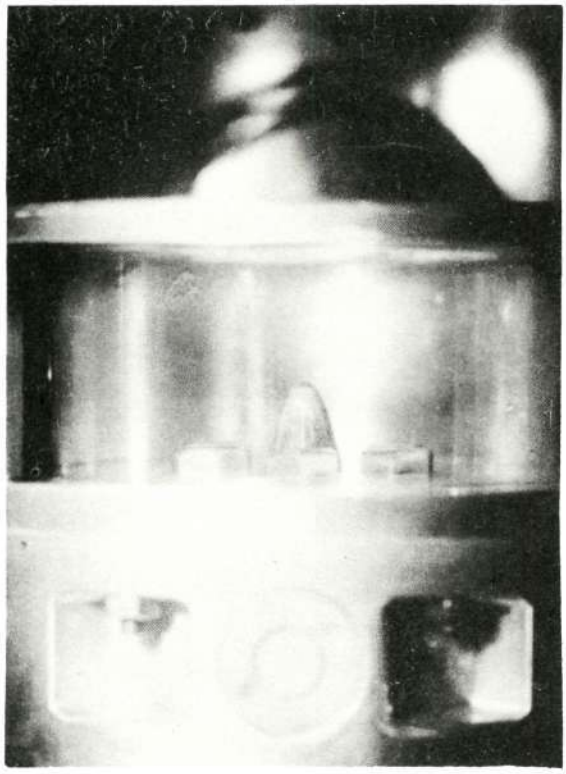

a) ARC CHAMBER THRU SIDEWALL WINDOW

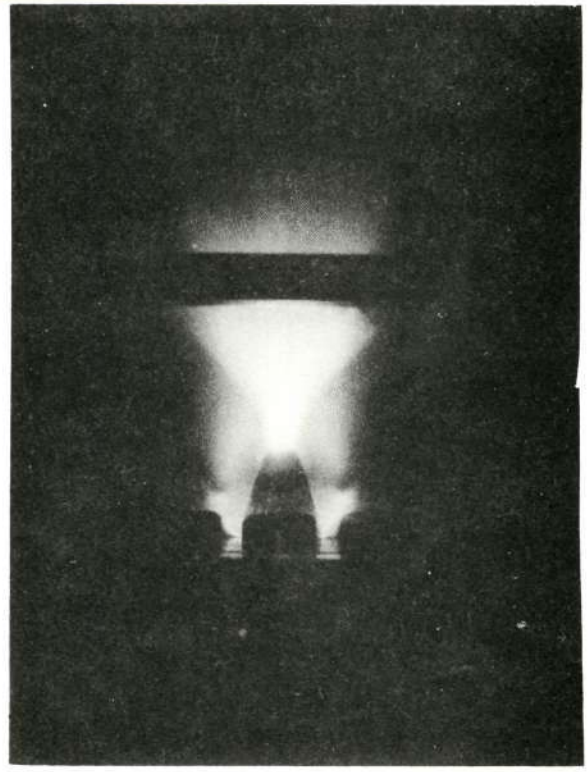

c) DISCHARGE STABILIZATION t = 21 μsec

PHOTOGRAPHS OF MPD ACCELERATOR OPERATION

FIGURE 2-6

AP25 · P · 381

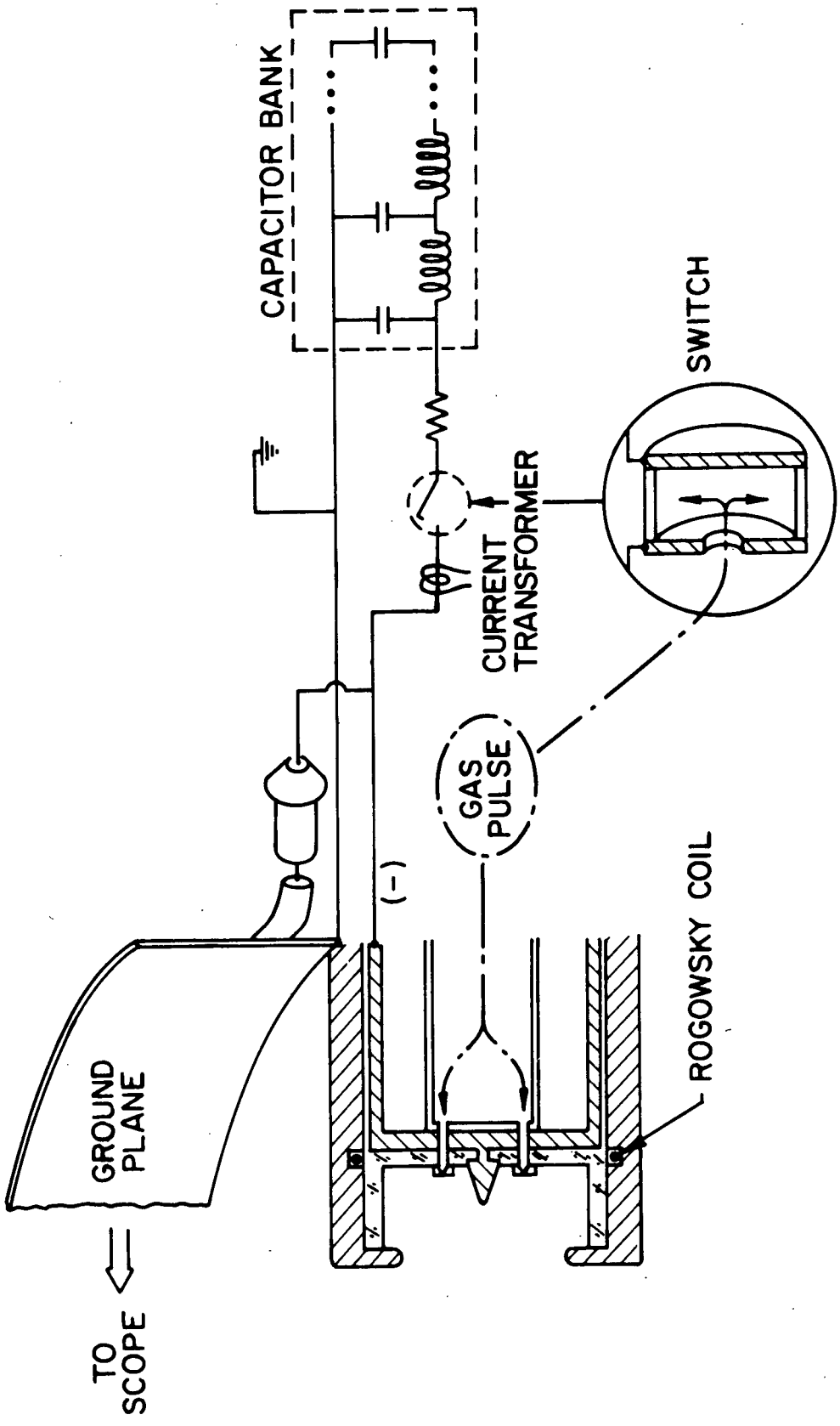

ACCELERATOR ELECTRICAL SCHEMATIC

FIGURE 2-7

AP25-4513

beyond the capability of commercially available transducer systems, so a pressure transducer had to be designed specifically to meet these requirements.

The sensitivity requirement was easiest to satisfy by utilizing a 3/8 inch diameter, well aged, PZT-5, piezoelectric crystal. Since PZT-5 has a piezoelectric constant (d_{33}^E) of about 374 picocoulombs/newton (Ref. 2-6), the crystal output for a given pressure is about:

$$Q = 374 \times 10^{-12} \pi r^2 = 2.68 \times 10^{-14} \text{ coulombs/N/m}^2$$

$$\approx 200{,}000 \text{ electrons/N/m}^2$$

A Kistler Model 565 charge amplifier was used to integrate the piezoelectric output. Using a 500 picofarad feedback capacitor, the output (V) of the charge amplifier fed by the above crystal is:

$$V = \frac{Q}{C} = 5.36 \times 10^{-5} \text{ V/N/m}^2$$

With this sensitivity, a pressure of one torr (133 N/m^2) results in a signal of about 7.13 millivolts, which can be detected and recorded using a 1A7A preamplifier in a Tektronix 555 oscilloscope. This crystal, charge amplifier and oscilloscope easily satisfy the requirement that one torr be detectable.

The noise problem was considerably more difficult to resolve. A study of the noise induced in pressure transducers in the pulsed MPD arc environment was carried out using a Kistler Model 601 and a very fast transducer (Ref. 2-7) available in the lab. Even with these transducers electrically isolated from the plasma, the noise-equivalent signal on a one msec time scale exceeded one atmosphere, compared with the one torr desired. Four major sources of noise were identified. These were:

1. induced EMF from the rapidly changing magnetic fields;
2. capacitively induced charge on one or both of the two electrical leads from the crystal to the charge amplifier;

3. heating of the piezoelectric crystal or its support elements, causing thermally induced strains;
4. and spurious stress waves, principally resulting from internal reflections but also from inadequate acoustical isolation in the transducer mounting.

The induced EMF expected was of the order of 10 volts per centimeter squared. Since the capacitance of the transducer and leads was about 100 picofarads, the induced charge from this source will be on the order of

$$Q \approx 10 \text{ V/cm}^2 \times 100 \text{ pC/V} \approx 10^3 \text{ pC/cm}^2$$

Since the sensitivity to pressure is about 3.6 pC/torr, to keep this source of noise below the equivalent of one torr, the net area linked by the changing magnetic field must be kept to less than 0.3 mm^2. With reasonable care in keeping the electrical leads close together and using coaxial geometry, this can readily be achieved, and the noise from this source in the final design was indetectable.

The magnitude of the electrostatic charge induced across the crystal was not calculated because of the complex geometry. Experimentally, however, it was found very easy to induce a charge of more than 3.6 picocoulombs. After considerable trial and error, it was found that by forming the outer (ground) conductor into a completely closed electrostatic shield around the crystal and the inner conductor, extending this shield back to the charge amplifier, and separating the shield by at least 1/8 inch from the plasma by potting epoxy, the capacitively induced noise from the MPD arc was reduced to a tolerable level. During use of the probe, abrupt appearance of noise usually was caused by failure of one of these two elements. Either the potting epoxy failed and allowed the plasma to get too near the shield, or the shield developed a hole.

Thermally induced strain due to heating of the piezoelectric crystal and its support elements proved to be one of the most difficult noise sources to remove. Although heat transfer is normally characterized by longer time constants, the combination

of high crystal sensitivity to thermally induced strain (about 1000 pC/^{o}K) and the very high plasma temperatures, caused heating to be the major source of noise in the Kistler 601 and York (Ref. 2-7) transducers. The problem was eventually reduced by using a variety of techniques reported in the literature, (Ref. 2-10). The principal steps were to change the design from the Kistler or York models to one involving two rods, each bonded to one face of the crystal, and the crystal edges protected by a thick layer of very elastic material. This design isolated the crystal from the hot plasma until after the time of interest, and used no support structures whose heating and consequent expansion would apply stresses to the crystal. It was found later that it was necessary also to coat the surfaces of the rods and shield the elastic material against radiative heating. Otherwise, the energetic radiation generated by the discharge penetrated the transparent rod and potting materials and rapidly heated the crystal. The steps taken to reduce this radiative heating source of noise were not always successful. Pinholes in the paint coating, reflected radiation and erosion of the opaque coating allowed some radiation to penetrate, especially at the higher current levels. Consequently in the chamber pressure measurements and the dynamic pressure measurements near the discharge, the noise equivalent signal criteria of one torr was not always satisfied.

The two types of acoustic noise were handled separately. Acoustic isolation of the probe from the shock tube, building and vacuum pump noise was achieved by suspending the probe assembly from rubber bands. The pendulum frequency ($\sqrt{g/l}$) of 40 μsec and the tension frequency ($\sqrt{k/M}$) of 20 μsec achieved were sufficiently low to filter out that environmental noise with a frequency comparable to the signal. The low frequency noise which passed through the acoustic filters appeared as a baseline shift which was a nuisance, but tolerable. This degree of isolation from the environment made positioning of the probe difficult, but it was found experimentally to be necessary. "O" ring mountings on the transducer rods, which would have been much more convenient,

were found to produce a noise-equivalent-signal of hundreds of torr.

Internal reflections were minimized by making the probe assembly as near a single, homogenous rod as possible. Complete acoustical homogeniety was impossible since the rod material (Plexiglas), electrical contacts and shielding (copper), piezoelectric crystal (PZT-5) and bonding material (epoxy), all had different acoustic impedances. Similarly the assembly could not be a simple rod since some support for the crystal was necessary, and because of the thermal and electrostatic shielding required on the sides of the crystal. By making the non-rod materials as thin as possible, however, and by taking considerable care to exclude voids which would produce very drastic acoustical impedance mismatches in the bonded surfaces, the assembly was made effectively homogenous for excitation stress frequencies below 10^5 Hz. Similarly, by using a crystal of the same diameter as the rods, using supporting and thermal shielding materials with a very low Youngs modulus, and designing the shield to be very weak, most of the stress was confined to the rod and crystal. To a considerable extent, internal reflections and complex modes were thus avoided and the probe acted as a simple homogenous rod, with only the longitudinal mode excited by the pressure signals.

As mentioned earlier, the pressure signals, after a few tens of μsec of transient behavior, were expected to maintain a steady value for the remainder of the current pulse. To follow this expected signal, the probe assembly was designed to have a rise time of less than 0.1 msec by mounting the crystal 2.0 inches from one end of a 38 inch rod assembly. The stress wave generated by the pressure pulse on the end of the 2 inch stub would require 25 μsec to traverse the 2 inches of Plexiglas rod (acoustic velocity about 2100 m/sec). Any reflections at either crystal surface would have a second chance to enter the crystal after traversing the stub twice in 50 μsec, so the rise time, even with poor coupling between the rod and crystal should be less than 100 μsec. The remaining 36 inch length of Plexiglas rod on the other

face of the crystal provides an acoustic delay line. After the stress wave leaves the crystal, it travels to the free end, is reflected and travels back to reenter the crystal only after about one msec. During the one msec of interest, therefore, the crystal is completely free of reflected stresses and interpretation of the output signal in terms of pressure on the stub end is straightforward. For times longer than one msec, the output is not simply related to the pressure pulse, but this is acceptable since the maximum duration of the MPD current pulse, and consequently any signal of interest is one msec.

Figure 2-8 shows a schematic of the probe assembly constructed according to the above design criteria. The piezsoelectric crystal and shield system is emphasized at the expense of the simpler but much larger Plexiglas rods. Each element in the assembly is identified by an item number which refers to Table 1. Table 1 explains the role of each element in determining the sensitivity, noise and response time of the probe assembly.

2.3 Probe Calibration

To calibrate the pressure probes it is necessary not only to determine the voltage output for a given pressure, but also to make sure that the calibration constant did not depend on the frequency or amplitude of the pressure over the anticipated range. This was accomplished by using four independant calibration techniques and studying the acoustic properties with two excitation techniques. This extensive testing and the many problems identified and solved using these tests during the probe development, served to generate considerable confidence that the calibration constant was valid for the measurements in the plasma.

2.3.1 Acoustic Properties

In the acoustic tests, stress waves were excited in the probe by two devices; a pendulum and a shock wave. The pendulum consisted of an 1/8 inch ball bearing suspended from a 6 inch long thread. In the test, the ball was held about one centimeter from

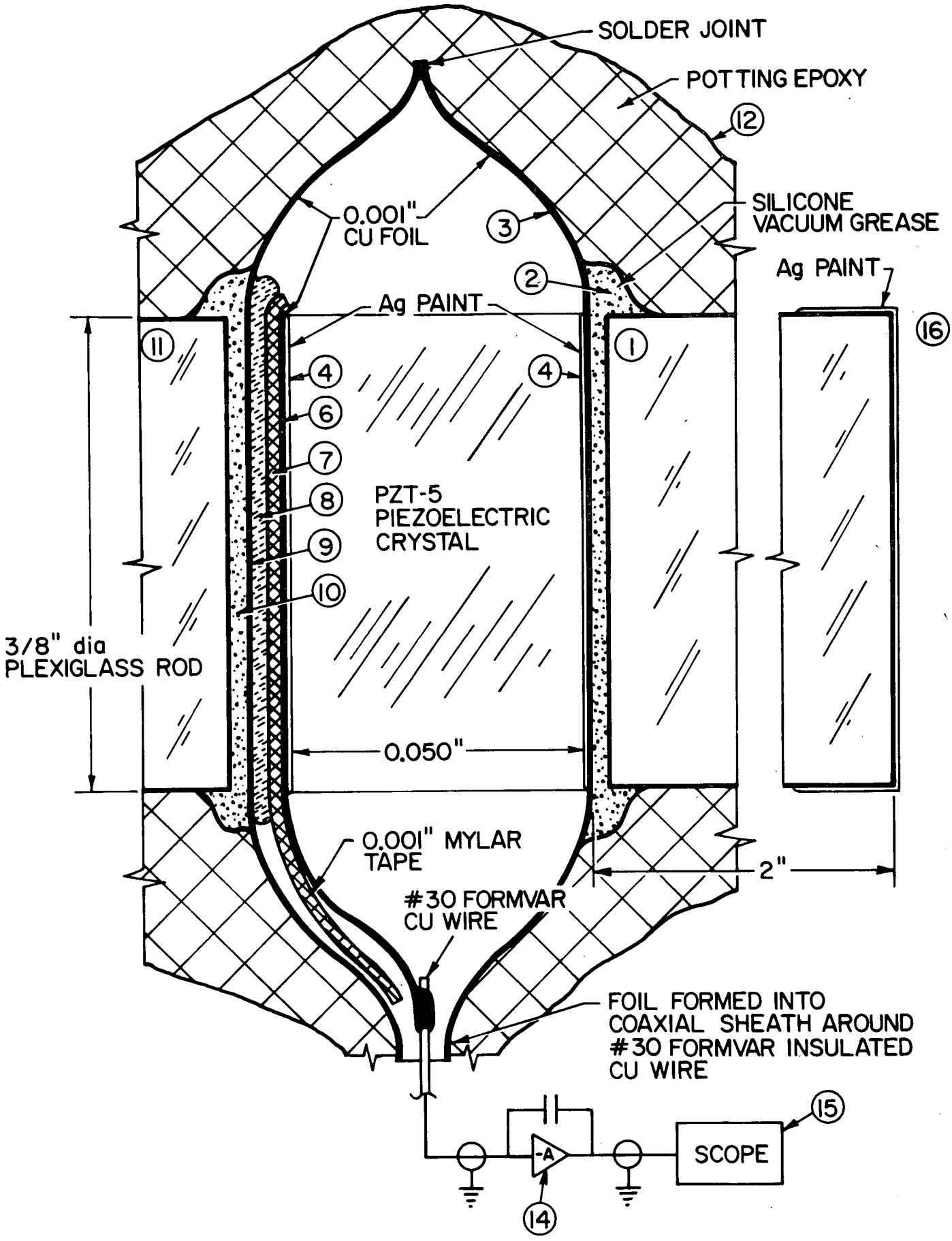

SCHEMATIC OF PRESSURE TRANSDUCER

FIGURE 2-8

AP25·4713

TABLE I

Pressure Transducer Construction

1. 3/8 x 2" Plexiglas stub - This provides thermal and electrical separation of the crystal from the plasma: It is sufficiently long to remove the crystal from the region of strong magnetic fields. It is acoustically simple - only longitudinal stress waves are excited. Its acoustic impedance matches the backing rod.

2. Silicone vacuum grease - This is used to achieve a good (no void) acoustical coupling between the rod and the foil. It is the weakest link in tension, so accidental damage will cause failure here, but the (no void) acoustical match is easily reformed.

3. 0.001" annealed and rolled copper foil - This provides one of the conductors for carrying the induced charge to the charge amplifiers. It also forms part of the gaussian electrostatic shield around the crystal and center conductor.

4. GC Electronics #21-1 silver conducting paint - This provides electrical contact between the tinned surface electrode on the crystal and the Cu Foil. It also provides a no void, acoustical coupling.

5. Piezoelectric (ceramic) crystal, Clevite PZT-5 6050-5 When strained, this crystal induces electric charges on its faces.

6. 0.001"annealed and rolled copper foil - This 3/8 dia. disc conducts the piezo-current from the tinned face of the crystal to the center wire of the coaxial output wire.

Item numbers refer to Fig. 2-8

TABLE I (Cont'd)

7. One mil mylar scotch brand electrical tape - This serves to insulate the #6 copper conductor from the shield (#9). The one sticky surface wets the #6 disc and provides a no void acoustical coupling.

8. Duco 50/50 formula Epoxe - This provides a no void acoustical coupling between the non-sticky side of the mylar tape (#7) and the shield (#9).

9. 0.001 inch annealed and rolled copper foil - This foil, together with #3 forms a Gaussian electrostatic shield completely enclosing the crystal and center conductor. The shield is formed in such a way that stresses tending to compress the crystal will bend the thin foil. This is to insure that almost all of the stress applied deforms and generates a signal from the piezoelectric crystal. The #9 foil is crimped and soldered to the #3 foil all the way around the periphery (except where the center lead penetrates) to form a completely closed shield. It is extended into a foil shield closely wrapped around the Formvar covered center conductor. This shield is then connected all the way around to the outside conductor of a length of RG/58U coaxial cable. At all points the separation between the two conductors is minimized to reduce the area involved in dB/dt noise pick-up.

10. Duco 50/50 formula Epoxe - This provides a no-void acoustic coupling between the shield and the acoustic delay line (#11) and bonds the piezoelectric wafer to the rod.

TABLE 1 (Cont'd)

11. 3/8 dia x 36" Plexiglas rod - This rod accepts the stress wave propagating through the crystal. The stress propagates through the rod in the longitudinal mode, is reflected from the free end, and approximately one msec later reenters the crystal. This rod, therefore, acts as a delay line, keeping reflections from the crystal for the time of interest. By keeping the wafer (#4 thru #10) thin, and maintaining good acoustical coupling throughout the wafer, the #11 and #1 rods are a simple acoustic system for wavelengths larger than the wafer thickness, and the acoustic impedance mismatch between the rods and the various materials in the wafer is unimportant.

12. Emerson and Cumings, Inc. Eccosil 2CN potting epoxy - This material is used to separate the charged plasma from the shield. The large separation reduces the capacitively induced shift in the shield ("ground") potential. It also prevents the conductive plasma from discharging to ground through the shield.

13. AWG #30 Formvar insulated copper wire - This wire provides the center conductor and insulation of a coaxial cable leading to regions of low B field, where conventional RG-58/U cable can be used. This cable is made as thin as possible both to present as little area between conductors as possible to reduce dB/dt noise, and to prevent the cable from supporting any of the stresses (which should be confined to the probe to maintain acoustic simplicity).

14. Charge amplifier, Kistler Model 565, S/N 148 with a 550 pF feed-back capacitor - This amplifier provides an input impedance of about 10^{12} ohms and produces a low impedance output voltage proportional to the input charge. The electronics time constant is about 7 μsec.

TABLE I (Cont'd)

15. Tektronix Model 555 (S/N 00377) dual beam osciloscope with type 21 and 21A time base and type L and type 1A7A amplifier plug-ins, and Hewlett Packard Model 196A polaroid scope camera - This system was used to display and record the voltage (pressure) signals as a function of time.

16. GC Electronics #21-1 silver conducting paint - This was used to prevent the intense light generated in the plasma from passing through the transparent stub (#1) and heating the piezoelectric crystal (#5).

the end of the probe with the string supported from a point directly above the probe face, and then released. The ball would strike the center of the probe face, and rebound after a time (about 50 μsec) determined by the elasticity of the impact and the velocity of the stress waves in the ball. The natural pendulum frequency of the ball was several seconds, so after rebounding the ball remained away from the probe for the duration of the test. The result of this impact was to induce an impulsive stress wave in the probe.

Figure 2-9 shows the voltage output from the piezoelectric crystal resulting from this impulsive stress wave. The dotted line shows the ideal response from a perfectly square stress wave into a perfectly elastic uniform, homogenous rod. The difference between the two traces is a very sensitive indication of the limitations of the probe.

In Fig. 2-9, the curved initial peak is caused by the small contact area and the consequent inelastic and elastic deformations. Using a Plexiglas striker, the peak became much broader, while using a brass cap on the end of the Plexiglas rod produced a much sharper peak. The observed difference between the ideal and real results shows a limitation on the test technique in establishing the probe response time and in using the momentum transferred for an absolute calibration. The deformation of contact surfaces, however, is not important in measuring gas pressure which produces a much lower stress per unit area.

The second small peak shown in Fig. 2-9 is a result of reflection of the stress wave from the Plexiglas - wafer interfaces (Items 2 to 10 in Fig. 2-8). This peak shows the rod is not acoustically homogeneous. The ratio of the amplitudes of these two peaks is only about 10:1, however, indicating that 90% of the stress wave passes through the crystal into the acoustic delay rod on the first try. In terms of probe performance this shows good response of the probe to rapid pressure changes.

The third indication of interest in Fig. 2-9 is the long flat region from 200 μsec to one msec. This shows that by this time

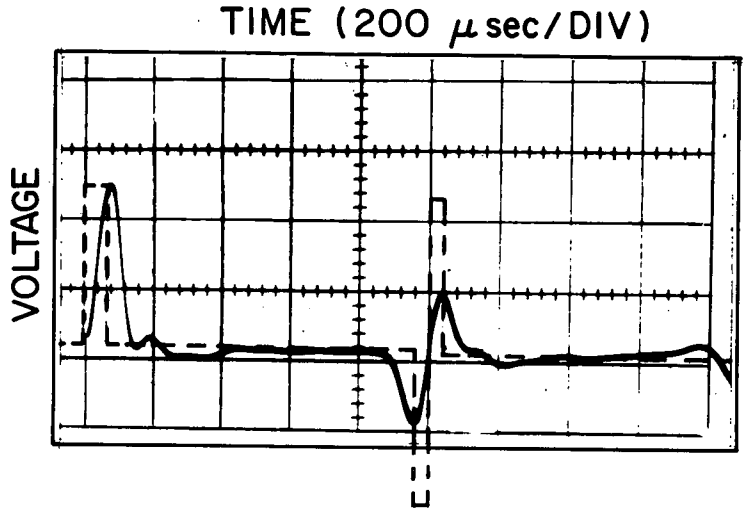

PIEZOELECTRIC VOLTAGE GENERATED BY AN IMPULSIVE STRESS WAVE IN PROBE: ACTUAL (———); IDEAL (– – – – –)

FIGURE 2-9

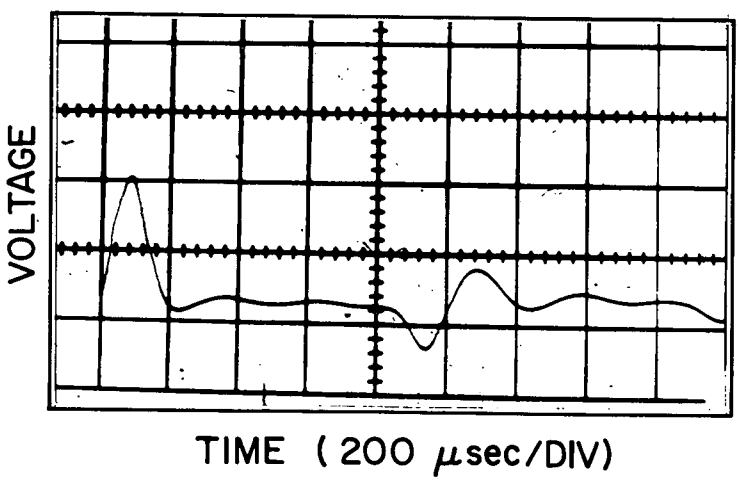

TEST RESPONSE AT COMPLETION OF DATA RUNS

FIGURE 2-10

all detectable stress has propagated into the acoustic delay rod, and also that this rod is not yet generating reflections. (When an "O" ring support or curved delay rod was used, this region of the trace was full of wiggles.) With a one msec square wave input, therefore, the probe would be free of initial transients during this time, and the output voltage a simple indication of the stress level.

The next major feature at about one msec is the returning stress wave echo from the end of the delay rod. Since the end was free, the compression wave (positive voltage) is reflected as a tension wave (negative deflection). This tension wave, as shown in Figure 2-9, has been broadened and attenuated by the non-linear behavior of irregularities at the ends and all surfaces, so before it reaches a maximum, the leading edge has propagated into the stub, been reflected from the free end of the stub as a compression wave which enters the crystal and cancels out the trailing edge of the tension wave. The sum of the areas under these reflected waves is about 80% of the area of the first spike, indicating only 20% of the momentum has been spread out over the rest of the probe by the two free end reflections and three passages through the crystal and shield. This dissipation is small and indicates the rod is acting essentially as a simple homogeneous rod.

Unfortunately the probe was damaged about half way through the experimental measurements and the performance degraded. Figure 2-10 shows the results of an echo test made at the completion of the experiments. The increase in internal reflections is clearly evident from a comparison of Figs. 2-9 and 2-10. The time from 200 μsec to one msec is not as free from disturbances from the initial transient. A comparison of the initial and reflected momentum (areas under the curves) showed, however, that dissipation was not appreciably effected by the increased internal reflections, so the probe voltage was still an excellent measure of instantaneous stress. The principal damage was to the sensitivity to rapid changes in pressure.

Since the pendulum test could not identify the rise time of the probe, a free shock in air was used to measure this parameter. Figure 2-11 shows the output of the probe subjected to a fast (few μsec) rise in pressure which then decayed in about 100 μsec to zero. As shown in Figure 2-11, the time required for the stress indication to reach its final value is only about 7 μsec. Since this delay can be entirely ascribed to the electronics in the charge amplifier, the shock test shows that the response time of the probe is far better than the basic requirement of about 100 μsec. This means that changes in plasma pressure level at a rate of 10^5 Hz will be indicated with the same calibration constant as slower rates of pressure changes. Fig. 2-12 shows the decay in rise time caused by the probe damage.

2.3.2 Calibration Constant

Four independent methods were used to determine the voltage output for a given pressure. Two of these, one based on the published piezoelectric constant and the other on momentum transferred by collision with a pendulum were relatively inaccurate but served to insure that no gross systematic error occurred. A third method, using the calculated pressure rise in a shock tube was the least subject to systematic error, but also the least precise. The fourth method, using a yanked weight was the simplest and most precise and its accuracy, or freedom from systematic error, was confirmed by the other methods.

In the yanked weight method, the probe was loaded axially with a known weight, and the voltage output measured as the weight was rapidly removed. Figure 2-13 shows the voltage history obtained by balancing a 200 gm weight on the probe stub end with the other end resting on the floor. The scope preamplifier and charge amplifier were set on D.C. to record accurately the relatively slow changes in voltage. The repeatability (which limited the precision) of the measurement was good, as indicated in Fig. 2-13, but depended on holding the probe perfectly vertical and accurately centering the weight directly over the axis of the probe to insure all of the force acted to stress the piezoelectric crystal in compression and did not bend the rod. The accuracy of the cali-

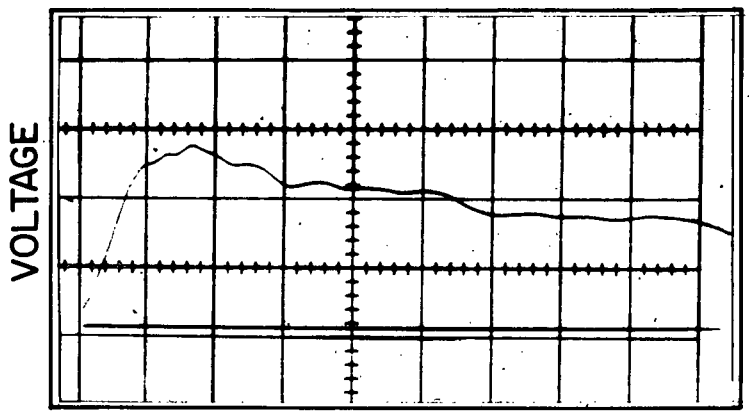

SHOCK WAVE RESPONSE OF THE PRESSURE PROBE

FIGURE 2-11

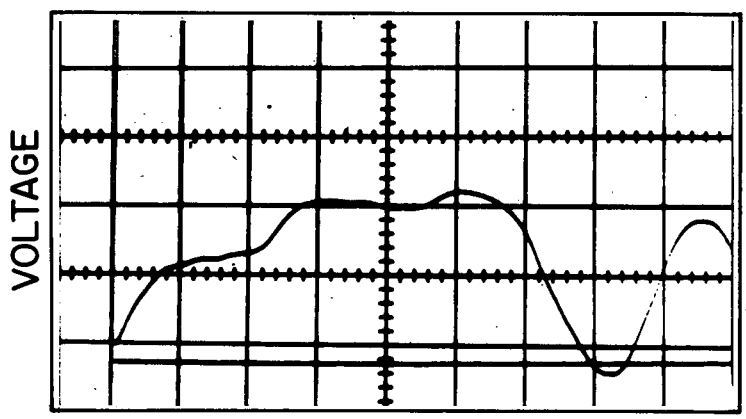

SHOCK WAVE TEST RESPONSE AT THE CONCLUSION OF THE EXPERIMENTS

FIGURE 2-12

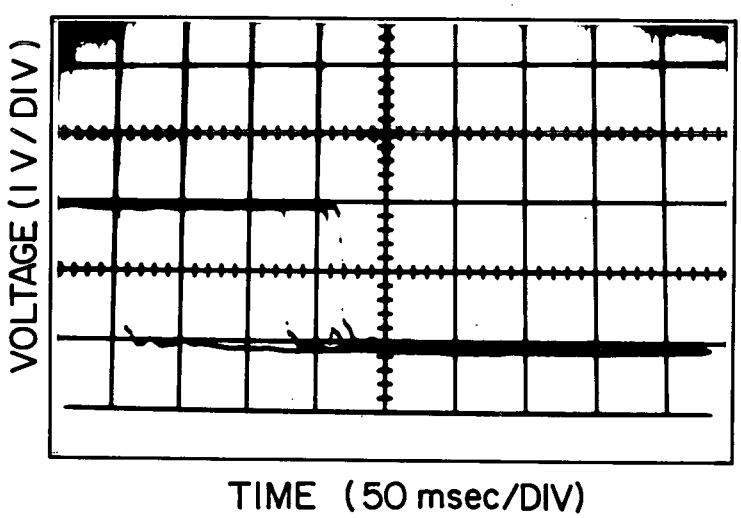

YANKED WEIGHT CALIBRATION RESPONSES

FIGURE 2-13

AP25 · P · 386

bration using this technique depends on the assumption that the response of the probe to the relatively slow (several msec) changes in stress caused by removing the weight, accurately reflects the response to the more rapid pressure changes to be measured in the plasma. This assumption was verified with the shock tube calibration.

The yanked weight method proved to be sufficiently simple so that it was used each time the probe was removed from the vacuum tank, to recheck the calibration constant. The only change discovered was after the accidental damage previously mentioned, when the calibration constant increased by 19% from 1.68 to 2.0 volts/200 g weight. This increase occurred because the broken potting epoxy (Item 12 in Fig. 2-8) would no longer support any stress.

Figure 2-14 summarizes the results for a series of tests (prior to taking the data) using 5,10,20,50,100 and 200 g weights. The bars indicate the range of voltage changes obtained with each weight and indicate the precision of the measurement. The deviations of the measurements from a straight line shown on Fig. 2-14 were ascribed to experimental error rather than to a non-linear probe response. Neglecting the widely scattered 5 g results, and applying the statistical test to a least squares fit of the data, the results summarized in Fig. 2-14 gave a 95% confidence that the probe response is within the range of 8.5 ± 0.2 millivolts per gram weight. Since the area of the probe is 0.726 cm^2, the calibration constant is

$$K = (8.5 \pm 0.2 \times 10^{-3})(0.726 \times 10^{-4}) / 9.8 \times 10^{-3}$$
$$= 6.30 \pm 0.15 \times 10^{-5} \text{ volts} / N/m^2$$
$$= 6.30 \pm 0.15 \text{ volts/ atm}$$

After the accidental probe damage, a similar series of calibrations gave $K = 7.50 \pm 0.20$ volts/ atm.

In the shock tube calibration method, three pressure probes were mounted in the driven section of a 1.2 inch shock tube (Ref. 2-8). One probe in the end wall and another 20 cm upstream were

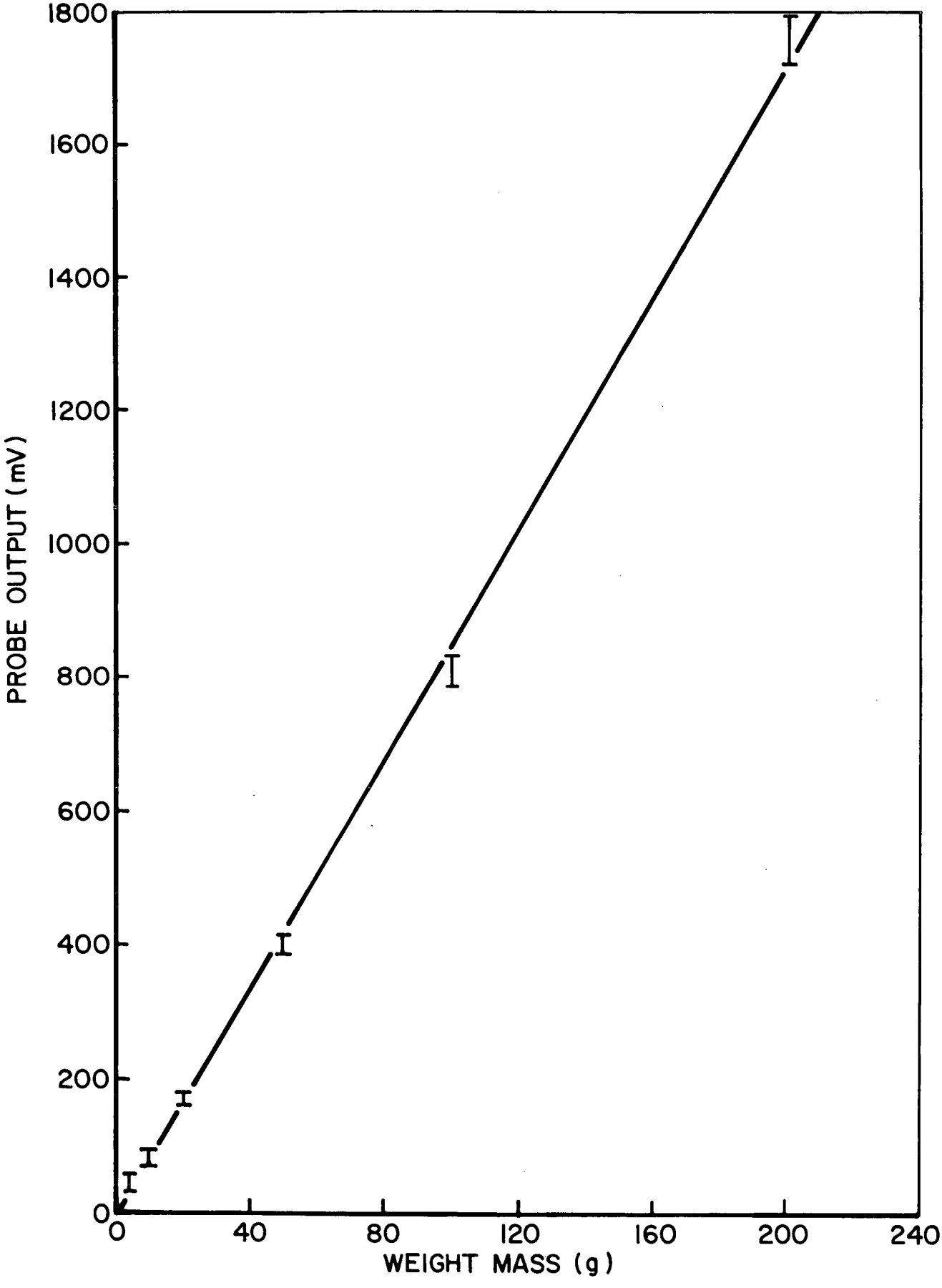

YANKED WEIGHT CALIBRATION
OF PRESSURE PROBE

FIGURE 2-14

AP25-4715

used to measure the shock wave velocity. The pressure probe to be calibrated was mounted flush with the tube wall, 10 cm from the endwall. The shock tube was operated with driven section pressures of 1, ½, ¼, 1/10, 1/20 and 1/100 atm of argon and the driver section at zero to 30 psig.

Figure 2-15 shows a typical data photograph. The bottom trace records the voltage output of the probe to be calibrated on a 100 μsec/div time scale, and the top trace records the voltage sum of the outputs of the timing probes on a 20 μsec/div time scale delayed exactly 200 μsec from excitation of the upstream probe. The apparent ending of the upper trace is caused by the shock arriving at the end wall and driving the summed voltage off scale. The upper base line contains 10 μsec per pulse timing markers to allow accurate shock time of flight determination.

Figure 2-16 summarizes the results of the shock tube calibration. The observed voltages from the data photograph are translated into pressure change using the yanked weight calibration of 6.3 v/atm and plotted against the Mach number squared of the shock calculated from the measured time for the shock to travel the known distance (20 cm), and using the room temperature (15°C) velocity of sound in argon. The bars represent the range of voltages observed on a single photograph (see Fig. 2-15) and the estimated possible error in reading the driven section pressure on a mercury manometer. Also plotted on Fig. 2-16 is the pressure ratio predicted by the perfect gas relationship

$$\frac{\Delta P}{P} = \frac{2\gamma}{\gamma + 1} (M^2 - 1) \qquad \text{(Ref. 2-9)}$$

The triple line indicates the uncertainty in the proper temperature (± 5°C), distance over which the time of flight is measured (± 2 mm) and the molecular weight of air (molecular weight uncertainty of .05) in the driven section.

The excellent agreement between the predictions and measurements of the pressure rise behind a shock based on the yanked weight calibration constant proves that the probe response to

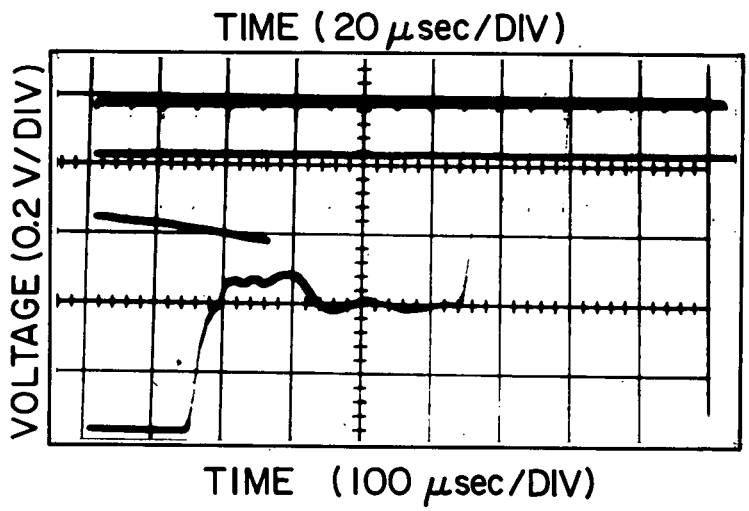

SHOCK TUBE - PROBE CALIBRATION RESPONSE

FIGURE 2-15
AP25 · P · 384

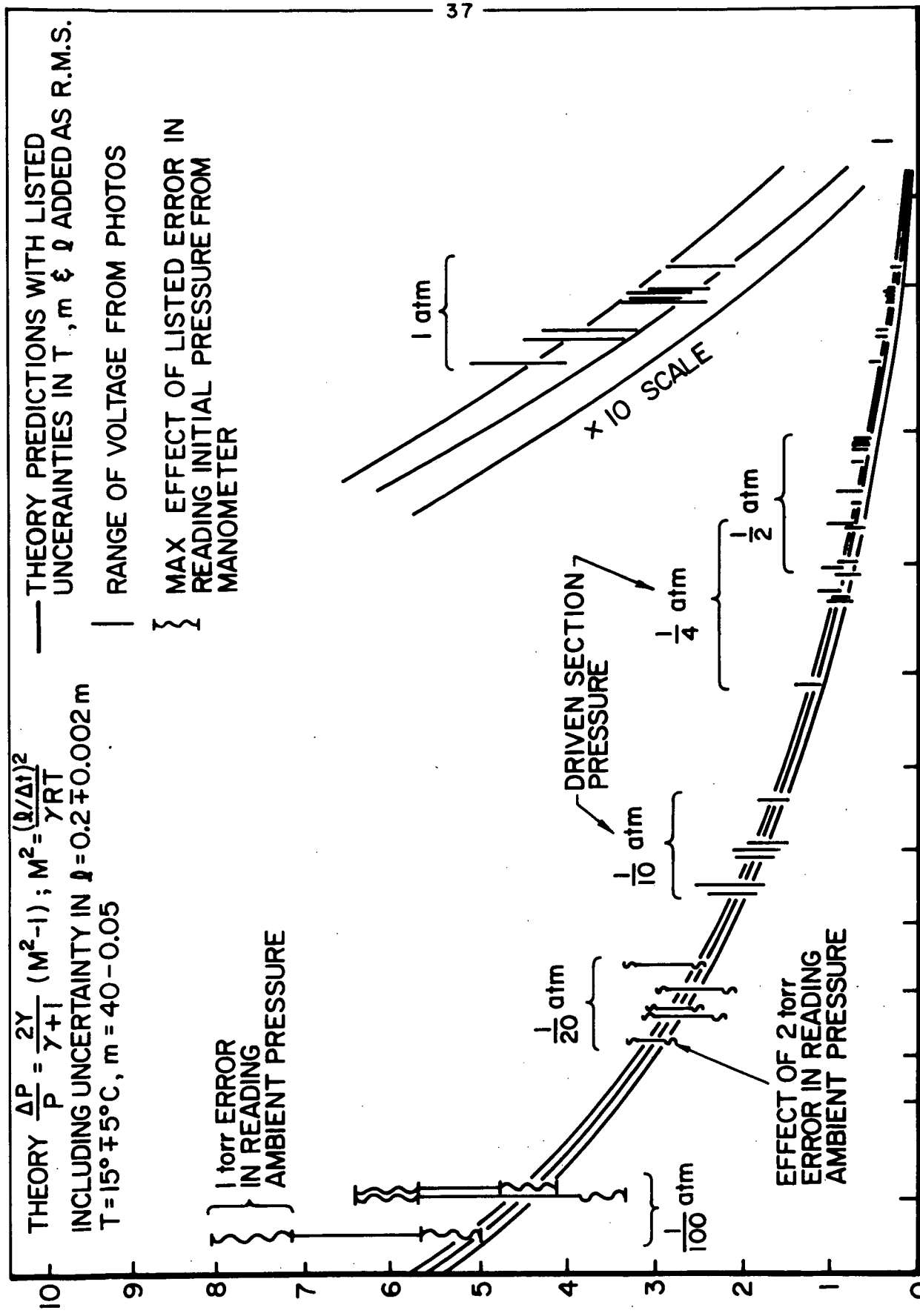

FIGURE 2-16

SHOCK TUBE CALIBRATION OF PRESSURE PROBE

AP 25 · 4714

slow (several msec) and fast (10 μsec) pressure changes are nearly identical. Figure 2-15 shows the easily obtained, high precision yanked weight calibration constant is also accurate at least within the precision of the shock tube measurements.

The final two calibration techniques were relatively subject to undetermined systematic error, but were useful to reduce the possibility of a major systematic error common to the yanked weight and shock tube calibrations. The first of these is based on the published average value of the piezoelectric constant of PZT-5 of 374 X 10^{-12} coulombs/newton (Ref. 2-6). The Kistler charge amplifier was found to produce 2 mV/pC, so the expected average calibration constant is about 5.4 V/atm compared with the 6.3 V/atm for this particular crystal. This (15%) is well within reported (Ref. 2-6) variations in this material.

Finally, both the probe and another Plexiglas rod with equal mass, m = 80 g, and the same acoustic lengths were coaxially suspended by 2.35 meter long strings (l) with their ends just touching. The rod was drawn back 5,10,15 and 20 mm (d) and released. Figure 2-17 shows the voltage output history from the probe. The shape of the rise and decay times indicate that the collision was not perfectly elastic and the rod was observed to rebound only about one-fifth of the initial separation distance (d). Using these data, the estimated momentum induced in the probe ($1.2 \times m1\sqrt{2g/d}$) was compared with the momentum in the probe calculated from the area under the voltage history curves. (This area in volt-seconds times the ratio of the crystal area, 0.726 X 10^{-4} m^2, to the yanked weight derived calibration constant, 6.3 X 10^{-4} $V/N/m^2$, gives the momentum of the probe.) The ratios of these two momenta were calculated for the 5,10,15 and 20 mm initial separations as, respectively, 1.02,0.97, 1.00, and 0.96 all of which are much closer to one than expected from the rough estimate of the rebound distance. This calibration also supports the contention that the yanked calibration constant is indeed a constant.

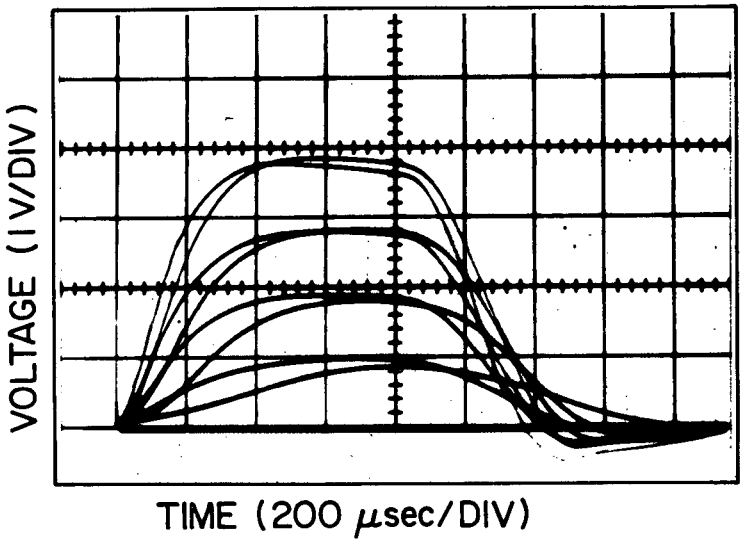

PENDULUM CALIBRATION RESPONSE OF PRESSURE PROBE

FIGURE 2-17
AP25·P·385

The conclusion is thus that the probe calibration is 6.3 V/atm, (7.50 after the accidental damage), independent of pressure amplitude or frequency over the range of interest, and these values were used with confidence to reduce the plasma pressure measurements.

CHAPTER 3
EXHAUST PLUME MOMENTUM FLUX

The momentum flux in the exhaust plume of the MPD accelerator was measured with an impact pressure probe. The interaction of this probe with the plasma was similar to a pitot tube, so the standard pitot corrections were applied to reduce the impact pressure data to axial momentum flux. Radial profiles of the jet were obtained for eight different combinations of mass flow rate and arc current. In addition, centerline momentum flux was measured at 1.9, 3.8, 5.9, 23, and 36 grams per second nominal mass flow rates for arc currents from 8 to 50 kiloamperes. At the "standard" ($\dot{m}$ = 5.9 g/sec, I = 15.6 kA) condition, radial profiles were obtained at 11, 5, and 1 inch from the anode face. All profiles were integrated assuming axial symmetry to obtain the total momentum content of the exhaust jet. These measurements were used to determine the effect of mass flow rate and arc current on the shape and time evolution of the jet and on the thrust of the MPD accelerator.

3.1 Apparatus

Figure 3-1 shows the apparatus used to measure momentum flux. The impact pressure probe behaves essentially as a one inch diameter, shrouded pitot tube using the pressure probe described in the previous chapter to sense the impact pressure. Unusually fast response times were achieved by mounting the pressure probe sensing surface 1/8 inch behind the probe orifice.

The 2-3/4 inch Plexiglas tube shown in Fig. 3-1 is used to protect and support the pressure sensor and pressure shield. The tube prevents buffeting of the sensor by the turbulent jet and delays any other spurious pressure signals, for example, the rise in static pressure on the end of the acoustic delay rod. Consequently together with the rubber band pendulum support, the tube acoustically isolated the pressure sensor from all acoustic excitation except the desired signal for the one msec test. In addition, aluminum foil and silver paint on the surface of the tube help shield the

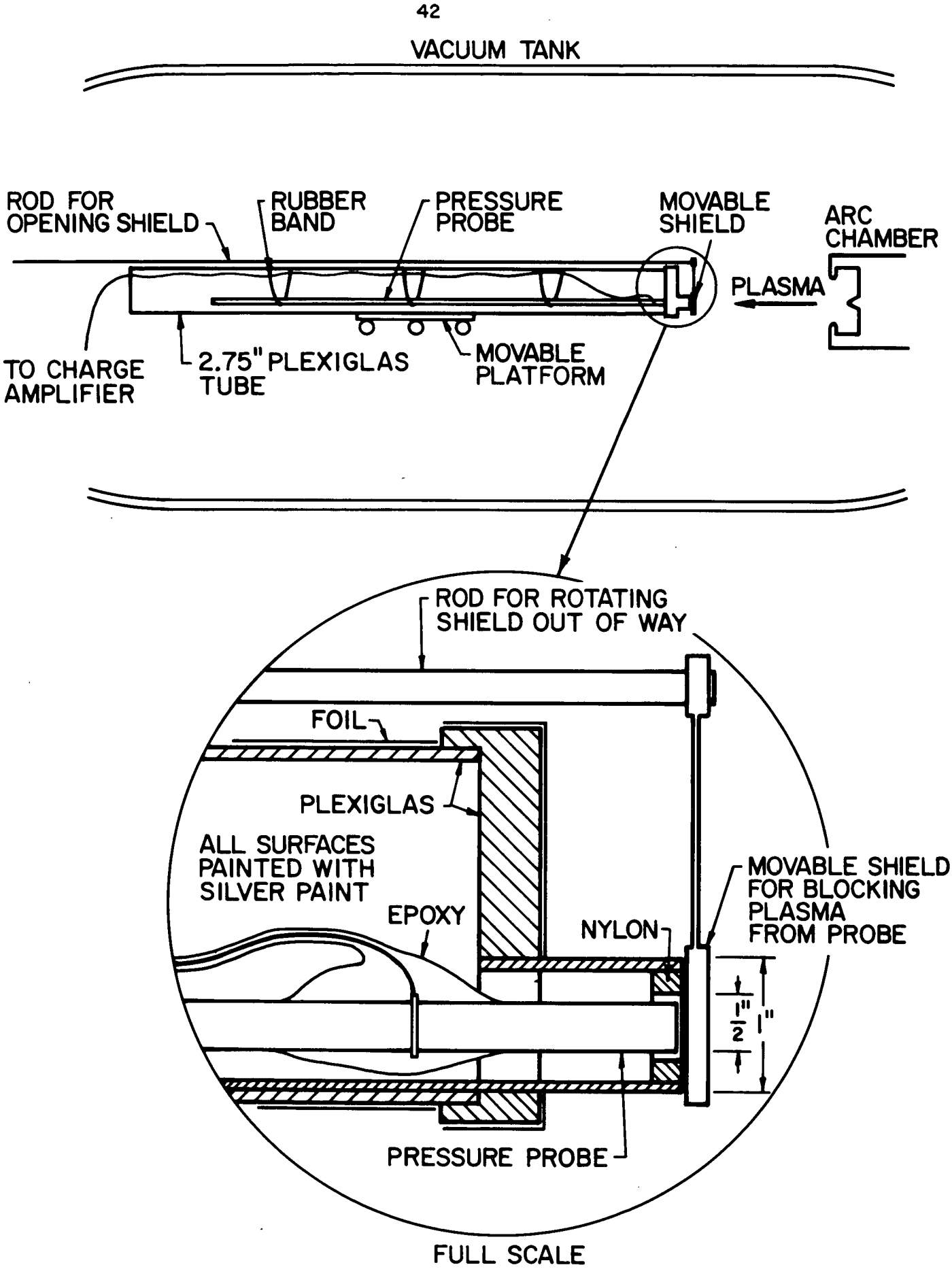

IMPACT PRESSURE PROBE

FIGURE 3-1
AP25·4712

piezoelectric crystal from radiant heating by the arc. The tube also supports the pressure shield and the rod for rotating this shield in or out of position from outside the sealed vacuum tank. This shield, (see Fig. 3-1) consists of a flat, one inch square plate. The place can be positioned well away from the pitot tube where it will not interfere with the plasma in front of the probe orifice, or alternatively, it can be rotated to tightly seal the probe orifice. In the latter position, by preventing the plasma from reaching the pressure sensor, it allows the noise amplitude at a given position to be determined immediately after a data shot by rotating the shield into position, and then taking a duplicate shot.

The 2-3/4 tube is mounted on a movable platform which is suspended from the tank walls. With the tank evacuated, the platform axial and radial position may be controlled from outside the tank. Since the tube is nearly as large as the tank, the achievable positions of the pitot orifice are limited to 20 inches from the anode and 10 inches from the centerline. Also an obstruction on the platform prevents probing to the right of the centerline.

The pitot pressure history is recorded by a Tektronix 555 oscilloscope fitted with a Hewlett Packard Model 196A camera using Type 47 Polaroid film. The 1A7A pre-amplifier in the scope is fed by a Kistler Model 365 charge amplifier with a 500 pF feedback capacitor. The charge amplifier received the pressure signal through an 8 foot length of RG 58/U coaxial cable which passes through a vacuum fitting on the tank, through Tygon tubing, to connect to a vacuum seal on the pressure probe coaxial lead. Arc current is detected with the Rogowski coil described in Chapter 2 and recorded (on the same photograph as the impact pressure history) by the upper beam of the 555 oscilloscope.

3.2 Data Analysis

The raw data were obtained in the form illustrated in Fig. 3-2 which shows the arc current, impact pressure and noise histories. Each oscilloscope photograph is a record of several

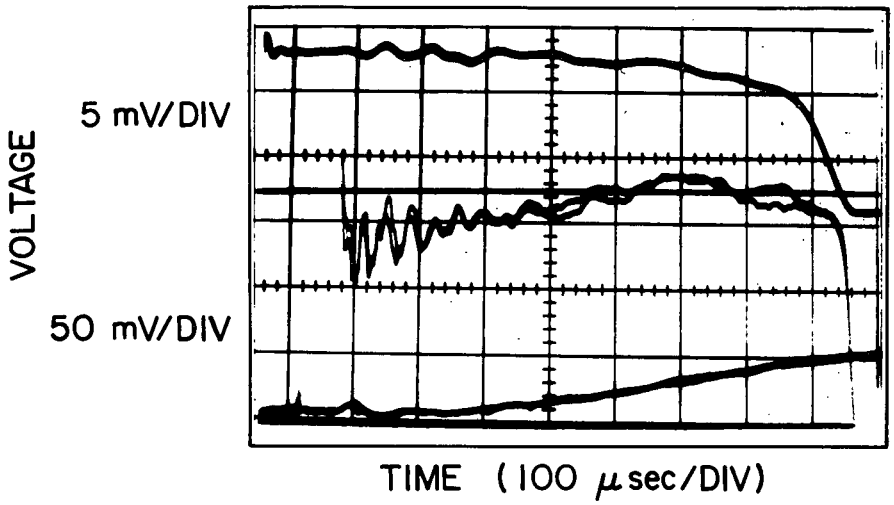

a) CENTERLINE POSITION

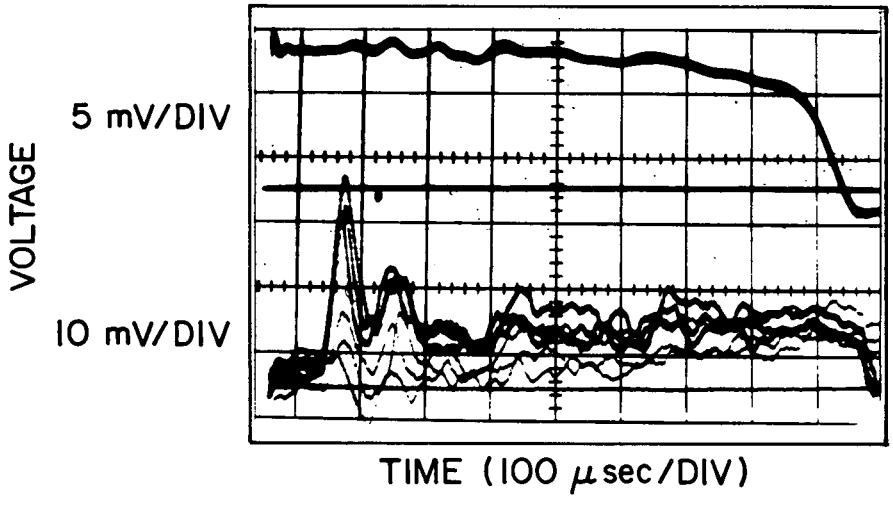

b) 8 INCHES FROM CENTERLINE

TYPICAL CURRENT , PITOT PRESSURE AND NOISE HISTORIES

FIGURE 3-2
AP25 · P· 390

shots taken at the same radial and axial position and with the same operating conditions of arc current and mass flow rate. From this data the axial component of the momentum flux during the quasi-steady phase was calculated and the accuracy and precision estimated from the multiple shot records for each of the positions and set of operating conditions investigated. Then, for each axial position, the total momentum flow (thrust) was computed by integrating over the jet area, assuming axial symmetry.

The calculation of the momentum flux from the raw data involved consideration of the calibration factors, noise subtraction, time selection, conversion of the measured stagnation pressures to momentum flux by a pitot tube model, and statistical analysis of the data scatter. Similarly, the total thrust integration involved corrections from the apparent probe position to the actual position of the measured impact pressure. The details and reasoning for the data reduction procedures are given in Appendix 3A. Table II illustrates these procedures by reducing the raw data of Fig. 3-2 ($\dot{m}$ = 5.9 g/sec, Z = 11 inches and R = 0 and 8 inches) to momentum flux at the corrected positions and form required for total thrust integration.

3.3 Results

The impact pressure histories obtained as a function of position over a range of currents and mass flow rates, add appreciably to the information available concerning the time evolution of the axisymmetric flow of accelerated plasma. In addition, the magnitudes during the quasi-steady phase show the dependence of total thrust on current and mass flow rate. This, in turn, throws some light on which of the many theories best describe the behavior of an MPD accelerator of this geometry and mode of operation.

3.3.1 Operating Conditions

The matrix of Table III shows the mass flow rates ($\dot{m}$) and arc currents (I) for which full momentum flux profiles were obtained.

TABLE II

Data Reduction Example

	Correction	Example*
1.	Time selected:	t = 100 μsec for I, 500 μsec for P
2.	Noise: $P_o(0)$ =	165 mV - 20 mV = 145 mV
	$P_o(8)$ =	10 mV - 6 mV = 4 mV
3.	Scaling: I =	(1.53 kA/mV) (10.5 mV) = 16 kA
	$P_o(0)$ =	(0.159 atm/V) (0.145V) = 0.023 atm
	$P_o(8)$ =	(0.159 atm/V) (0.004V) = 0.00064 atm
4.	Pitot Shock Wave:	P(0) = 0.023/0.9 = 0.026 atm
		P(8) = 0.00064/0.9 = 0.0007 atm
5.	Pitot Yaw:	P(8) = (0.0007) (0.98) = 0.0007 atm
6.	Pitot Re:	P(8) = 0.0006 $\pm$ 0.0001 atm
7.	Axial Component:	$P_z(8) = (0.000\bar{6})\ (\cos\theta) = 0.000\bar{4}8$ atm
8.	Axial Flow:	$P_{zz}(8) = (0.000\bar{4}8)\ (\cos\theta) = 0.000\bar{3}9$ atm
9.	Radial Position:	P(0) ⟶ P(0.5")
		P(8) ⟶ P(8.5")
10.	Grad P:	P(0.5) ⟶ P(0.5)
		P(8.5) ⟶ P(8.36)
11.	Symmetry Integral:	$2\pi RP_{zz}$ (0.5) = 5 N/inch
		$2\pi RP_{zz}$ (8.36) = $1.\bar{5}$ N/inch
12.	Precision:	$2\pi RP_{zz}$ (0.5) = 5 $\pm$ 9%
		$2\pi RP_{zz}$ (8.36) = 1.5 $\pm$ 115%
13.	Thrust:	$\int_0^\infty 2\pi RP_{zz}dR$ = 77 N $\pm$ 20%

* Raw data from Figure 3-2, $\dot{m}$ = 5.9 g/sec, Z = 11 inches

TABLE III

Operating Conditions

Profiles at Z = 11 inches

$\dot{m}$ (g/sec) \ I (kA)	8	12.3	15.6	27	36
1.9	X			X	
3.8		X			
5.9	X		X	X	
23				X	
36					X

Profiles at $\dot{m}$ = 5.9 g/sec, I = 15.6 kA

1. Z = 1"
2. Z = 5"

Centerline Momentum Flux at Z = 11 inches

1. For $\dot{m}$ = 1.9 g/sec, I = 24.7 to 9.4 kA
2. For $\dot{m}$ = 3.8 g/sec, I = 30.2 to 7 kA
3. For $\dot{m}$ = 5.9 g/sec, I = 30.2 to 11.3 kA
4. For $\dot{m}$ = 23 g/sec, I = 41 to 7.1 kA
5. For $\dot{m}$ = 36 g/sec, I = 50.5 to 16.5 kA

The values of the parameters which appear on the diagonal of Table III were selected to satisfy the "matched" flow conditions ($I^2/\dot{m} \approx 40$ $kA^2 \cdot sec/g$, see Ref. 3-7). Reference profiles were repeatedly obtained throughout the experimental period for the "standard" conditions, I = 15.6 kA, $\dot{m}$ = 5.9 g/sec.

In addition to the parameter ranges shown in the matrix, profiles were measured for $\dot{m}$ = 5.9 g/sec, I = 15.6 kA at 1 and 5 inches from the anode face to ascertain the jet shape. Finally the centerline momentum flux was determined over the operating range of arc currents for each of the five available mass flow rates. The operating range limits on the arc current were set by the limitations of the capacitor power supply system.

3.3.2 Jet Description

Time History A planned delay between the initiation of mass and current flows causes the chamber to be filled with an expanding cloud of neutral gas when the arc is ignited. This cloud of gas is ionized and accelerated into the vacuum chamber (Ref. 3-7) with a relatively slow velocity of less than 10^4 m/sec (Ref. 3-1). The leading edge of the accelerated gas, therefore, consists of a high density, low velocity region which should appear to the impact pressure probe as an initial transient.

Figures 3-2 and 3-3 show the momentum content and radial distribution of this initial transient at a distance of 11 inches from the anode face. In Fig. 3-2a, the initial transient is large, indicating most of the swept gas (momentum) is accelerated along the axis, but the small initial transient in Fig. 3-2b shows some reaches this radius. Since this plasma is slower (Ref. 3-8), but more massive (Ref. 3-7) than the quasi-steady jet, it provides an ambient background source from which mass may be ingested into the quasi-steady jet. In this way, the initial transient provides evidence of a condition which might cause the large (100% or more) shot-to-shot variations in the momentum flux measured at the edges of the quasi-steady jet discussed below.

After the initial transient, the voltage, current and jet velocity (Ref. 3-8) quickly settle to steady values that remain constant for at least 0.6 msec. This is the quasi-steady mode of operation. Figure 3-2a shows that the momentum flux on the centerline is also quasi-steady during this period. (The early fluctuations observed in Fig. 3-2a are acoustic oscillations in the probe as are the longer lived oscillations in the damaged probe as shown in Fig. 3-4 (see Chapter 2)). At the edge of the jet, however, the fluctuations are up to 100% of the observed pressure. Since the jet Reynolds number as it leaves the anode orifice (Sec. 5-4) is about 1.5×10^4, these edge fluctuations may represent the onset of turbulent interaction of the fast jet with the slow ambient plasma.

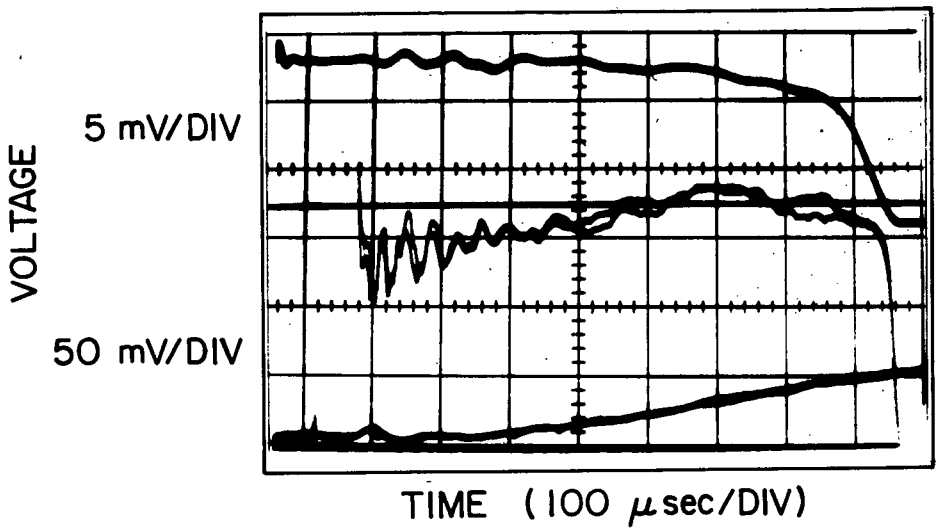

a) CENTERLINE POSITION

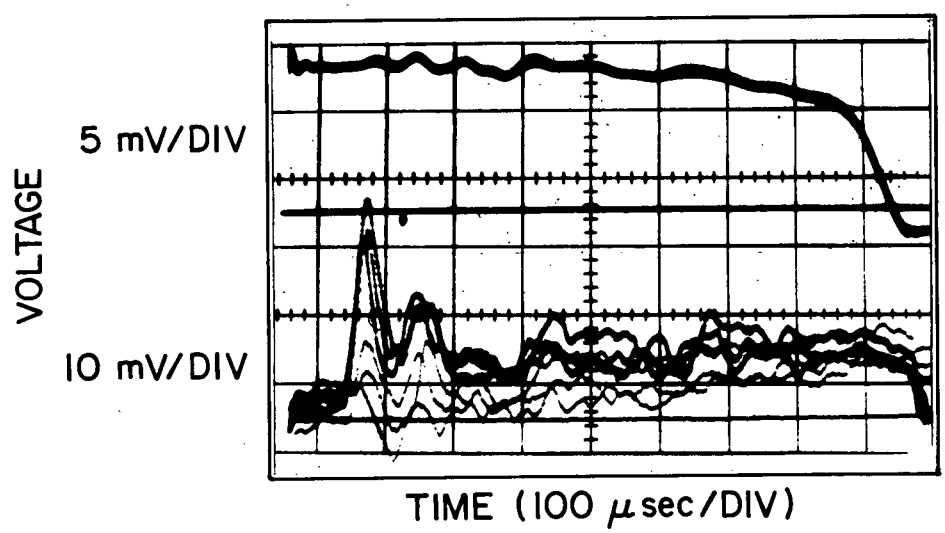

b) 8 INCHES FROM CENTERLINE

TYPICAL CURRENT , PITOT PRESSURE AND NOISE HISTORIES

FIGURE 3-2

AP25 · P· 390

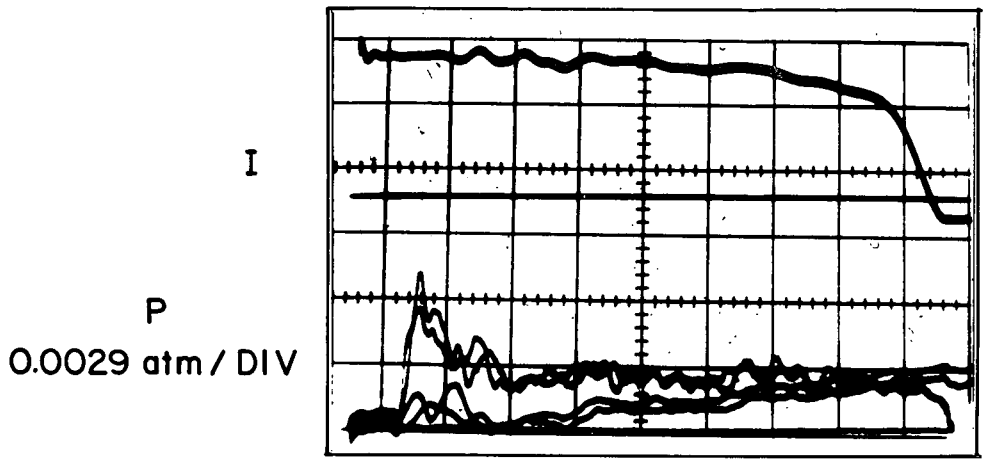

CURRENT, PITOT AND NOISE HISTORIES
AT R=6 AND Z=11 in

FIGURE 3-3

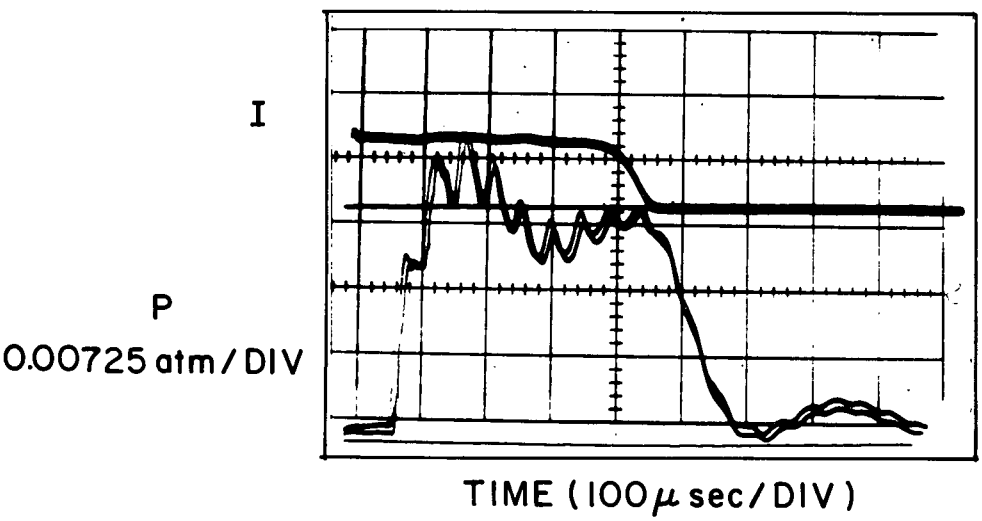

SHORT CURRENT PULSE HISTORIES

FIGURE 3-4

The trailing edge of the quasi-steady flow is defined by termination of the arc current. Figure 3-4, taken with a 1/2 msec current pulse, shows that the momentum flux drops to zero after the arc is extinguished. The lower velocity associated (Ref. 3-8) with the reduced current level over the last 50 μsec causes this trailing edge to be spread out over 100 μsec by the time it has traveled the 11 inches to the impact pressure probe.

Jet Profile The shape of the quasi-steady jet at 11, 5 and 1 inches from the chamber is sketched in Fig. 3-5. The main feature of interest in this presentation is that the jet leaves the chamber as a narrow beam about 2 inches in diameter (from a 4 inch diameter orifice!) and expands radially into a nearly gaussian profile with a half width of nearly six inches at a position 11 inches from the chamber. Probe interpretation is difficult in the very large pressure gradients at Z=5 and Z=1 inches (Section 3.A.4), but the best interpretations indicated that the jet edges were initially very sharp. When these three profiles were replotted for the purpose of integrating the thrust, it was found that the function $2\pi RP_{zz}(R)/ZR$ (approximately the derivative of the profile) scaled nearly linearly with the Z position.

The integrated total thrust at all three positions agreed within 2%.

The most rewarding technique for investigating the profile shape at Z = 11 inches is shown in Fig. 3-6. To obtain this plot, the axial momentum flux measurements were treated as the ordinate of a histogram vs. radial position. The fraction of the area of the histogram outside a given R was then plotted against R on normal probability paper. As is evident from Fig. 3-6, the data points fall nearly on a straight line, indicating the distribution is nearly Gaussian. The deviations from Gaussian are principally at large radii, where the turbulent boundary causes the maximum uncertainty in the data. By similarly plotting the profile data for all the other mass flow rates and currents, it was found, within the precision of the profile measurements, the shape of the jet was independent of $\dot{m}$ and I. The apparent width (standard

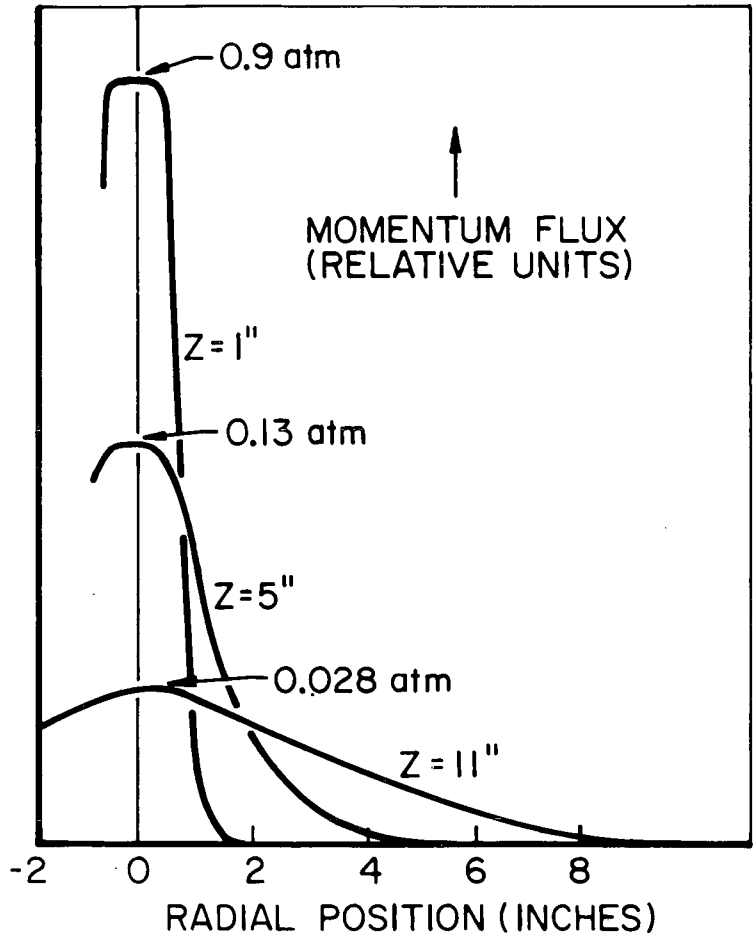

JET PROFILES AT 11, 5 & 1 INCHES
FROM THE ANODE FACE

FIGURE 3-5

AP25 · 4720

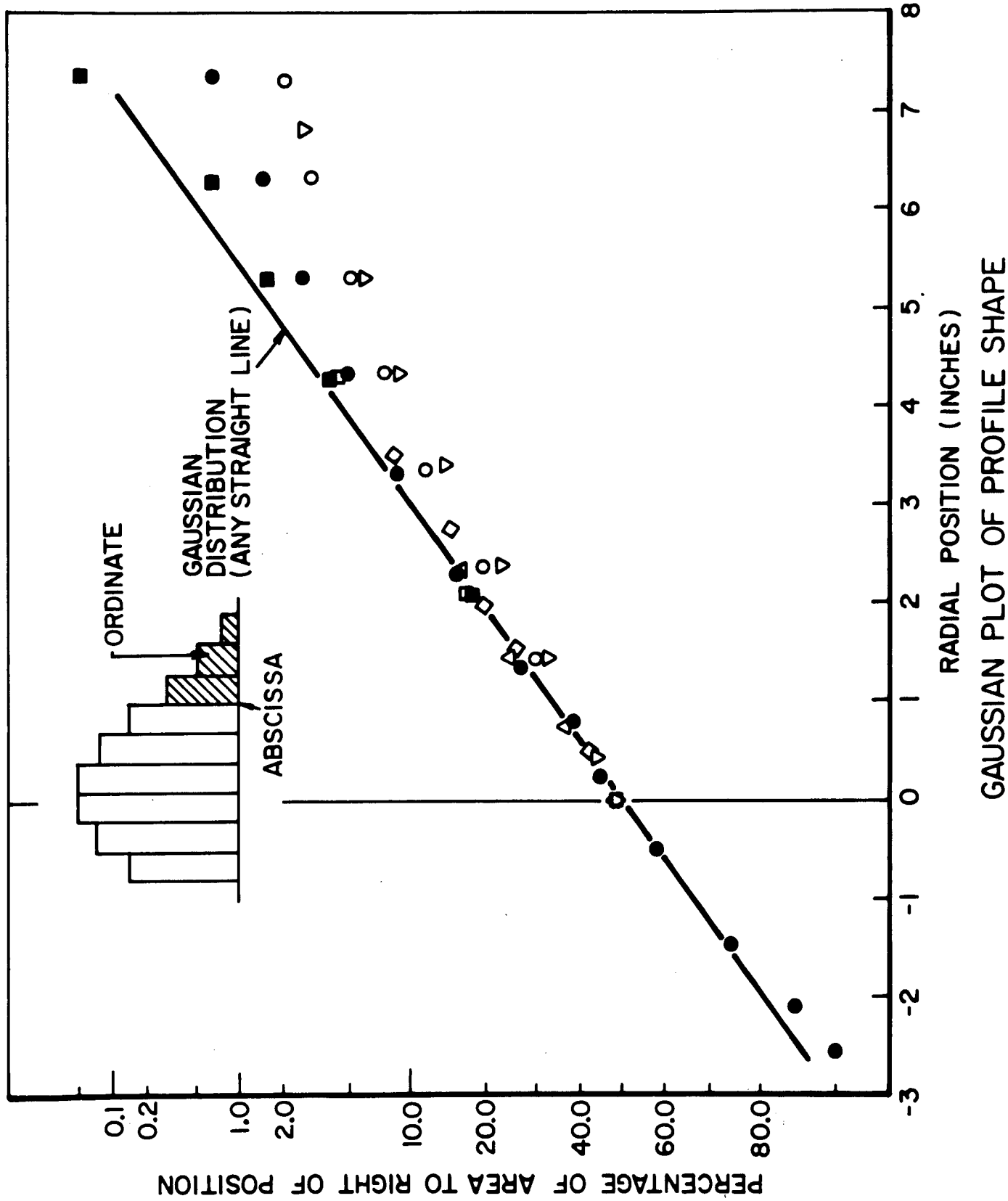

FIGURE 3-6
AP25 · 4719

deviation σ = 2.3 inches) also remained constant. This provides a first order description of the invariant shape of the jet which is especially useful in estimating the total thrust of the jet from a single impact pressure measurement (P_{zz}) on the centerline using the relation:

$$\text{Thrust} = 2\pi\sigma^2 P_{zz}(R=0)$$

3.3.3 Total Thrust

Figure 3-7 summarizes the total thrust information obtained by integrating the momentum flux profiles. Also shown are the nominal mass flow rates for each profile and the total electromagnetic (EM) thrust predicted assuming an axially symmetric current density distribution (Ref. 3-9). The error bars represent the best estimate of the range within which the thrust can be located with 95% confidence. These limits are a best estimate rather than a precise statistical statement, principally because it was necessary to estimate the momentum injected at the edges of the quasi-steady jet from the snowplow initial transient. Despite these limits on the precision, three significant conclusions can be drawn from the summary in Fig. 3-7.

First and most important, the data show that the total thrust scales as the square of the current over the range of parameters investigated. This relation has been previously confirmed by thrust stand measurements at lower currents and for different geometries (Ref. 3-10 and 3-11). The data reported in Fig. 3-7 confirms that $T \propto I^2$ continues to hold up to at least 36 kA for a pulsed MPD accelerator with a very large anode orifice (4 inches). Since the theoretical justification of the I^2 relation is based on the assumption of axial symmetry, the data also indicate this symmetry is maintained ("spokes" are not important).

Second, the measured total thrust significantly exceeds the predicted electromagnetic thrust for all except two of the conditions. This result is particularly interesting since the electromagnetic thrust component in a real device would be expected to approach the theoretical prediction as an upper limit, not exceed the prediction.

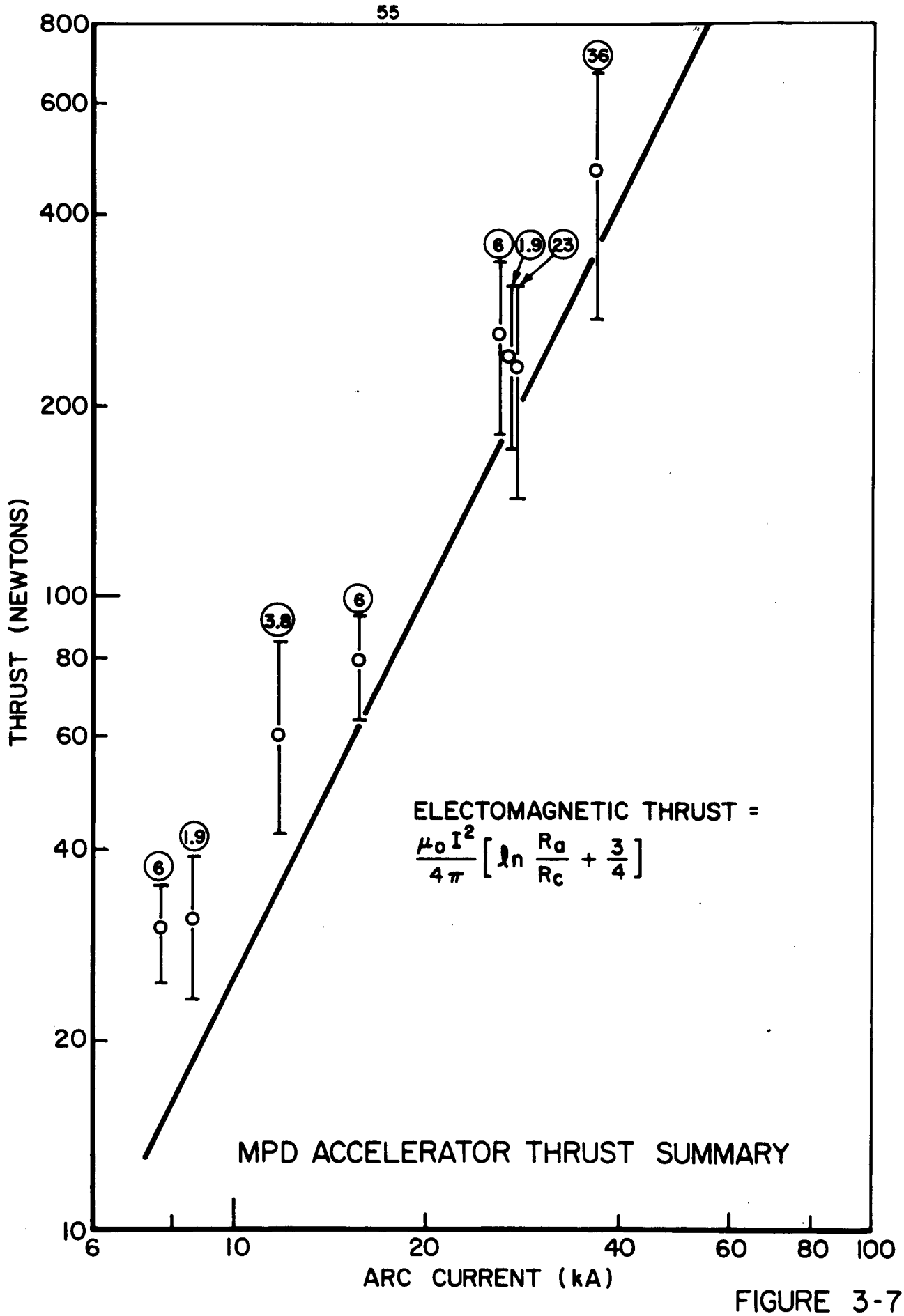

FIGURE 3-7
AP25-4716

For example, even a small (few percent) deviation from exact axial symmetry would reduce the EM thrust component significantly. Of the possible real device effects, only a drastic reduction in the cathode attachment radius could increase the EM thrust and the experimental evidence (see Ref. 3-2) indicates this does not happen in the present accelerator. This leads to the conclusion that in this geometry, significant thrust is provided by electrothermal acceleration over the entire range of parameters. It was expected that at very low currents the MPD accelerator would act as an electrothermal arc jet, deriving most of its thrust from the expansion of the heated plasma, but the indication in Fig. 3-7 that even at the highest currents, from 10% to 55% of the total thrust is electrothermal is surprising. Since this device does not have a material nozzle, this, in turn, indicates the $\vec{j}\times\vec{B}$ body forces act (favorably for a change) to simulate an effective converging - diverging nozzle.

3.3.4 Centerline Momentum Flux

The momentum flux on the centerline is of particular interest for two reasons. First it can be measured with much greater accuracy (10%) and resolution (5%) than the total thrust, and second, it is much easier to determine, requiring only one measurement at each condition. The first of these reasons is important in that it allows more subtle relationships to be detected. The second is important because of the apparently invariant shape of the jet (Section 3.3.2). A useful estimate of the total thrust can be simply calculated from the single measurement of the centerline momentum flux.

Figure 3-8 shows a typical data record for a survey of momentum flux on the centerline as a function of arc current, for $\dot{m}$ = 1.9 g/sec and Z = 11 inches from the anode. The first half of the traces should be ignored as probe-caused oscillations. The latter half of the figure clearly shows the monotonic change in momentum flux with arc current (upper set of traces).

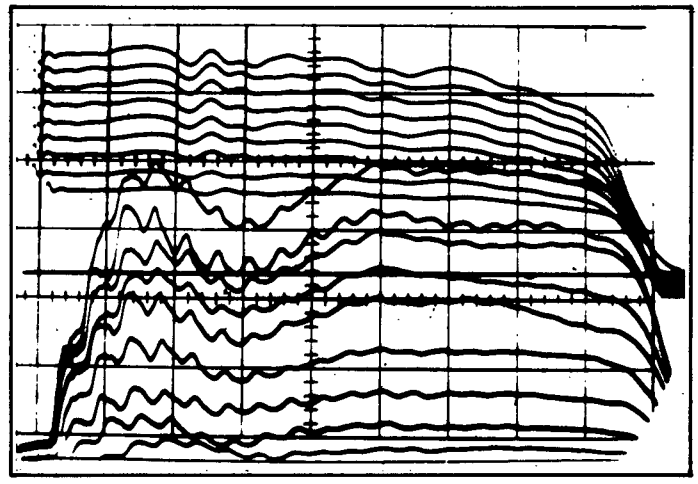

CENTERLINE MOMENTUM FLUX DATA FOR $\dot{m}$ = 1.9 g/sec

FIGURE 3-8

AP25 · P · 392

Figure 3-9 summarizes the measurements of the centerline momentum flux. In this plot, although the general trend is identical for all mass flow rates, there is some evidence that lower mass flows produce lower centerline momentum flux. The effect, if real, is barely within the precision of the present measurements.

Figure 3-9 also shows the centerline momentum to increase as the 2.35 power of the arc current rather than the 2.0 power. This probably indicates a narrowing of the jet shape at higher currents, an effect beyond the precision of the jet shape analysis in Section 3.3.2.

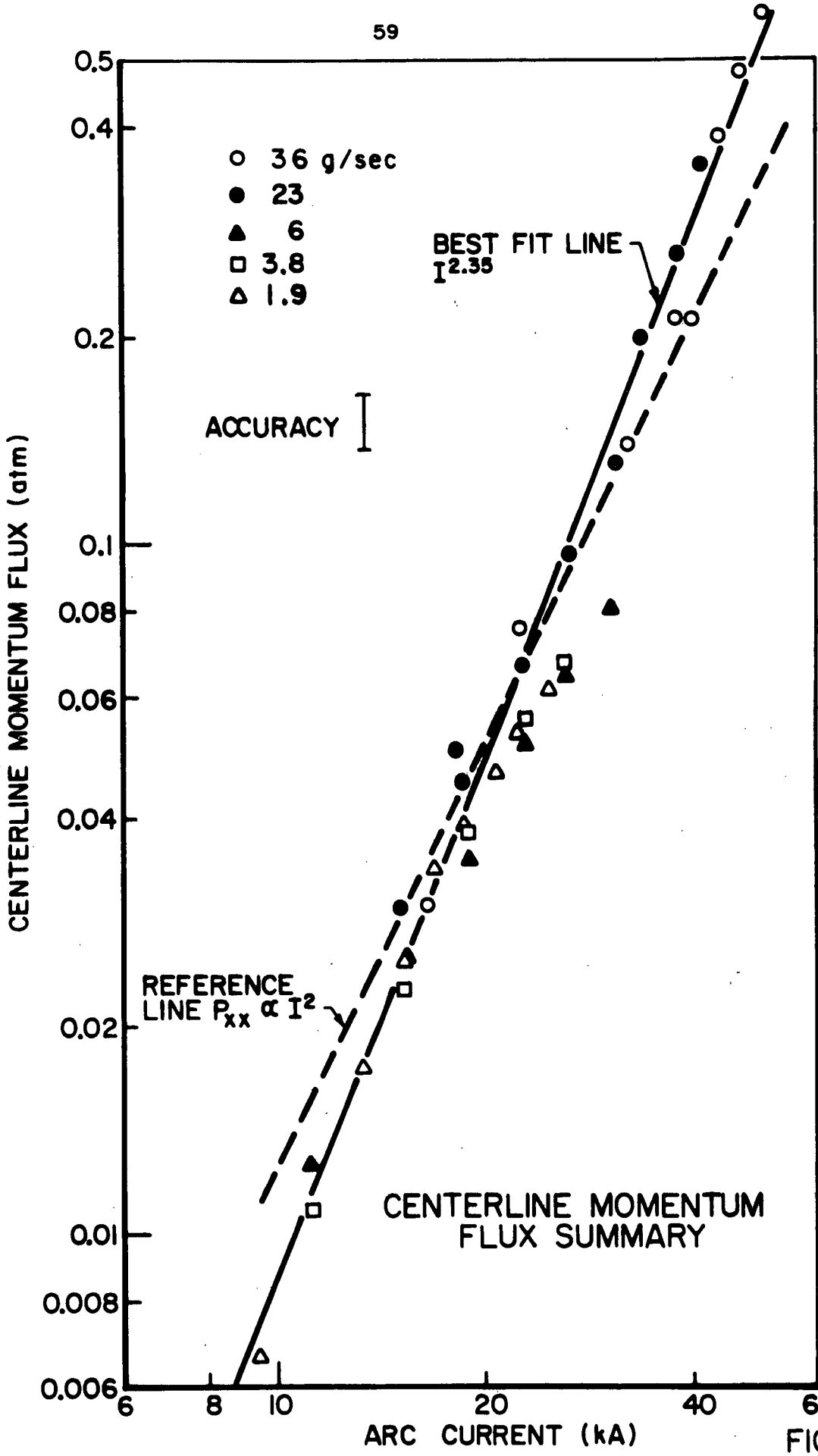

FIGURE 3-9
AP25-4718

Appendix 3.A Data Reduction Procedures

The task of analyzing the data is to convert the oscilloscope photographic records to momentum data as a function of position in the jet, mass flow rate and arc current. This task divides into four parts. First, the recorded voltage amplitudes of the traces are scaled to arc current and impact pressure histories using the calibration factors reported in Chapter 2. Second, the noise is subtracted and a current and pressure selected which are representative of the quasi-steady portion of the histories, and the precision of the measurements evaluated from multiple shot records. Third, the impact pressures are reduced to axial momentum flux values using a standard model of supersonic pitot tube behavior. Finally, for a given axial position, arc current and mass flow rate, the momentum flux as a function of radial position is integrated to obtain the total axial momentum in the jet. To illustrate these steps, the data recorded in Fig. 3-2 are analyzed below.

3.A.1 Scaling

The starting point for data reduction is exemplified in Figure 3-2 which shows two typical measurements of the arc current, impact pressure and noise histories. These data were obtained with a nominal mass flow rate of 5.9 g/sec at a distance of 11 inches from the anode surface. Figure 3-2a is a record of four successive shots with the probe orifice on the nominal centerline (R=0) and Figure 3-2b is a record of six successive shots at 8 inches from that centerline (R=8).

The top trace in each photograph is the multiple record of the arc current measured relative to the straight baseline (second trace from the top). The current calibration factor is 7.65 kA/div so the currents are about 16 kA. The next trace down is a multiple (X 2 in 3-2a, X3 in 3-2b) shot record of the impact pressure with calibration factors of, respectively, 0.00795 atm/div and 0.00159 atm/div. The bottom (light) traces in each figure are the noise

obtained by blocking the probe orifice. The baseline shifts especially noticeable in Figure 3-2b, are caused by 20 Hz vacuum pump acoustic noise.

3.A.2 Time, Noise and Precision

Time For both Fig. 3-2a and 3-2b the time near the center of the photograph (500 μsec after the start of the current pulse) was chosen as representative of the quasi-steady impact pressure. For earlier times, the initial transient caused by the snowplow gas (Ref. 3-1) caused acoustical oscillations in the pressure sensor (noticable especially in Fig. 3-2a after t=150 μsec) superimposed on the EM induced oscillations (noticable especially in Fig. 3-2b). For times later than t=800 μsec the returning acoustic echo attenuates the strain in the crystal (Chapter 2). The arc current amplitude was read at t=100 μsec, after the initial transient but before the RC decay of the passive integrator had a chance to appreciably reduce the integrated Rogowsky coil signal.

Noise To obtain the true impact pressures from the photographs, it is necessary to subtract off the noise. For example, in Figs. 3-2 the average noise on both figures was subtracted from the average signal at t=500 μsec to obtain average impact pressures during the quasi-steady phase of 0.023 and 0.00064 atm respectively. The short (60 μsec) initial time with no signal was used to establish the baseline level for both noise and signal amplitudes. The noise at t=500 μsec is principally from radiant heating of the piezoelectric crystal as can be recognized from the steady increase with time until the arc is extinguished.

Precision A statistical analysis of the shot-to-shot variation was carried out for one profile to establish the precision of the measurements. As may be inferred from Figs. 3-2, this precision was nearly independent of the radial position. The sample standard deviations for 9 signal minus 9 noise shots at R = 0, 1½, 3, 4, 5, 6, 7, 8 and 9 inches were, respectively 2.02, 3.15, 2.25, 1.13, 1.86, 0.19, 0.52, 1.05 and 1.05 X 10^{-3} atm. Applying the statistical t test, the 95% confidence limits for the true mean have a range about

the sample mean of, respectively, 1.5, 2.4, 1.7, 0.85, 1.4, 0.14, 0.4, 0.8 and 0.8 X 10^{-3} atm. Since the impact pressures for this profile varied from 23 X 10^{-3} on the center 0.6 X 10^{-3} atm at R=8, the precision varies from 5.8% to 114%. Because of this large imprecision at the edge of the jet, the total momentum flux in the jet can be determined only within about 30% at the 95% confidence level. This is a significant limitation on the results that can be expected from the present technique.

3.A.3 Pitot Corrections

Conversion of the impact pressures to momentum flux was based on the standard supersonic pitot model (Ref. 3-2). This model assumes a curved shock forms in front of the pitot orifice. The shock location and its effect on stagnation pressure is determined by the probe diameter, free stream Mach number, transverse velocity gradient, probe Reynolds number and yaw angle. The model assumes the plasma on the stagnation streamline passes through the shock with a normal incidence and is brought to rest isentropically in the subsonic region aft of the shock.

Supersonic Using this model, the pitot or isentropic stagnation pressure aft of the shock, P_o, is related to the static (thermodynamic) free stream pressure, p_s, and the free stream Mach number, M by the Rayleigh supersonic pitot tube formula, (Ref. 3-2),

$$\frac{P_o}{p_s} = M^2 \left(\frac{\gamma+1}{2}\right)^{\frac{\gamma}{\gamma-1}} \Bigg/ \left(\frac{2\gamma}{\gamma+1} - \frac{\gamma-1}{\gamma+1}\,\frac{1}{M^2}\right)^{\frac{1}{\gamma-1}}$$

Since the total momentum flux in the free stream, P, is related to the thermodynamic pressure p_s by $P = p_s + \rho U^2 = p_s(1 + \gamma M^2)$, the pitot pressure and momentum flux are related by

$$\frac{P_o}{P} = \left(\frac{\gamma+1}{2}\right)^{\frac{\gamma}{\gamma-1}} \Bigg/ \left(\frac{2\gamma}{\gamma+1} - \frac{\gamma-1}{\gamma+1}\,\frac{1}{M^2}\right)^{\frac{1}{\gamma-1}} \left(\gamma + \frac{1}{M^2}\right)$$

Fortunately, this expression is very insensitive to the exact value of both γ and M, since neither quantity is known in the plasma jet with great accuracy. For Mach numbers from 2 to ∞, and with

γ near 5/3 in and after the shock and slightly lower in the free stream, the above relation reduces to

$$P = P_o/0.9$$

with an estimated uncertainty of 5%.

Reynolds Number Based on the extensive empirical experience with pitot tubes, three additional corrections to the impact pressure were considered. These were viscous losses, yaw and resolution of the pitot pressure into axial and radial components. The effect of viscosity on pitot pressures has been extensively investigated as a function of Reynolds number. The results, summarized in Refs. 3-3 and 3-4 indicate a negligible correction is required for probe Reynolds numbers greater than 20. The estimated density, velocity and viscosity near the center of the jet are of the order of, respectively, 5×10^{-6} (Chap. 5), 2.5×10^{-4} (Ref.3-8) and 10^{-5} (Ref. 3-6) in MKS units, so the probe Reynolds number is above 300. Near the edge of the jet, however, the estimated Reynolds number drops to about 14, so the indicated pitot pressure is too high. The data near the edge of the jet are suffficiently uncertain because of measurement imprecision, making a precise correction factor meaningless. Consequently, an estimated viscosity correction was based on the empirical correction factor $1 + 5/Re$, reported in Refs. 3-4 and 3-6. Applied to the present data, this works out that 20 ± 20 N/m^2 should be subtracted from the momentum flux in the outer regions of the jet.

Yaw The axis of the impact pressure probe was maintained parallel to the jet axis, while the velocity vector direction depends on the radial position. Experience with pitot tubes has shown that the recorded stagnation pressure falls off as the yaw angle between the probe axis and the velocity vector increases. The top curve in Fig. 3-10 shows the predicted (Ref. 3-4) yaw response of a shrouded probe as a function of the yaw angle. The barred lines show the results of an attempt to experimentally verify this function for our probe by changing the probe angle but keeping the orifice location fixed on the jet centerline. The broad spread and the limited angular range of the data were a consequence of the limited space and motional control in the vacuum

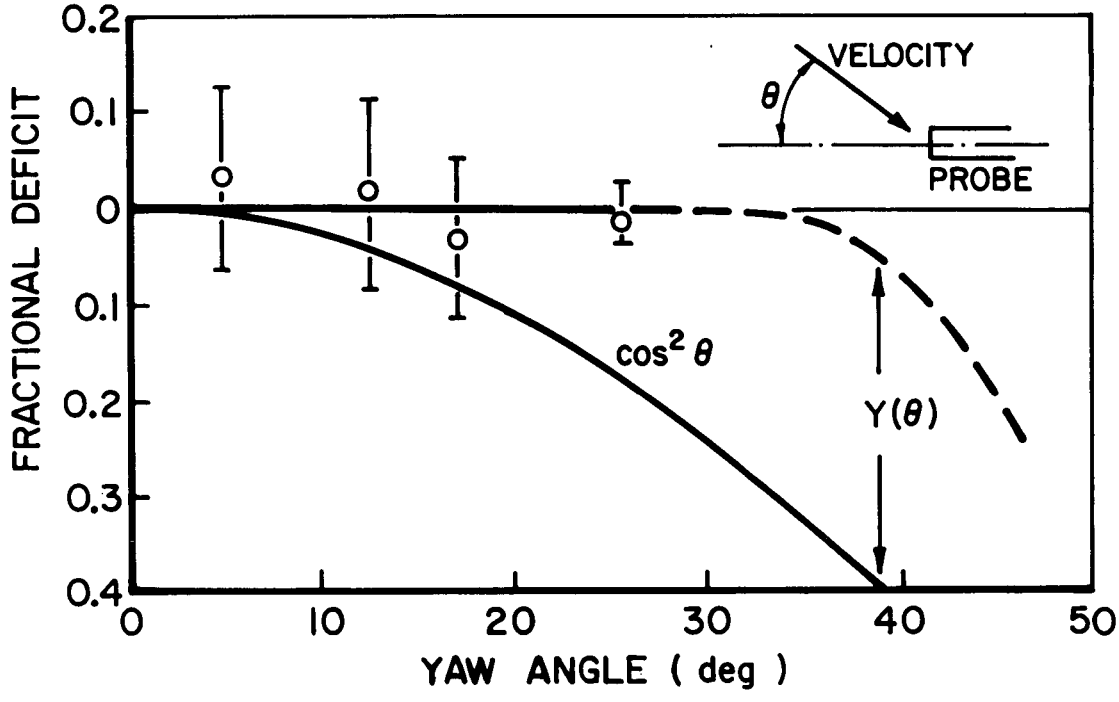

EFFECT OF YAW ANGLE (θ) ON PROBE RESPONSE TO AXIAL MOMENTUM

FIGURE 3-10

AP25 · 4721

system. Still, these data support the contention adopted that the yaw response is given by the upper curve.

Tensor With the yaw correction, the calculated momentum flux is the magnitude of the flux tensor $P = p\overleftrightarrow{I} + \rho\overleftrightarrow{uu}$. This is the quantity of momentum in the $\vec{u}$ direction which flows per second through an area perpendicular to $\vec{u}$. The axial component ($\hat{z}$) of this flux tensor through an area with a direction $\hat{a}$ is $p\,\hat{z}\cdot\hat{a} + \rho u^2\,\hat{u}\cdot\hat{z}\;\;\hat{u}\cdot\hat{a}$ where the "$\wedge$" symbol indicates a unit vector. Only the axial component was calculated and the integration was carried out over an area normal to the jet axis ($\hat{a} = \hat{z}$), so only the flux element $P_{zz} = p + \rho u^2\cos^2\theta$ (where $\hat{u}\cdot\hat{z} = \cos\theta$) was of interest. Since the static pressure (especially near the jet edges where $\cos^2\theta$ is significant) is small, the term $(1-\cos^2\theta)p$ was neglected and the tensor element P_{zz} calculated from the relation

$$P_{zz} = \left|\overleftrightarrow{P}\right| \cos^2\theta$$

This conversion factor is also plotted as the lower curve in Fig. 3-10. In practice, the yaw and tensor corrections were calculated simultaneously by using the difference between the two curves on Fig. 3-3, $Y(\theta)$, times the measured impact pressure. Fortunately, the uncertainty in this correction is principally associated with $\theta > 30^\circ$ ($R > 6$), since the yaw correction of zero for smaller angles has been well established (Ref. 3-4). For $R > 6$, the estimated uncertainty is 20% of the correction factor.

Applying these transformations to the data of Figs. 3-2, the mean, momentum flux on the centerline $P_{zz}(0) = 23 \times 10^{-3}$ atm/0.9 = 26×10^{3} atm and the mean momentum flux at R=8, $P_z(8) = (0.6\times10^{-3})(0.83)^2/0.9$ minus $20 \times 10^{-5} = 0.26 \times 10^{-3}$ atm. Using the square root of the sum of the squares to combine the uncertainties, the true mean of $P_{zz}(0)$ is expected to lie within the range 23.5 to 28.5×10^{-3} atm (5% scale, 5% supersonic, 5.8% precision, total = 8.6%). Similarly the true mean $P_{zz}(8)$ is expected to lie within the range 0.56 to -0.04×10^{-3} atm (5% scale, 5% supersonic, 114% precision, 4% yaw, 28% Re, total = 115%)

3.A.4 Integrated Momentum

The final step in data reduction, is to obtain the total momentum flow rate or thrust of the jet by integrating the flux over the jet cross-section. Axial symmetry was assumed so this integral reduces to $(2\pi RP_{zz})dR$. In this form, it is apparant that the accuracy of the radial position is just as important as accuracy of the momentum flux in determining the thrust of the jet.

Two corrections to the radial position values are required. The first correction is a consequence of the effect of the radial gradient in the momentum flux on the pitot measurement. This problem has been encountered frequently in boundary layer measurements with pitot tubes, and was studied in plasmas in the work reported in Reference 3-6. In these studies it was found empirically that the effect of an impact pressure gradient normal to the axis of the pitot tube was to shift the effective orifice center a distance $d = \sqrt{D\nabla P/P + d\nabla P}\ D/4$ toward the region of higher momentum flux. (D is the probe diameter and P the pitot pressure.) This correction, when applied to our data, resulted in a shift of at most 0.2 inches, but the effect of this shift on integrated momentum was significant since it narrowed the measured size of the jet.

Centerline Correction The second correction was required to locate the true centerline of the jet with respect to the nominal R=0 position of the platform. This was very difficult to determine beforehand using physical measurements, because the apparatus is not designed to make the platform motion along the vacuum tank axis, the alignment of the chamber and tank axis, and the chamber and jet axis alignment all accurate within the 1/4 inch required. Further, the importance of the accuracy of this measurement was not appreciated until after all of the data were collected. Consequently it was necessary to use properties of the data to make the necessary corrections.

Figure 3-11 shows the raw data prior to this correction. The integrand of the thrust integral, $2\pi RP_{zz}$, is plotted against the platform position for the six radial profiles obtained at the "standard" conditions (5.9 g/sec & 16 kA.) Of particular interest are the two sets of data connected with heavy lines in Fig. 3-11. One, (data symbol "■") is defined by the mean of 9 shots at each position (the series also used to determine reproducibility). Prior to collecting these data, the edges of the jet were approximately located and this information used to set the platform R=0 position. This set is therefore the most accurately centered data available. The other curve of particular interest (data symbol "o") is defined by the one series of measurements where special arrangements were made to extend the profile to both sides of the nominal centerline. If the jet centerline and R=0 coincided in this case, the $2\pi RP_{zz}$ curve should be symmetric about R=0. Instead, as shown on Fig. 3-11, the maximum of the "o" curve for $R < 0$ is lower and occurs at a smaller R than the standard curve ("■") and the portion of the profile for $R > 0$. A study of the behavior of $2\pi RG$, where G is a Gaussian curve, showed that these are the properties expected with this ordinate (which is the derivative of the Gaussian) with an incorrect R=0. The curve maximum will move down and to smaller R or up and to larger R depending on the direction of the error in R=0. With these properties in mind, the R=0 for the full profile curve ("o") was shifted 0.5 inches to equalize the magnitude of the maxima on both sides of the centerline. This also caused the radial location of the maxima to coincide with that of the "■" curve at about 2.2 inches. This confirmed that the correction was successful and necessary. Next, the remainder of profiles were similarly adjusted so that the radial location of their maxima were also at 2.2 inches. This required, at most, an adjustment of 3/4 inches. The corrected data for the five profiles are plotted in Figure 3-12. All data in this display lie close to the standard data, as they should since all are measurements at the same mass flow rate and current. The scatter can be completely explained by the uncertainties previously noted.

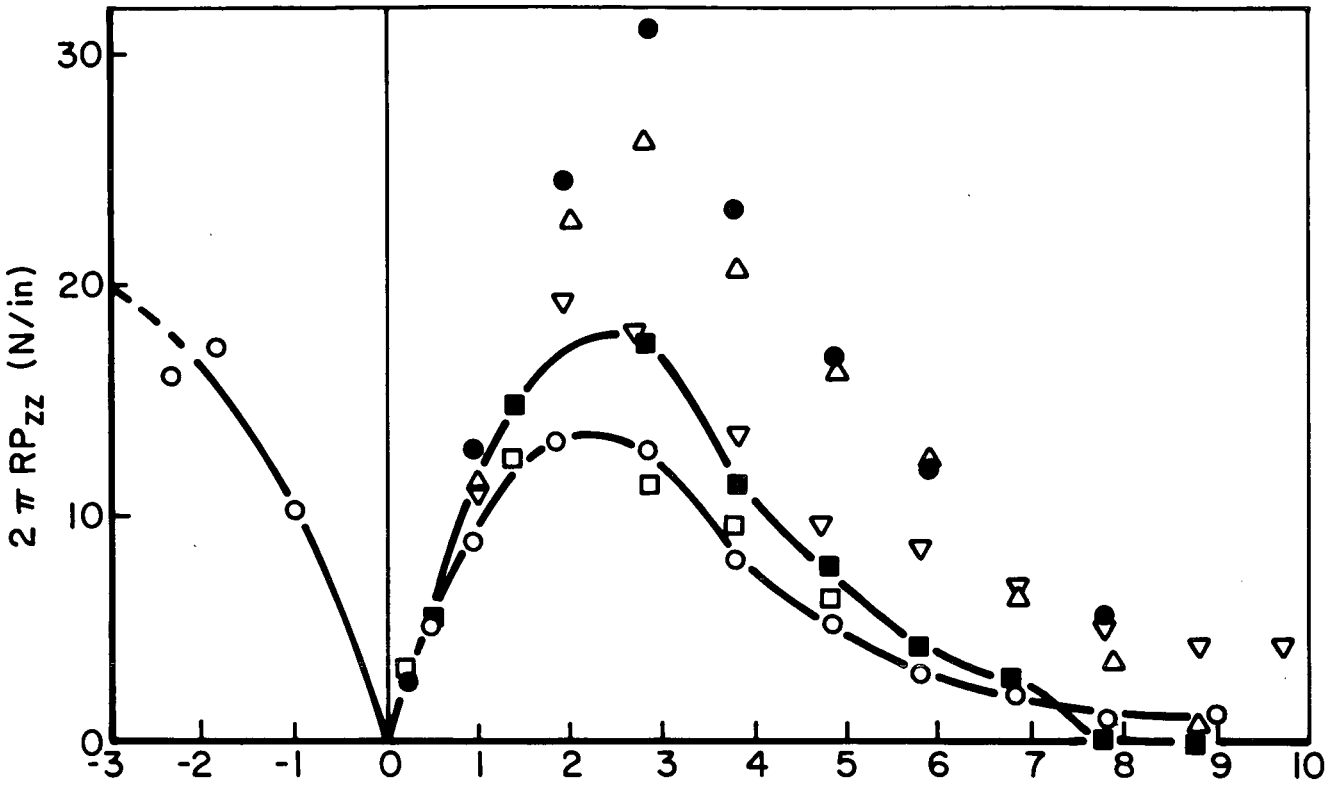

RAW DATA THRUST PROFILE DERIVATIVES

FIGURE 3-11

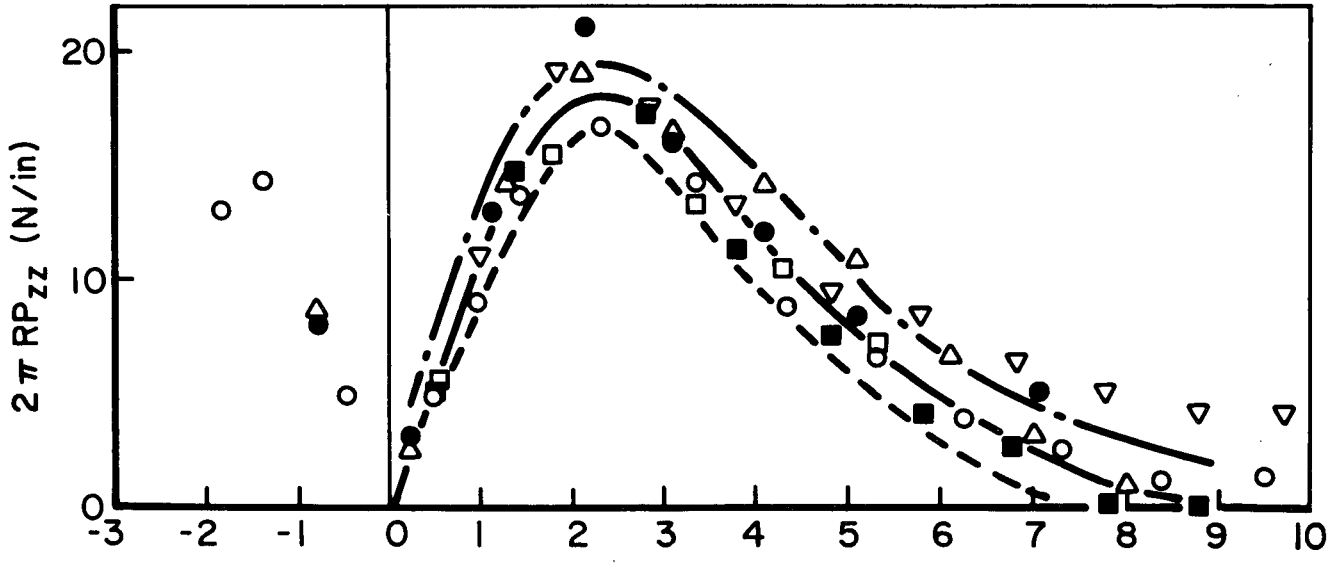

ADJUSTED ℄ THRUST PROFILE DERIVATIVES

FIGURE 3-12

Finally, this correction was applied to the profiles at other mass flow rates and currents. Fortunately, it was found by checking back through the lab notebook, that most of these were taken after a standard condition run ("▽") that had required no correction. The probe had not been disturbed between this "▽" run and the 8 subsequent runs so no correction was applied to the R=0 for these profiles. One of the remaining immediately followed a standard condition run "●", so the centerline correction was known. The final profile, taken at 36 g/sec and 38 kA, was immediately followed and preceded by removal of the probe, so no guide to the correction required was available. The location of the $2\pi RP_{zz}$ maximum indicated a correction of 1/2 inches, so this correction to the R=0 was used and the limits of uncertainty increased correspondingly in reporting the thrust.

Precision An error analysis of the integration of the profiles show two compensating effects. The uncertainty of each point used to calculate the thrust is increased by the uncertainty in R. This is easily appreciated by considering the thrust integrand, $2\pi RP_{zz}$. In analyzing the data, an uncertainty in R of ± 1/8 inch was assumed. On the other hand, the profiles form a pattern, so a least squares fit of the profile would reduce the uncertainty of the integrated thrust. Rather than actually using a least squares fit, the same effect was achieved (with a mathematical complexity more in keeping with the rest of the precision analysis) by drawing a smooth mean curve through the mean of each point. Then the sum of all point uncertainties was added to half the sum of the squares of the variations of the mean points from the curve, and the square root of this sum divided by the number of points in the profile to give an uncertainty in the ordinant of the mean curve. The two limiting curves were drawn and graphically integrated to give two values of thrust, which are expected to bracket the value of the true thrust in the jet. The mean and limiting curves are shown on Fig. 3-12.

CHAPTER 4
CHAMBER PRESSURE

The pressure in the arc chamber of the MPD accelerator was measured using a static pressure tap in the side wall. Sources of systematic error in the measurement were identified and compensated. Data were obtained for five nominal mass flow rates over a range of arc currents from 8 to 50 kA. With the aid of several assumptions, the aerodynamic or electrothermal component of thrust was calculated from the chamber pressure and the ratio of electrothermal to electromagnetic thrusts obtained as a function of $\dot{m}$ and I.

4.1 Apparatus

Figure 4-1 shows the apparatus used to measure chamber pressure. The probe described in Chapter 2 is used as the sensor in a ½ inch ID pressure tap in the chamber wall. The hole and its surroundings were painted with reflecting paint to reduce the amount of radiant heating of the piezoelectric crystal by the arc. A rubber band, pendulum support for the probe and the hole clearance (3/8 inch probe in a 1/2 inch hole) isolated the sensor from acoustic noise. Fast response was obtained by mounting the pressure sensitive face of the probe 1/8 inch from the interior chamber wall. The residual acoustic, electromagnetic, electrostatic and thermal noise was measured by blocking the static pressure tap with mylar tape backed with aluminum foil. This also blocked the thermal noise caused by arc chamber radiation, but this type noise could be separately identified on the total signal responses.

Arc current and the terminal voltage were measured for each shot with the Rogowosky coil and Tektronix voltage probe described in Chapter 2. The arc current history was traced by the upper beam of the oscilloscope and recorded on the same photograph as the pressure history. The terminal voltage history was recorded with a second scope and camera.

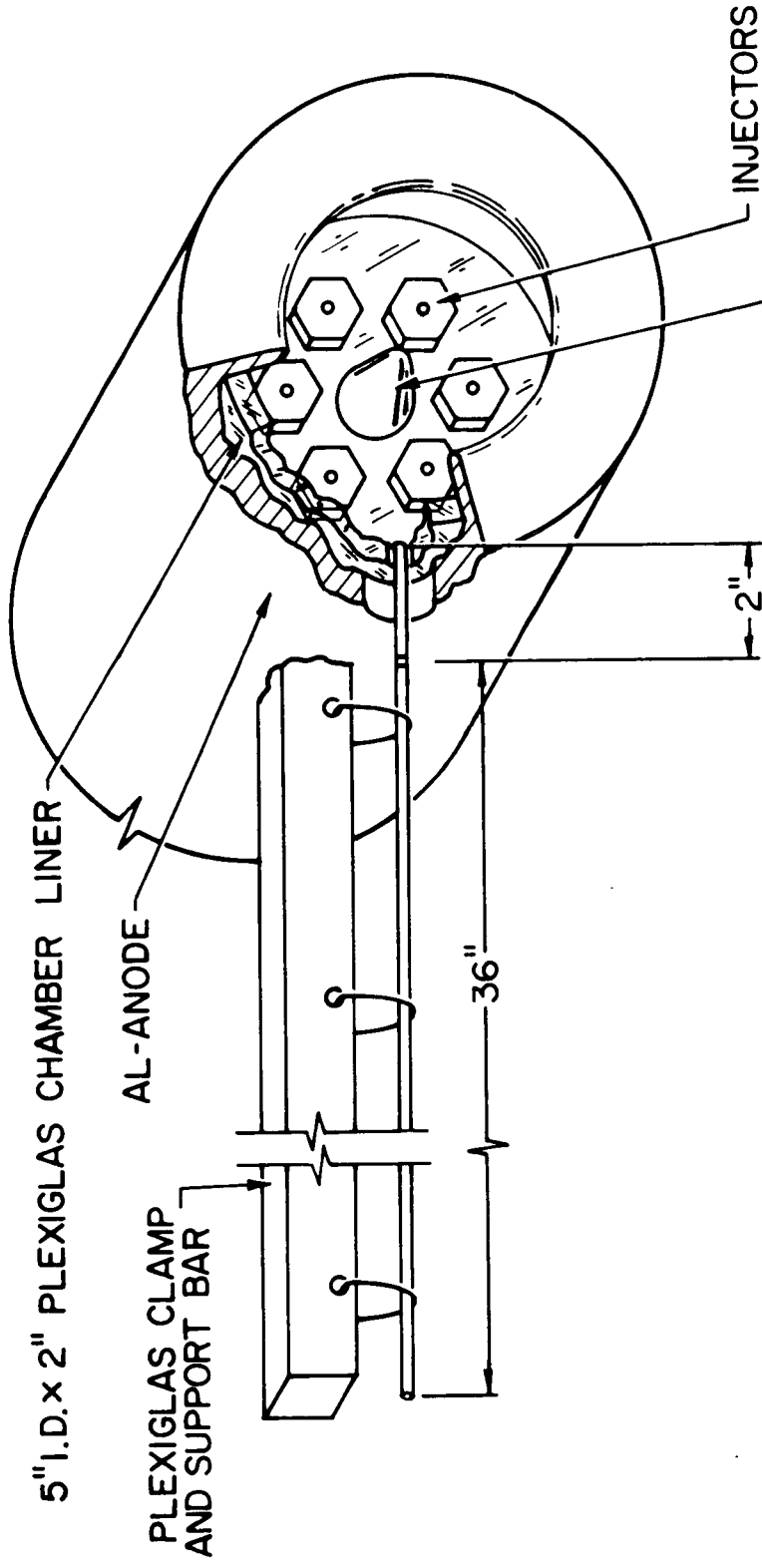

FIGURE 4-1
AP25·4743

4.2 Data Analysis

The data analysis followed essentially the same pattern as that used to reduce the impact pressure measurement: 1) scaling, 2) noise elimination and selecting a representative time, 3) static pressure tap corrections to get chamber pressure and, 4) calculating the electrothermal thrust component. Steps 1 and 2 were essentially identical so just the salient points are given below. Steps 3 and 4, however, are discussed in detail since the procedures for reducing static pressure data differ significantly from procedures for reducing impact pressure data.

4.2.1 Scaling

Figure 4-2 shows a typical data record of the chamber pressure (lower trace) and arc current (upper trace) histories. The current scale shown was derived from the Rogowsky coil calibration of 1.53 kA/mV and the pressure scale from the pressure probe calibration of 6.3 V/atm.

4.2.2 Precision, Noise and Time

The precision of the chamber pressure measurements was not formally determined. Successive shots (Figs. 4-2 and 4-3) showed that shot-to-shot variations were sufficiently low (compared to other uncertainties) to be neglected.

The noise was measured by blocking the static pressure tap with tape so it was necessary to open the vacuum system between signal and noise shots. Consequently, noise was recorded on a separate photograph from the chamber pressure data. Figure 4-4 shows such a noise record corresponding to the chamber pressure data shown in Figs. 4-2 and 4-3. The bottom trace on Fig. 4-3 has been manually scratched on the photograph to show the net pressure history, obtained by point by point subtraction of the (Fig. 4-4) noise from Fig. 4-3.

The time selected on each oscilloscope photograph as representative of the quasi-steady phase, was determined by the type and amount of noise present. For most photographs, the time

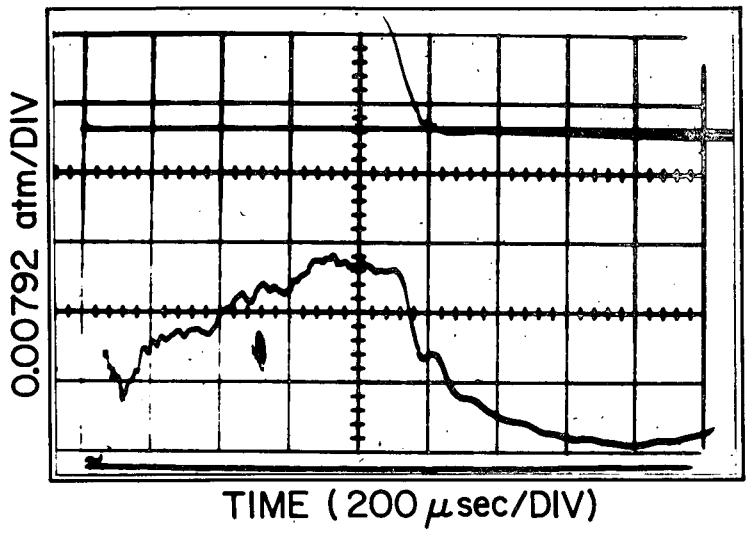

FIGURE 4-2

ARC CURRENT AND CHAMBER PRESSURE HISTORY

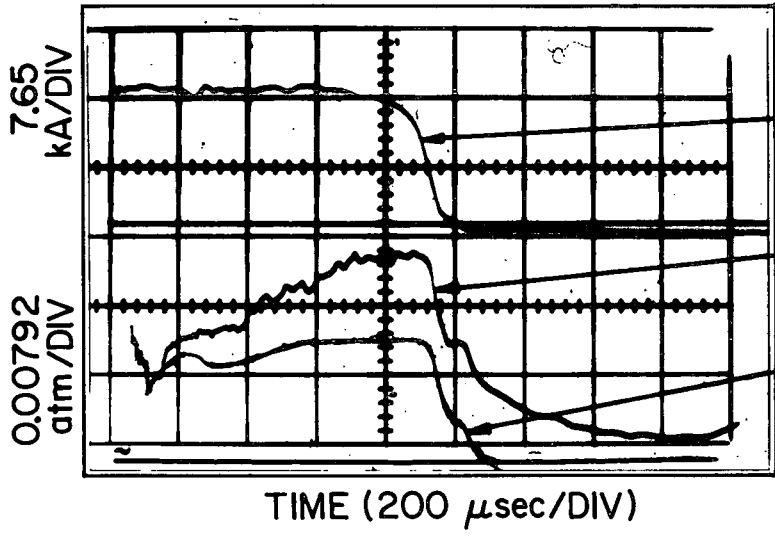

FIGURE 4-3

REPEAT SHOT NOISE MANUALLY SUBTRACTED

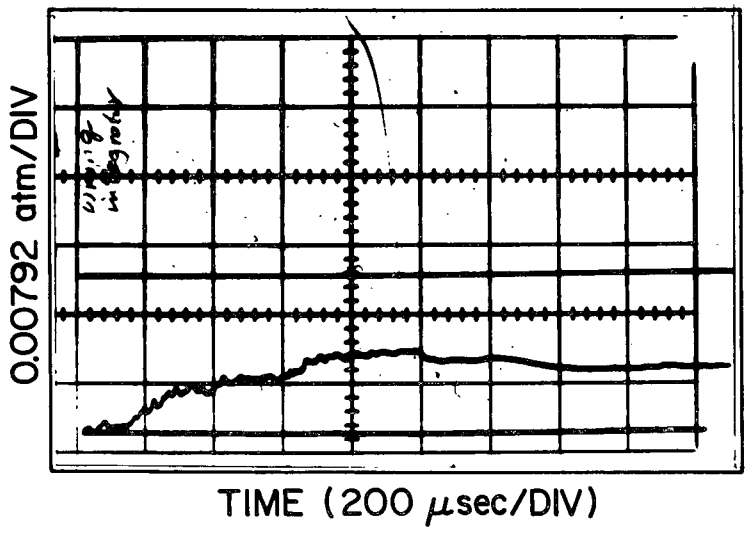

FIGURE 4-4

CHAMBER PRESSURE NOISE

selected was 350 μsec after the start of the current pulse. The initial 25 μsec no-signal portion of the trace established the zero pressure base line.

4.2.3 Static Pressure Corrections

Normally there is little question that a static pressure tap measures the local free stream pressure (Ref. 4-1). Some experimental check of this point seemed desirable, however, because of the presence of electromagnetic acceleration in the chamber as well as the inevitable gas leakage in the annular space between the 3/8 inch probe and the 1/2 inch hole. Consequently, repetitive measurements were taken to determine the effect of blocking the annular space with plastic sponge, and moving the probe to different positions along the hole axis. The pressure indication did not change when the sponge completely blocked leakage around the probe. Acoustic noise increased considerably, but changes in pressure indication of greater than about 10% would still have been detectable.

Measurements of the chamber pressure also showed no change with the face of the pressure sensor located at five different positions relative to the interior surface of the chamber. The positions were with the probe face: protruding 1/8 inch into the chamber; flush with the chamber interior surface, and withdrawn 1/8",2/8",and 3/8"back into the hole. This insensitivity to changes in the chamber boundary indicates the absence of rapid flow or strong pressure gradients which would have required further static pressure corrections.

4.2.4 Electrothermal Thrust

The contribution of gasdynamic forces to the total thrust of the MPD accelerator is the vector integral of the normal pressure over all solid surfaces plus the vector integral of the viscous forces over the same surfaces. Measurement of these forces as a function of position is beyond the scope of this work. Instead, several drastic but reasonable assumptions were made to provide a plausible estimate of the force exerted on the plasma by the surfaces of the arc chamber.

The first assumption was that the viscous forces were negligible. In MKS units, the hot plasma viscosity is less than 10^{-5} (Ref. 4-3), the velocity about 10^4 (Ref. 4-2) so with a 1 mm boundary layer the viscous force would be less than $10^{-2} N/cm^2$. Since the surface areas are tens of cm^2, and the total thrust of the order of 100 N, the assumption of negligible viscous loss seems reasonable.

The second assumption was that the pressure on the chamber walls was uniform. Some support for this assumption was offered by the experiments described in Section 4.2.3 which indicated the ionizing current near the wall did not generate rapid flow or high pressure gradients. The current pattern in the arc chamber (Ref. 4-2) indicates any pressure difference along the anode walls due to jxB forces would be concentrated near the walls and would have been detected by these experiments. The details of the plasma flow are not known, but it seems reasonable that flow pressure gradients in the volume behind 80% of the current connecting the chamber walls will be small since the flow area is large and the jxB accelerating forces are small.

The final assumption is that the force exerted on the 200 cm^2 front face of the anode is negligible. This assumption is justified by the experimental measurements of the plasma density and temperature in Ref. 4-4. The maximum density on the face of the anode is about $10^{20}/m^3$, so even with an ion temperature of 5 eV, the force would be less than 2 Newtons, quite small compared with the 100 N total thrust.

4.3 Results

Figure 4-3 shows that, as in the case of the terminal and field measurements, the chamber pressure enters a quasi-steady mode after an initial starting transient. The duration of the transient agrees well with the duration of the terminal voltage and magnetic field transients.

Figure 4-5 shows a typical data photograph from a survey of chamber pressure as a function of mass flow rate and current. Each of the lower traces represent a single shot at the current shown in the corresponding upper trace. All data on a single

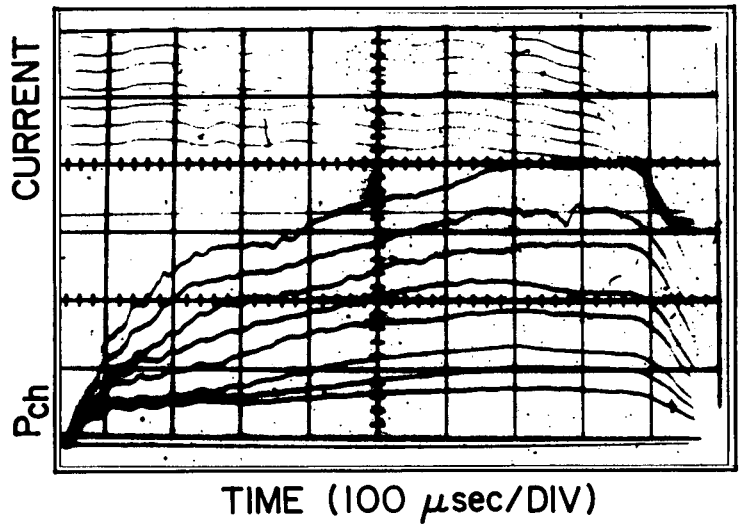

SURVEY OF P_{ch} AS A FUNCTION OF ARC CURRENT

FIGURE 4-5

AP25 · P·400

photograph are obtained using a single mass flow rate. Figure 4-6 summarizes all of this chamber pressure survey data. On this figure, each of the data traces has been reduced to a single chamber pressure value by the methods of Section 4.2 and is plotted vs. the arc current (I) using five symbols to differentiate between the five different mass flow rates ($\dot{m}$). Immediately apparent from Figure 4-6 is that chamber pressure is strongly related to arc current and much more weakly dependent on mass flow rate.

To express these relationships empirically, a least squares fit to the data for each $\dot{m}$ was used to find that chamber pressure scaled as $(I)^{1.54}$ for all mass flow rates. Each chamber pressure measurement data point was then divided by $I^{1.54}$ to eliminate the arc current dependance, and the resulting numbers plotted vs. $\dot{m}$ as shown in Fig. 4.7. The dots in this figure represent a single datum, and the "X"'s the mean at each mass flow rate condition. This plot shows that the $\dot{m}$ dependence of chamber pressure is weak, but unambigious. Again a least squares fit to the data was used to express an empirical relation for chamber pressure (P_{ch}) in MKS units of

$$P_{ch} = 3.02 \pm 0.05 \times 10^{-3} \quad (I)^{1.54} \quad (\dot{m})^{0.294}$$

Where the precision limits indicate the range of the mean value of $P_{ch}/I^{1.54} \dot{m}^{0.294}$ within 95% confidence limits. Note, however, that a least squares fit does not prove the exponents are exactly the values given.

The electrothermal thrust component (T_{et}) expected with these chamber pressures, is (using the assumptions discussed in Section 4.2.4) the chamber pressure times the throat, or anode orifice area of 81 cm^2. Using the empirical relation above (and rounding off the exponents) this calculation gives an electrothermal thrust (in MKS units)

$$T_{et} = 2.45 \times 10^{-5} \; I^{1.5} \; \dot{m}^{0.3}$$

or numerically, the electrothermal thrust varies from 5 to 100 N over the range of I and $\dot{m}$ investigated.

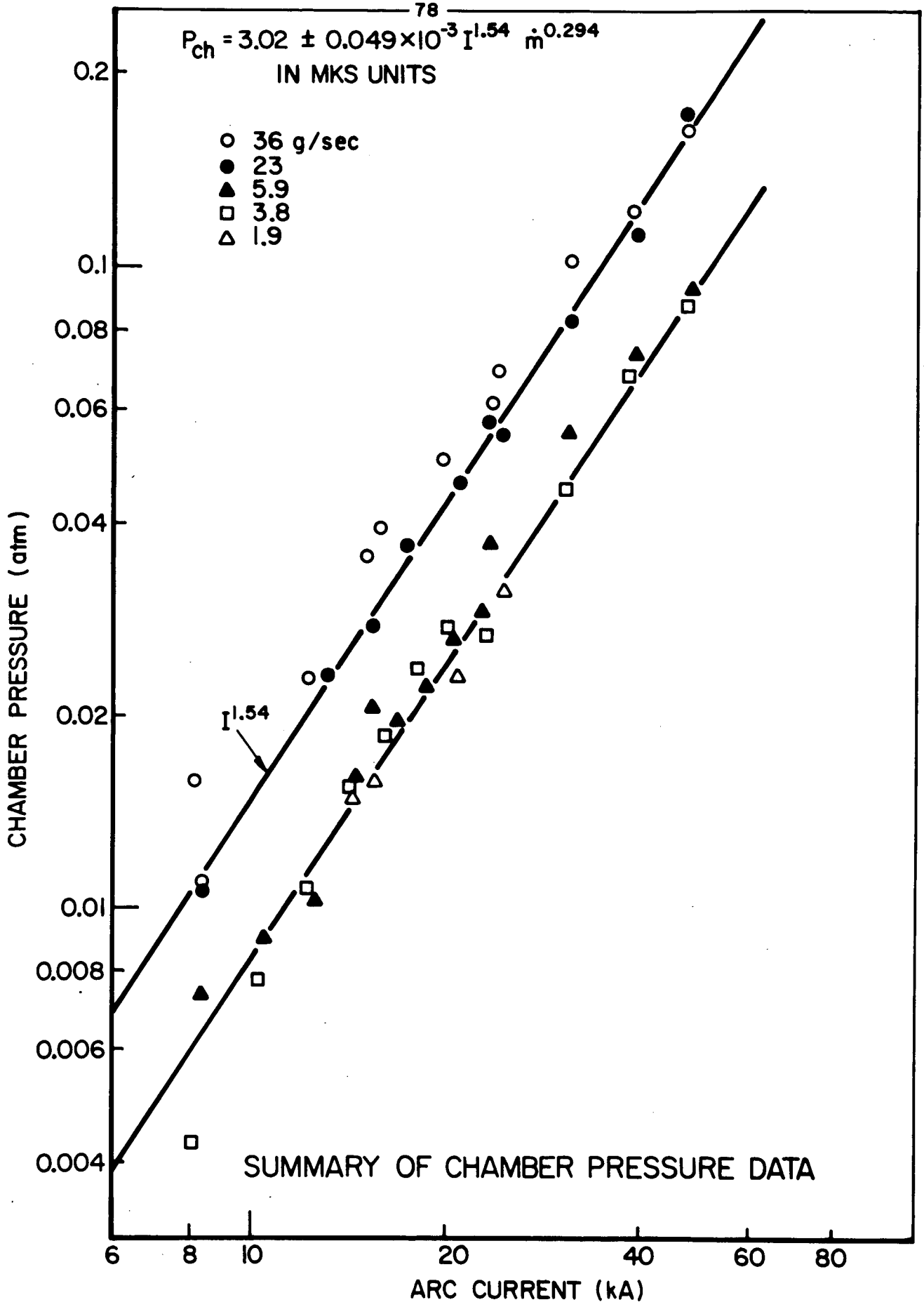

FIGURE 4-6

AP25-4739

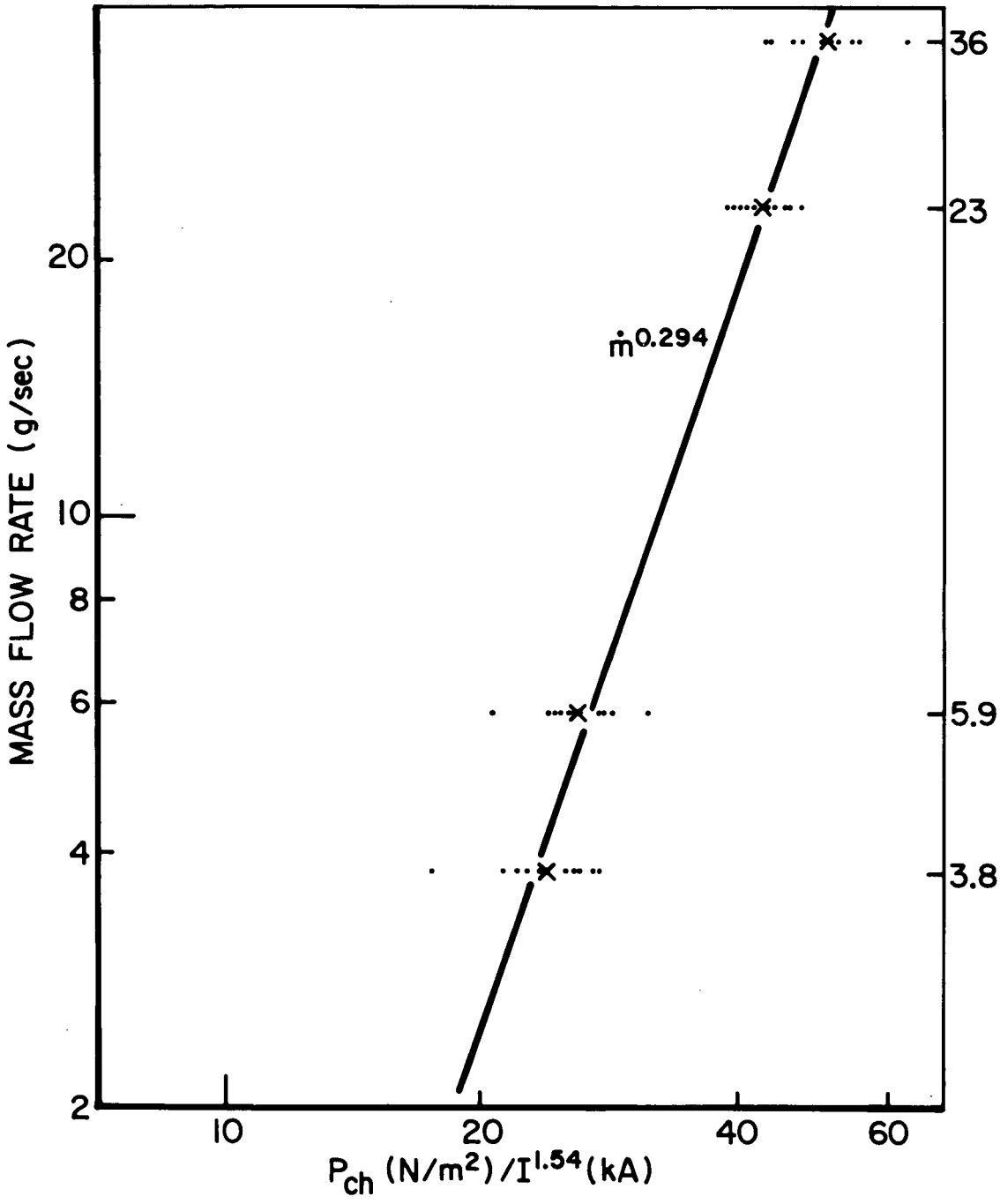

FIGURE 4-7

AP25-4742

The above data provides an answer to the long standing question concerning the electrothermal fraction of the total thrust of the MPD accelerator. For each of the total thrust measurements reported in Fig. 3-7, this ratio was calculated using the corresponding electrothermal thrust from the data on Fig. 4-6. This ratio is plotted in Fig. 4-8 as a function of the parameter I. Over the entire range of parameters investigated, about 20% of the thrust is caused by plasma pressure on the chamber walls.

A plausible reason for this fraction to remain nearly constant is given by an extrapolation of the data using the empirical relation developed above. Assuming (as verified in Chapter 5) that the total thrust is the sum of the electrothermal and electromagnetic $\mu_o I^2 (\ln r_a/r_c + 3/4)/4\pi$ components, the fraction (F) of electrothermal to total thrust is given by

$$F = \frac{2.45\text{X}10^{-5} \; I^{1.5} \dot{m}^{0.3}}{2.4\text{X}10^{-7} I^2 + 2.45\text{X}10^{-5} I^{1.5} \dot{m}^{0.3}}$$

$$= 1 + \left[\frac{(I^2/\dot{m})^{1/4}}{100 \; \dot{m}^{0.05}} \right]^{-1}$$

This relation is also plotted in Fig. 4-9 and suggests that the range of $I^2/\dot{m}$ covered by the experiments was not sufficient to show large changes in the fraction F. This relation also predicts the arcjet-to-MPD transition which was the original reason for the interest in the fraction F.

It is interesting to note the presence of the parameter $I^2/\dot{m}$ in the equation for F. This parameter also appears prominently in the best available theory of MPD accelerator operation (Ref. 4-7), which is based on a minimum principal. The theory has not yet been developed to the point where a direct comparison with the experiments is possible, but the appearance of the $I^2/\dot{m}$ is encouraging.

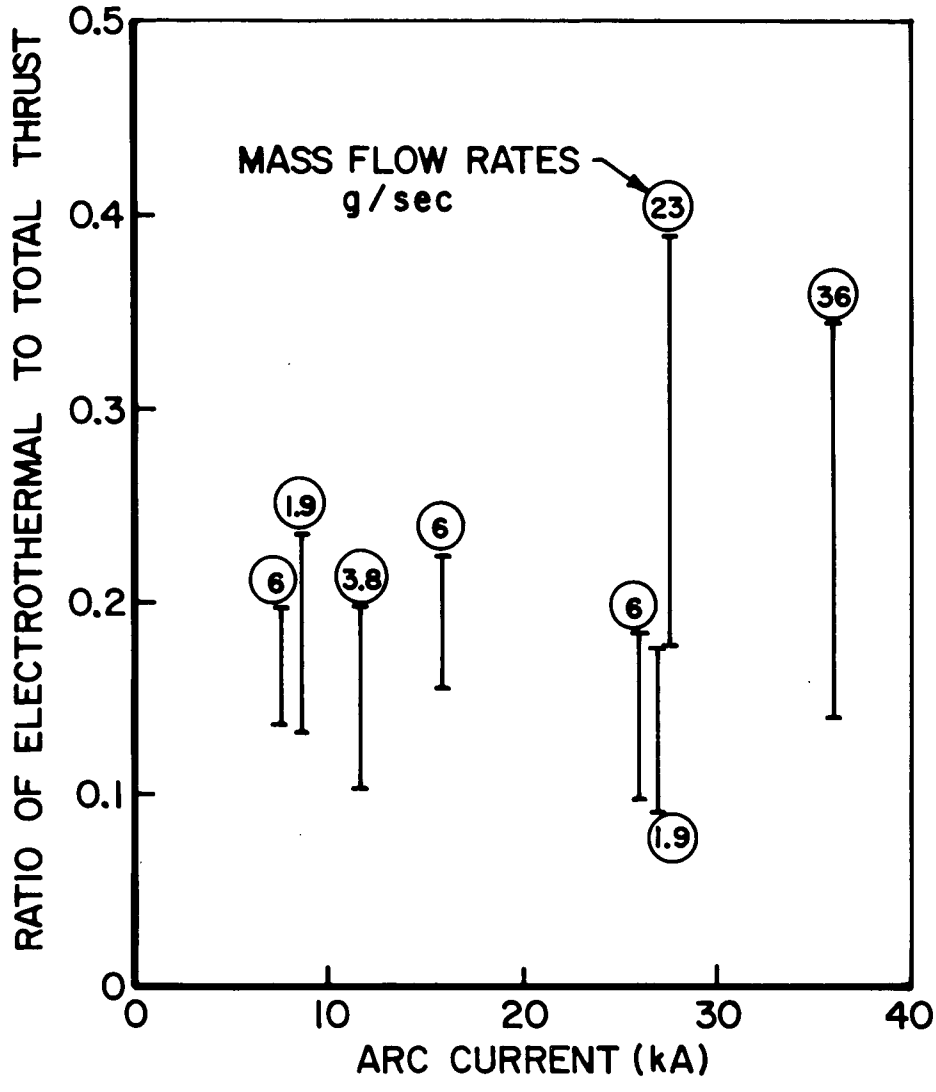

ELECTROTHERMAL CONTRIBUTION

FIGURE 4-8

AP25·4740

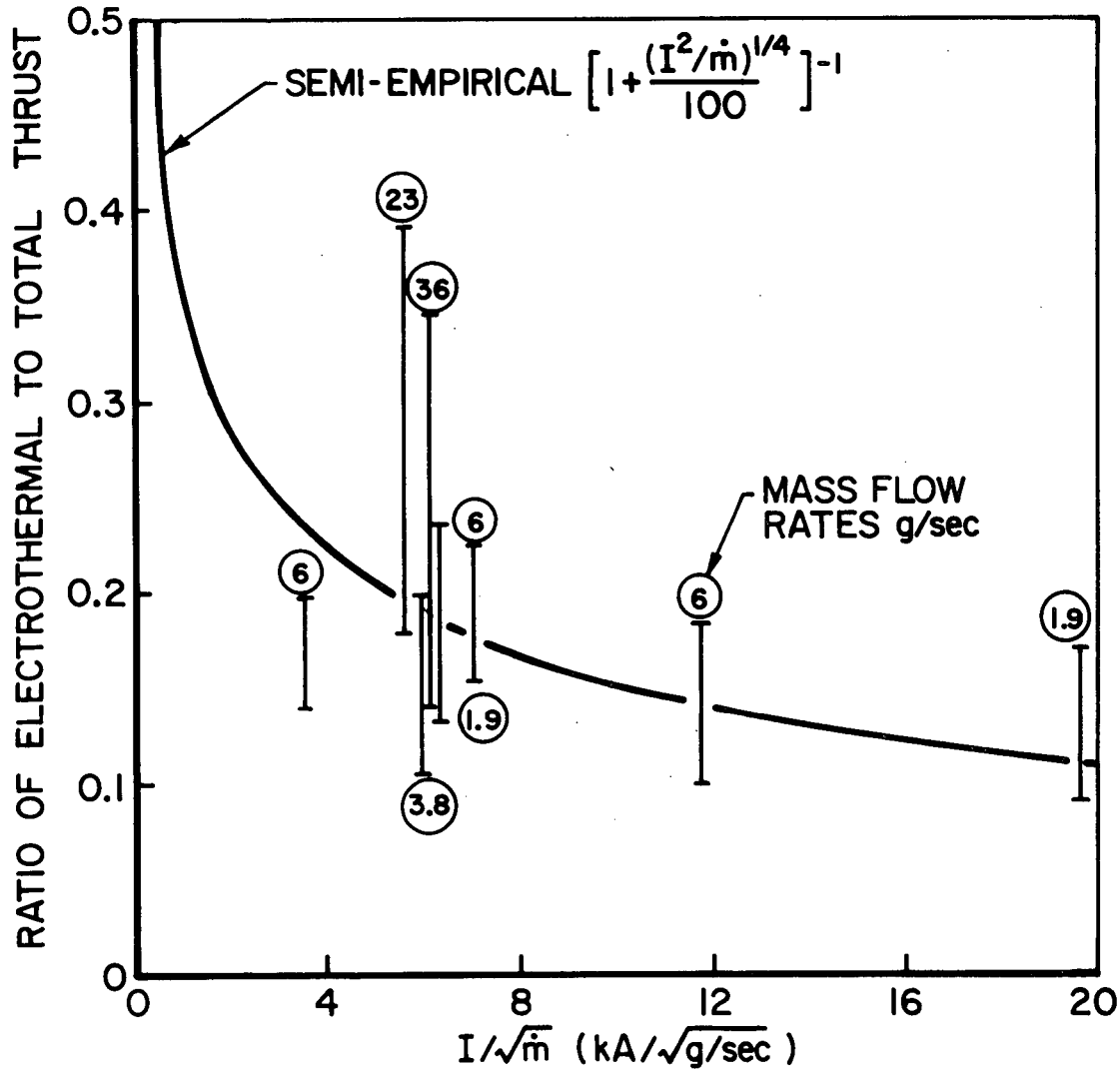

RATIO OF ELECTROTHERMAL TO TOTAL THRUST

FIGURE 4-9
AP25 · 4741

CHAPTER 5

MASS, MOMENTUM AND ENERGY FLOW

The measurements reported in Chapters 3 and 4 combine with earlier data to provide a major increase in our knowledge of mass, momentum and energy flow from the MPD accelerator. Since the momentum flux is ρu^2, dividing by the local velocity (Ref. 5-1) gives the mass flux profile of the jet. The integral over this profile compared with the total inlet mass flow rate (Ref. 5-2), shows appreciable mass is bypassing the jet. The calculated electromagnetic thrust (Ref. 5-3) plus the measured electrothermal thrust (Chap. 4) equals the jet axial momentum content (within the accuracy of the data of Chapter 3) indicating the major sources and sinks of momentum have been identified and measured. The energy of streaming motion is ρu^2 times ½ the velocity, so the spatial distribution of this major fraction of the total energy flow is identified, providing a basis for improved estimates of the remaining energy sinks.

The engineering implications of this knowledge of mass, momentum and energy flow follow immediately. The mass utilization efficiency (60%), specific impulse (1400 sec), thrust efficiency (21%) and other engineering parameters describing the performance of the accelerator as a space thruster are easily calculated. More important, the position and time resolved information shows the reason for the particular values of the performance parameters. This, in turn, suggests what must be done to improve performance and provides clear directions for an experimental development program.

5.1 Mass Flow

Figure 5-1 shows the axial mass flux profiles at 11 and 5 inches from the anode which are produced by an arc current of 15.6 kA and a mass flow rate to the accelerator of 5.9 g/sec. The data reported in this figure were calculated by dividing the total momentum flux taken from the smoothed curves discussed in Chap. 3 by the velocity taken from the profiles of Fig. 5-2, (see

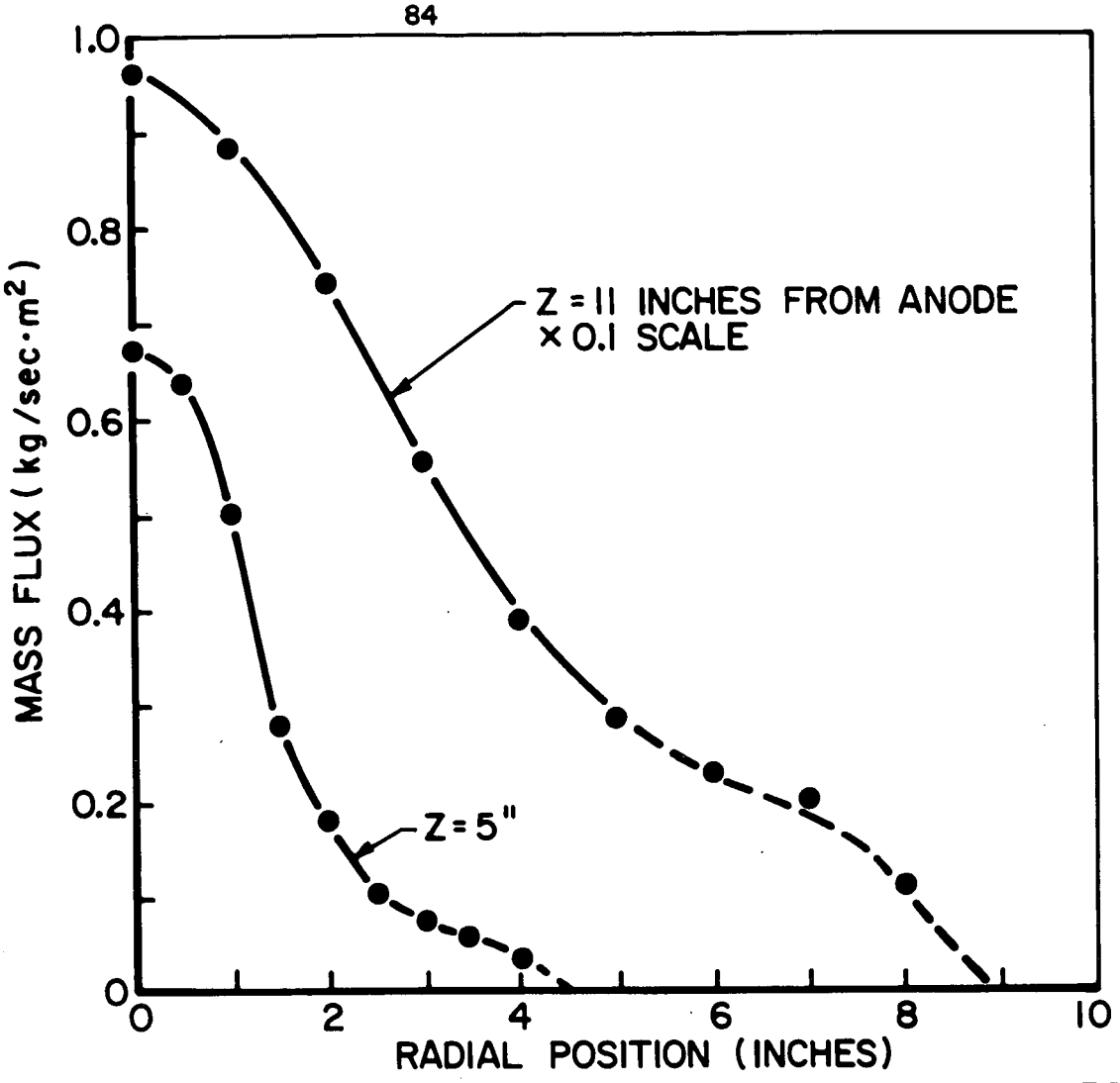

AXIAL MASS FLUX PROFILE FIGURE 5-1

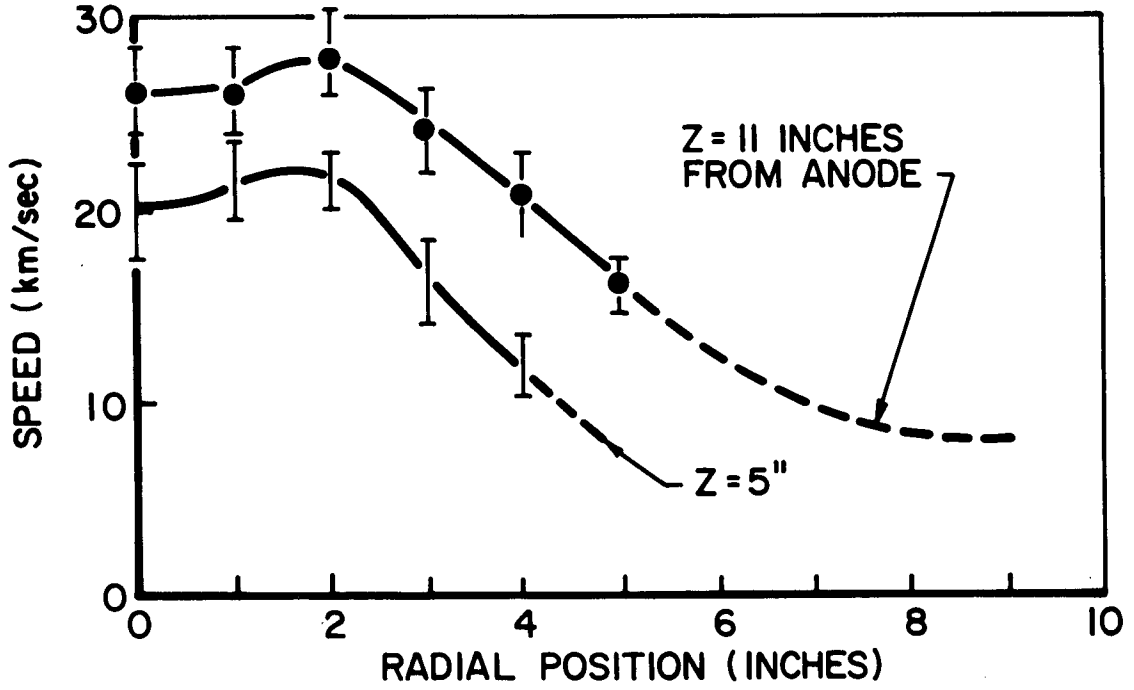

VELOCITY PROFILE FIGURE 5-2

Ref. 5-1) at each point and multiplying by the cosine of the velocity vector. This method for calculating mass flux is based on the assumptions: 1) that the Mach number is high, so the impact pressure ($P_{static} + \rho u^2$) was primarily ρu^2; 2) that the velocity vector pointed from the center of the anode, and 3) that the extrapolation of the velocity profile shown as a dotted line in Fig. 5-2 is valid. A quantitative calculation of the uncertainty introduced by these assumptions proved to be infeasible, so the accuracy of the mass flux reported in Fig. 5-1 is unknown. A "best judgement" is that the mass flux is correct to 20% near the centerline and 50% near the edge of the jet since the sensitivity to uncertainties in momentum and velocity is linear (eg. 10% error in velocity implies 10% error in mass flux).

Figure 5-3 illustrates one of the most informative ways of displaying the mass flow data. The mass flux profile was graphically integrated (using $2\pi R$ as a weighting factor as

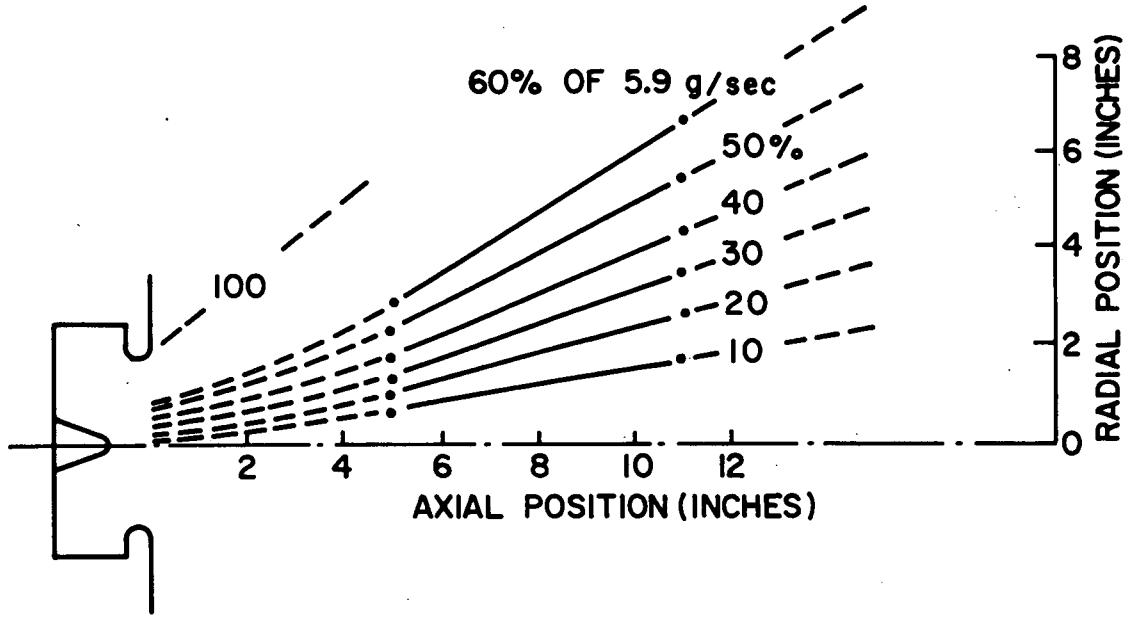

MASS FLOW STREAMLINES

FIGURE 5-3

discussed in Chap. 3) from R=0 to R. The radial positions for which this integral was 10% through 60% of the nominal inlet mass flow rate are plotted in Fig. 5-3 for the two axial positions. Points representing the same percentage define the mass streamlines, which are labledin Fig. 5-3 with the fraction of the (nominal) total mass flowing in the conical volume bounded by the streamline.

The data as displayed in Fig. 5-3 indicate the steady state mass utilization is poor. Only 60% of the mass carries appreciable momentum and only a central core moves at the highest velocity (see Fig. 5-2). This conclusion, if true, is so important to a thruster development program, that it is worthwhile to consider the supporting evidence in detail.

The value for the inlet mass flow rate is the most questionable of the data indicating poor mass utilization. The nominal value used in the calculations was obtained by a choked orifice, mass flow rate calculation (Ref. 5-2). The accuracy of this calculation is unknown, since it was based on a reasonable but nevertheless assumed reservoir temperature of 230°K and a reservoir pressure measurement that was probably subject to considerable acoustic and heating noise (see Chap. 2). An attempt to check this cold flow $\dot{m}$ is illustrated in Fig. 5-4. These data were obtained by blocking the anode orifice to provide a known limited volume receptacle for the inlet mass flow and used the chamber pressure measurement arrangement (Fig. 4-1) to measure the time rate of increase in the chamber pressure caused by the cold gas flow. The mass flow rate ($\dot{m}$) in such an arrangement is the time rate of change of density (ρ) multiplied by the chamber volume (V) so the measured dP/dt and the desired $\dot{m}$ are related by

$$dP/dt = RT\dot{m}/V + \rho RdT/dt.$$

Again the temperature is not known so the mass flow rate calculation depends on an assumption. Assuming, however, that the chamber temperature is not a function of time and is γ times the assumed shock tube reservoir temperature of 230°K, the data of

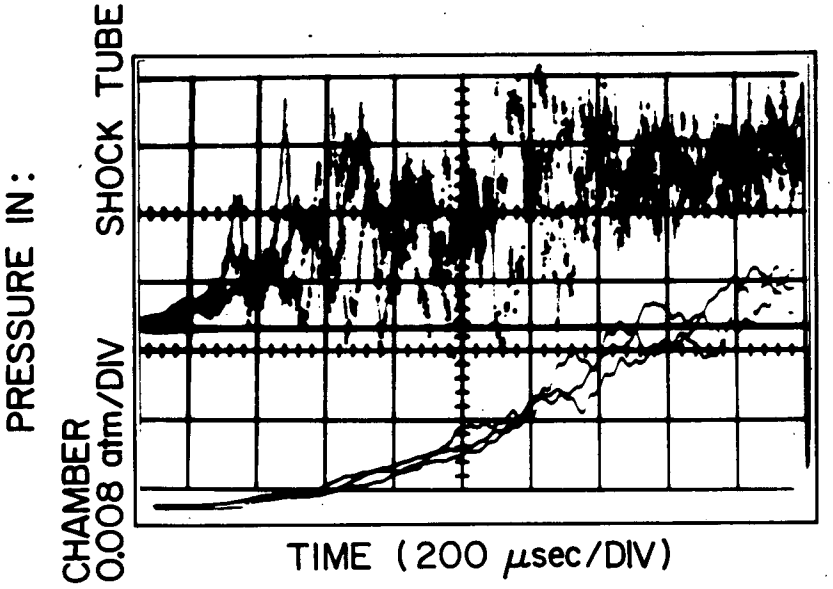

COLD FLOW CHAMBER PRESSURE RISE

FIGURE 5-4
AP25-P-402

Fig. 5-4 indicate a mass flow rate of 15 g/sec. This estimate, then, suggests the mass utilization is even worse than shown on Fig. 5-3. Similarly any corrections due to mass ablation from the chamber walls, or injestion by the jet from ambient plasma (Chap. 3) will make the calculated mass utilization even worse.

The velocity profiles as shown in Fig. 5-2 are based on time-of-flight measurements and also may contain some systematic error. If the velocity were lowered as suggested by Doppler shift measurements (Ref. 5-4), the calculated mass in the jet would be larger and the mass utilization better. The Doppler shift measurements, however, measure mass averaged velocities, so the values reported in Ref. 5-4 which are much less than the peak velocity measurements reported in Ref. 5-1 tend more to support the proposition of poor mass utilization rather than dispute the peak velocities of 25 km/sec. In addition, a velocity profile sufficiently smaller (1/3) to imply the injected mass is in the jet would reduce the calculated streaming energy (Sect. 5-3) to an unreasonably low value. The velocity profile as used is probably sufficiently accurate to support the conclusion of poor mass utilization. The accuracy of the momentum measurements was discussed in Chap. 2, and a 1/3 larger momentum flux, especially near the centerline seems improbable.

On balance then, the evidence indicates an appreciable fraction of the inlet mass flow is not included in the high velocity jet. As suggested in Fig. 5-3 by the dotted line, the remaining mass probably is ejected from the 1 inch annular space between the 2 inch diameter jet and the anode lip rather than retained in the chamber. The alternate, retention of the excess mass in the chamber until the conclusion of the current pulse, should cause an increase in the chamber pressure which is not observed in the quasi-steady phase (Fig. 4-3). Also the measured chamber pressure alone (0.02 atm), without any electromagnetic acceleration, would force the missing 2 g/sec in choked flow through the 60 cm^2 annular space between the jet and the anode

lip. Either this flow exists or there is some balancing force for which no evidence has been found.

5.2 Momentum Flow

Figure 5-5 shows the axial momentum flow pattern for a nominal input of 5.9 gm/sec and an arc current of 15.6 kA. This pattern was derived from the momentum flux profiles reported in Chap. 3 in the same way as the mass flow streamlines were calculated from the mass flux profiles. That is, the weighted integral from R=0 to R of the average flux profiles at 11, 5 and 1 inches from the anode were expressed as a fraction of the total thrust, plotted against R, the radial positions for 10% through 90% crossplotted to give the points marked by an "•" in Fig. 5-5, and the points connected to define the momentum streamlines.

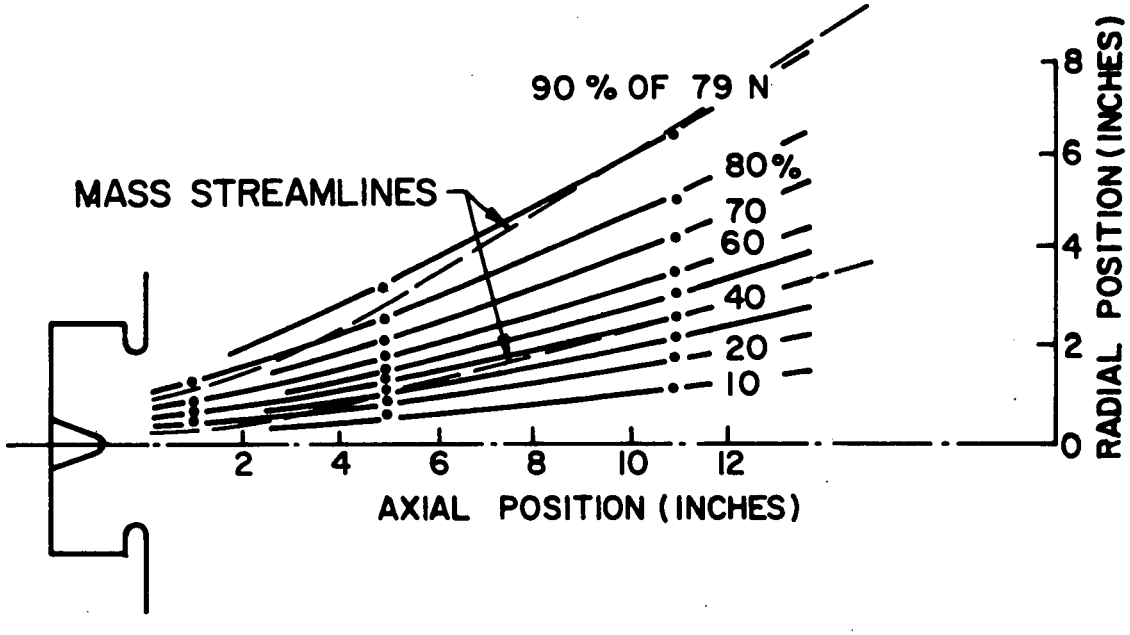

AXIAL MOMENTUM FLOW STREAMLINES

FIGURE 5-5

The slopes of the momentum streamlines in Fig. 5-5 are nearly equal to the slopes of the mass flow streamlines at the same position for Z > 7 inches, indicating negligible momentum is added after this axial position. Nearer the anode, however, the momentum streamline slopes are much less than the corresponding mass streamline slopes (i.e., the mass in a given streamline gains momentum). This shows that even after the jet has left the anode orifice, there is an appreciable increase in momentum, especially near the centerline. This observation is in agreement with and derives from the observed velocity increase along the centerline (Ref. 5-1). If this increase of momentum were strictly a consequence of the expansion of the jet into a vacuum, the momentum of the central portion would increase at the expense of the momentum content of the outer regions so the edge momentum streamlines would have a greater slope than the edge mass streamlines. Figures 5-3 and 5-5 do not show this property. They show an increase in momentum of the entire jet of about 8N or 10%, suggesting small fringing magnetic fields are still accelerating the plasma well after it leaves the anode orifice. It must be recalled, however, that the momentum flux measured near the jet edges varied over a range of 100% (Sec. 3.A.2), so the precise location and slope of the streamlines near the jet edges is uncertain. The precision of the data near the edges is not sufficient to decide between vacuum expansion or downstream acceleration as an explanation of the observed centerline velocity increase.

The total axial momentum (thrust) of 79 newtons used in Fig. 5-5 is the sum of the measured electrothermal thrust, (T_{et} as reported in Chap. 4), and the predicted electromagnetic thrust (T_{em}, Ref. 5-3). It is assumed that these two forces dominate. The close agreement between this applied force (79 N) and the total integrated axial momentum in the beam (76 N) is a strong argument for all the assumptions used to calculate these numbers and also for the accuracy of the measurements. This argument is made even stronger by considering the predicted and actual dependance of thrust on current and mass flow rate.

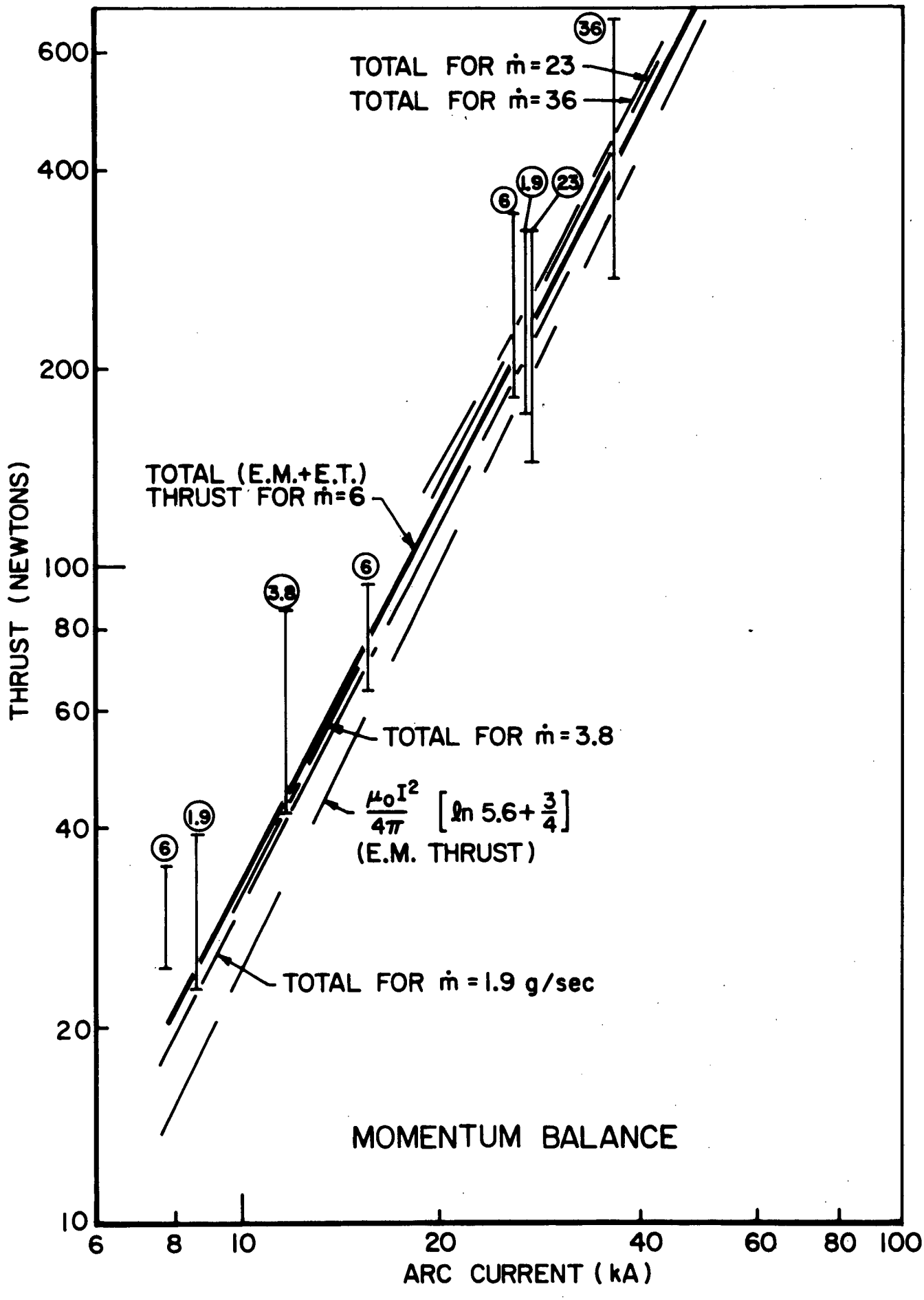

FIGURE 5-6

AP25·4749

Figure 5-6 shows the momentum balance obtained at the other mass flow rates and arc currents investigated (Table II). The barred verticle lines are reproduced from Fig. 3-7 to show the measured total axial momentum content of the jet and are labeled with the nominal mass flow rate. The lowest dashed line shows the predicted $T_{em}(I)$ which is common for all mass flow rates, and the other lines show the sum of this $T_{em}(I)$ plus the equation developed in Chap. 4. In all except one case, the total axial momentum derived from the flux profiles equals the $T_{em}(I) + T_{et}(I,\dot{m})$ within the accuracy of the data. This balance over most of the range of parameters investigated, gives added confidence in the techniques used to obtain these numbers (see Chapters 3 and 4). At the lower currents the sensitivity limit of the pressure probe was approached, and back calculations showed an easily explained (Chap. 2) systematic error of one torr would reconcile any disagreement.

5.3 Energy flow

Figure 5-7 shows the flow pattern of the total energy of motion of the plasma produced by a mass flow rate of 5.9 g/sec and an arc current of 15.6 kA. This pattern was calculated by multiplying the total momentum flux ($|\rho u|\,|u|$ taken from the smoothed curves of Chap. 3) times 1/2 the component of the velocity normal to the area of integration (Fig. 5-2), times the weighting factor $2\pi R$, integrating from R=0 to R and expressing this integral as a fraction of the total electrical energy supplied to the arc ($VI = 2.56 \times 10^6$ watts, see Fig. 5-8). This fraction was plotted against R, at the R positions corresponding to 10% through 35% cross plotted on Fig. 5-7 for Z = 5 and 11 inches, and the points connected to form flow energy streamlines. The most significant information gained by this process was that each element of the jet gained appreciable energy from Z=5 to Z=11 inches and that as much as 37% of the input power eventually appeared as directed kinetic energy.

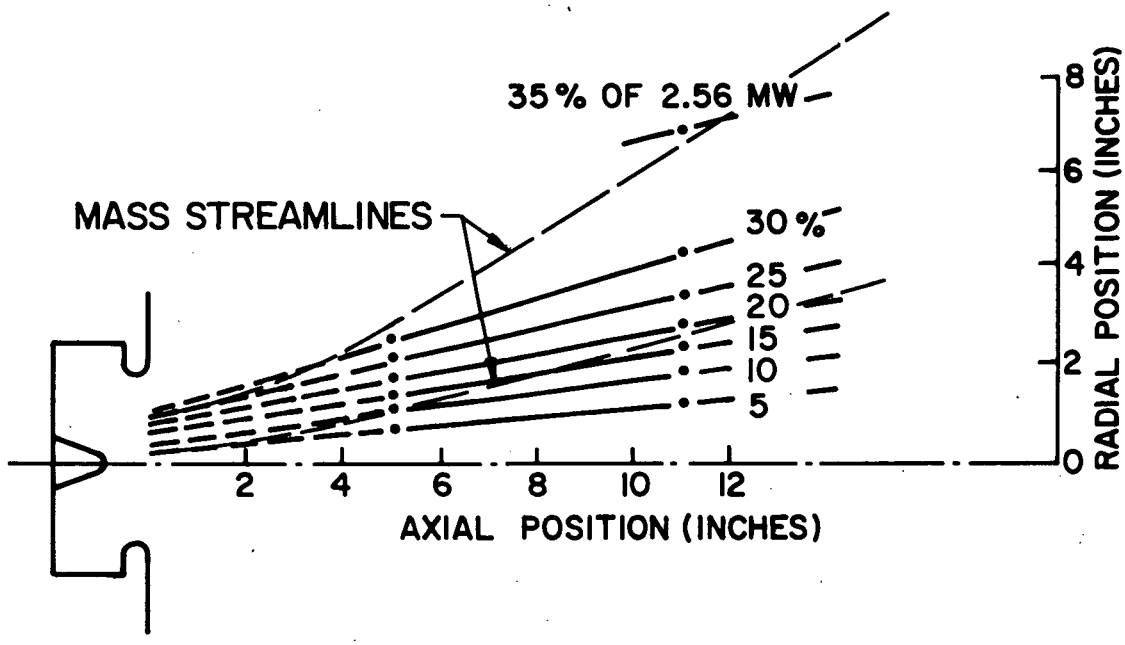

KINETIC ENERGY STREAMLINES

FIGURE 5-7

In contrast to the observed mass deficit, it is no surprise that all of the energy does not appear as kinetic energy. Losses are expected to the electrode surfaces and in ionizing, excitation and heating the plasma. Sufficient hard experimental data are not yet available to pinpoint the location of the remaining 63% of VI = 2.56 MW of input power, but with what is available and a few reasonable assumptions a fairly accurate estimate is possible. That is:

1) 11% or 0.31 MW are lost to the anode through the anode sheath voltage drop (Ref. 5-5);
2) 16% or 0.43 MW or ½ of the cathode sheath power is lost to the cathode (Ref. 5-6); and
3) 12% or 0.33 MW are lost in heating, exciting and ionizing the plasma to a 1½eV equilibrium state (Refs. 5-6,7,8).

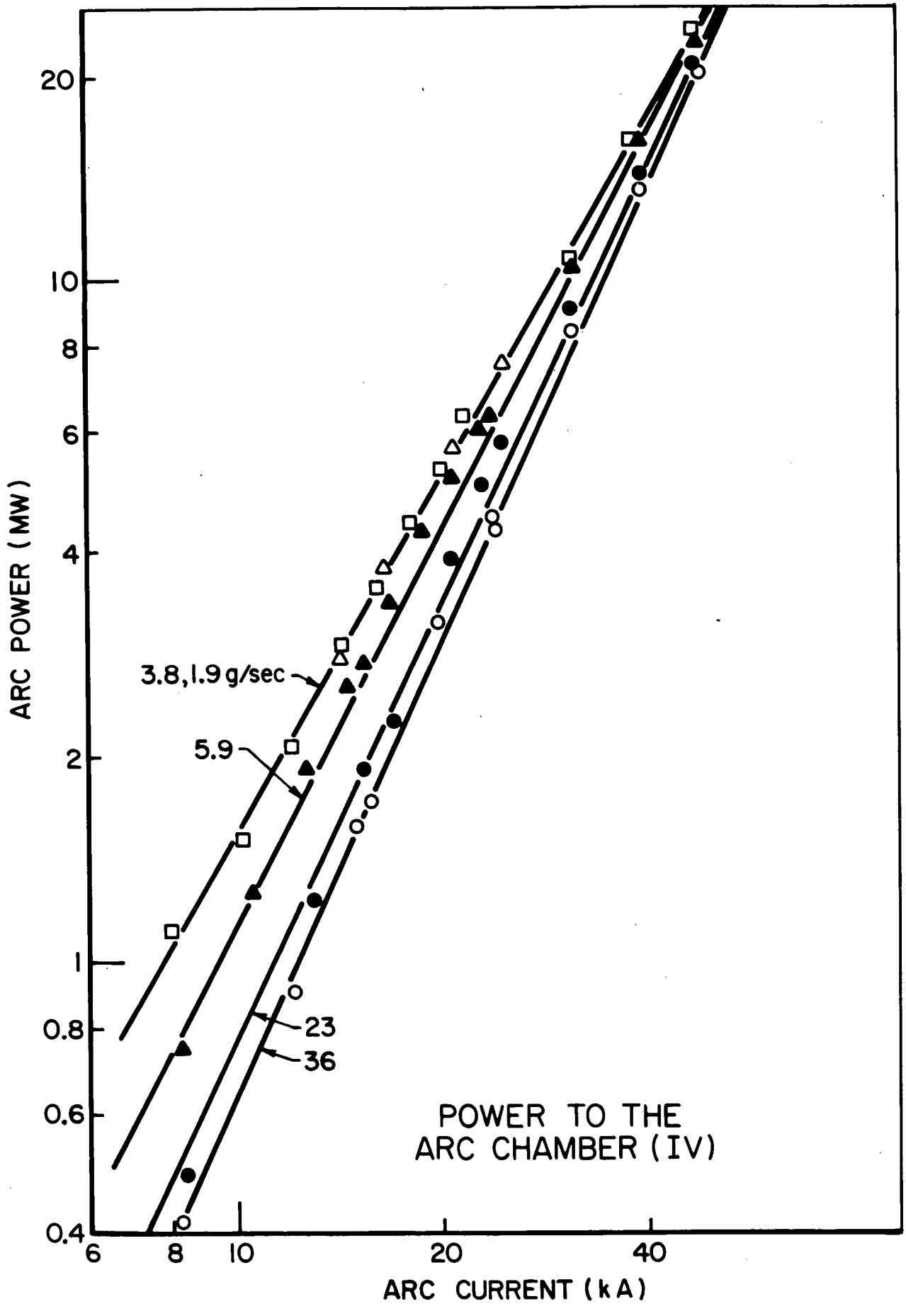

FIGURE 5-8

AP25·4748

The sum of all these estimates (40% plus the 37% of kinetic energy is only 77% of the measured input power, but this absence of an exact power balance is to be expected from the large uncertainties associated with the losses, especially the frozen flow losses of item 3, and losses (e.g. radiation) not included in the power balance.

5.4 Performance Parameters

Using the mass, momentum and flow energy profiles found above, many properties of the jet at the standard operating conditions may be calculated and used to discuss the possible mechanisms of the accelerator. The density, for instance, is $\rho u^2/u^2$, typically 4×10^{-6} kg/m^3. Also, with reasonable assumptions, such as assuming most of the ion thermal energy has been converted to flow energy at Z = 11 inches, the properties of the jet as it leaves the anode plane can be calculated to be: ion temperature = 10 eV; Re=10^4; static pressure = 0.021 atm (nearly equal to the measured chamber pressure of 0.017 to 0.021 atm); and, velocity, temperature and static pressure are nearly uniform across the jet. This in turn, implies the profile losses are low so that most (90%) of the kinetic energy (0.95 MW) contributes to useful thrust.

Most of such calculations, however, will not be particularly informative until the accuracy of the results is confirmed by validating the velocity profile and inlet mass flow rate data. Even without this validation, however, it is useful to consider the performance of the accelerator as a space thruster, since the results suggest a promising direction for thruster development which may produce significant improvements in MPD accelerator performance.

Since the discovery of the MPD accelerator, it has been known that performance calculations can be misleading. The most widely recognized error occurs at the so-called "starved" operating conditions. At low (or zero) inlet mass flow rates, an MPD accelerator still produces about the same thrust as with

higher mass flows (Chap. 3). The mass accelerated is usually ingested or mass ablated from the arc chamber surfaces. Consequently, at these conditions, quasi-steady specific impulse or, $T/\dot{m}$, and thrust efficiency, $T^2/2\dot{m}$, calculated on the basis of input mass flow rates do not represent the true performance of the accelerator as a space propulsion system. Table IV shows the performance parameters calculated on this basis, and the results for the "starved" condition I = 27 kA, and $\dot{m}$ = 1.9 g/sec illustrate the problem. An efficiency of 132% is impossible and a specific impulse of 11200 sec is improbable. Indirect methods, such as measuring the electrode and insulator mass loss, have established that ablation occurs at high currents and/or low inlet mass flow rates ("starved conditions"), but these methods are not sufficiently precise to allow reliable calculations of performance (Ref. 5-10).

The techniques developed in this chapter can be used to give a more accurate performance evaluation for the "starved" operating conditions. Using the methods outlined in Sec. 5.1, the actual mass flow rate in the jet can be calculated. Using this mass flow rate in the formula $T/\dot{m}$ will give a much more realistic value for the specific impulse of a starved MPD accelerator. The result will still be too high, however, since as shown for the standard conditions in Sec. 5.1, the mass leakage around the jet is indetectable.

A second way in which performance calculations such as Table IV are misleading, is concerned with thrust efficiency, $T^2/\dot{m}$. The thrust efficiency is commonly thought of as the fraction of the total input power which appears as useful thrust. This is the ratio of the axially directed kinetic energy flow power to electrical power or

$$\eta = 1/2 \int \rho u_z^2 \, u_z \, dA/IV$$

If the velocity and momentum flux are uniform across the jet at a point sufficiently downstream so that the static pressure

TABLE IV

Performance Parameters
Based on INPUT Mass Flow Rates
During Quasi-Steady Operation

I A	$\dot{m}$ kg/sec	T N	T/$\dot{m}$ m/sec	I_{sp} sec	$T^2/2\dot{m}$ watts	IV watts	η_t %
7.75×10^3	5.9×10^{-3}	21½	$3\frac{3}{4} \times 10^3$	3.8×10^2	0.0403×10^6	$.98 \times 10^6$	4.11
8.6	1.9	22½	11.8	12	0.133	1.2	11.1
11.7	3.8	43	11.3	11.5	0.243	2.05	13.5
15.6	5.9	79	13.4	13.7	0.54	2.56	21
	3.9*	79	20.2	20.7*	0.8	2.56	33*
26	5.9	220	37.5	38	4.13	7.2	17.4
27	1.9	210	110	112	11.5	8.7	132
27½	23	240	10.4	10.6	1.04	6.7	15.5
36½	36	450	12.5	12.7	2.86	11.0	26

* based on mass flow rate in the jet and observed profiles.

is negligible, the thrust power can be written as

$$\tfrac{1}{2}\int \rho u_z^3\, dA = \tfrac{1}{2}\int \frac{(\rho u_z^2)^2}{(\rho u_z)}\, dA \rightarrow \tfrac{1}{2}\frac{\left[\int \rho u_z^2\, dA\right]^2}{\int \rho u_z\, dA} = T^2/2\dot{m}$$

As shown in Sec. 5.3, however, the approximation of uniformity is not valid. Both the velocity and momentum flux are functions of position at Z = 11 inches from the anode. Even in the anode plane where the momentum flux is nearly uniform across the jet, there is a leakage of plasma around the jet which does not participate in the MPD acceleration process. The thrust efficiency as measured by $T^2/2\dot{m}$, therefore, is a measure not only of energy efficiency, but also gas or plasma leakage from the thruster. This is clearly misleading in a thruster development program since the procedures used to improve the efficiency with which energy is converted into useful thrust are clearly different from the procedures required to stop a plasma or gas leak. Using the measured momentum flux and velocity profiles in the integral relation above, the efficiency with which energy is converted to thrust for the standard conditions was calculated to be 33%. This is over half again as big as the value (21%) of $T^2/2\dot{m}$ for these conditions. Presumably, the $T^2/2\dot{m}$ calculation is equally misleading for all the other operating conditions listed in Table IV as well as the reported results in Refs. 5-4 and 5-8. The magnitude of the difference discovered for the standard conditions strongly suggest that the techniques developed in this chapter be used to separate the effect of leakage from MPD accelerator inefficiencies in any thruster optimization program.

5.5 Thruster Development Program

Finally, the new information gained by profile measurements shows how performance can be improved. Previous thruster optimization studies at AVCO (Ref. 5-4) have shown that thruster performance is related to the parameter $I^2/\dot{m}$. (The results of Chap. 4 give a hint as to why this should be so). Their

results indicated that for the "starved" condition, $I^2/\dot{m} > 40$ $kA^2 \cdot sec/g$, erosion was a problem, and they reasoned that for $I^2/\dot{m} < 40$, the "over-fed" condition, some of the input mass would bypass the acceleration region. The "standard" operating conditions in the present experiments were originally chosen to be "matched" ($I^2/\dot{m} \sim 40$) since the AVCO results implied this operating condition optimized thruster performance with respect to leakage and erosion. The profile studies in Sec. 5-1 show that even at this "matched" condition, about 50% of the inlet mass bypasses the acceleration region. Mass utilization is poor, reducing the specific impulse from a potential 2100 sec to 1400 sec and the thrust efficiency from a potential 33% to 21%. In this case, the profile measurements provided a more direct and accurate indication of "starved" and "overfed" conditions than provided by the $I^2/\dot{m}$ correlation and therefore a better basis for thruster optimization. This result suggests two complimentary programs for improving the thruster performance of an MPD accelerator. These are:

1) Stop the mass loss through the annular space between the jet and the anode lip. Two methods of accomplishing this suggest themselves. The anode orifice size could be reduced, as it is in the AVCO thrusters (Ref. 5-4). There is some indication that this geometry change may decrease the efficiency by increasing the terminal voltage, so it will be desirable to measure the velocity and momentum flux profiles for a series of anode orifice sizes to find the optimum geometry. Alternatively, the annular space may be blocked by an insulator. The leaking plasma velocity is apparently low velocity so erosion of the insulator may not be serious, and since the leaking plasma apparently does not participate in the MPD acceleration process, the insulator may not degrade efficiency. The key point in using this or similar techniques for improving mass utilization is recognizing the problem and measuring the result of any geometry modification.

2) The goal of the second program would be to find the optimum operating conditions for a given geometry. This would require measurement of the velocity and momentum flux profiles (as well as $\dot{m}$, I, V and erosion) over a range of $\dot{m}$ and I. Using the techniques outlined in this chapter, the true specific impulse, efficiency and mass utilization would be calculated at each operating condition. From this information, the optimum thruster operating conditions for any specified mission could be calculated.

In view of the large inefficiencies detected by the investigation described in the preceding chapters, either or both of these thruster development programs could reasonably be expected to produce a major improvement in MPD thruster performance.

REFERENCES

[1-1] Richter, R., "Development of a 30 KW Three Phase AC Arc Jet Propulsion System," NASA CR-54112 (1964).

[1-2] Kerrebrock, J. L., "Electrode Boundary Layers in Direct Current Plasma Accelerators," J. Aerospace Sci., 28, p. 631 (1961).

[1-3] Clauser, M. U., "Magnetohydrodynamics," Space Technology, Wiley & Sons, N. Y. (1959).

[1-4] Bostick, W., "Plasma Motors," Advan. Astronaut. Sci., Vol. 2, pp. 2-1, Am. Rocket Soc. Plenum Press, Inc., N. Y., (1957).

[1-5] Cann, G. L., et al., "Hall Current Plasma Accelerator," AIAA J., 2, p. 1234, (1964).

[1-6] Zukoski, E. E., et al., "Experiments Concerning Non-Equilibrium Conductivity in a Seeded Plasma," AIAA J., 2, p. 1410, (1964).

[1-7] Ducati, A. C., et al., "Experimental Results in High Specific Impulse Thermionic Acceleration," AIAA J., 2, p. 1452, (1964).

[1-8] Jahn, R. G., Physics of Electrical Propulsion, McGraw-Hill, (1968), p. 196f.

[1-9] Esker, D. W., et al., "Radiation Cooled MPD Arc Thruster," NASA CR 72557 (1969).

[1-10] Malliaris, A. C., "Quasi-Steady MPD Propulsion at High Power," NASA CR-111872 (1971).

[1-11] Clark, K. E., "Quasi-Steady Plasma Acceleration," NASA Grant NGL-31-001-005, Report 859 (Princeton University, AMS Dept., Thesis 1969).

[1-12] Turchi, P. J., "The Cathode Region of a Quasi-Steady MPD Arcjet," NASA NGL-31-001-005, Report 940 (Princeton University, AMS Dept., Thesis, 1970).

[1-13] Oberth, R. C., "Anode Phenomena in High Current Discharges," NASA NGL-31-001-005, Report 961 (Princeton University, AMS Dept., Thesis, 1970).

[1-14] Jahn, R. G., et al., "Acceleration Patterns in Quasi-Steady MPD Arcs., AIAA J., 9, pp. 167-172, (Jan. 1971).

REFERENCES

2-1 Clark, K. E., "Quasi-Steady Plasma Acceleration," NASA Grant NGL-31-001-005, Report 859 (Princeton University, AMS Dept., Thesis 1969).

2-2 Jahn, R. G., et al., "Pulsed Electromagnetic Gas Acceleration," NASA NGL-31-001-005, Report 634o, Jan. 1970, pp. 32-36.

2-3 Turchi, P. J., "The Cathode Region of a Quasi-Steady MPD Arcjet," NASA-NGL-31-001-005, Report 940 (Princeton University, AMS Dept., Thesis, 1970).

2-4 Oberth, R. C., "Anode Phenomena in High Current Discharges," NASA-NGL-31-001-005, Report 961 (Princeton University, AMS Dept., Thesis, 1970).

2-5 Koeppendorfer, W., "Induction Coils as Detectors for Fast High Current Discharges," (Translation) Institute for Plasma Physics, Munich-Garching (1961).

2-6 "Piezoelectric Technology Data for Designers". Issued by Clevite (1965).

2-7 York, T. M., "Pressure Distribution in the Structure of a Propagating Current Sheet," NASA Research Grant NGL-31-001-005, Report 853 (Princeton University, AMS Dept., Thesis, 1968).

2-8 Jahn, R. G., et al., "Pulsed Electromagnetic Gas Acceleration," NASA Contract NGL-31-001-005, 16th Semi-Annual Report 634o, (June 1970), pp. 60-73.

2-9 Shapiro, A. H., The Dynamics and Thermodynamics of Compressible Fluid Flow, Vol. 1, Ronald Press, 1953, p. 123.

2-10 Huddlestone, R. H. and Leonard, S. L., Plasma Diagnostic Techniques, (Academic Press 1965), p. 53f.

REFERENCES

3-1 Boyle, M. J., "Plasma Velocity Measurements with Electric Probes," (Princeton University, AMS Dept., B.S. thesis 1969).

3-2 Shapiro, A. H., The Dynamics and Thermodynamics of Compressible Fluid Flow, Vol. 1, Ronald Press, 1953, p. 154.

3-3 Volluz, R. J., Handbook of Supersonic Aerodynamics, Section 20, Wind Tunnel Instrumentation and Operation. NAVORD Report 1488, Vol. 6 (U. S. Govt. Printing Office, 1961).

3.4 Ladenburg, R. W. ed., High Speed Aerodynamics and Jet Propulsion, Volume IX, Princeton University Press, 1954, pp. 111-123.

3-5 Devoto, R. S., "Transport Coefficients of Partially Ionized Argon," Phys. Fluids, 354-364, (1967).

3-6 Voropayev, A. A., "Measurement of Plasma Flow Rate with a Head Pressure Pipe," Translation in NASA-TT-F-12768 (1970).

3-7 Clark, K. E., "Quasi-Steady Plasma Acceleration," NASA Grant NGL-31-001-005, Report 859 (Princeton University, AMS Dept., Thesis 1969), p. 76.

3-8 Jahn, R. G., et al., "Acceleration Patterns in Quasi-Steady MPD Arcs," AIAA J., 9, pp. 167-172, (Jan. 1971).

3-9 Jahn, R. G., Physics of Electric Propulsion, (McGraw-Hill, 1968), p. 244.

3-10 Malliaris, A. C., et al., "Quasi-Steady MPD Propulsion at High Power," NASA CR-111872, (1971).

3-11 Malliaris, A. C., "Plasma Acceleration in an Electrical Discharge by the Self Induced Magnetic Field," J. Appl. Phys., 38, (1967), pp. 3611-3619.

3-12 Turchi, P. J., "The Cathode Region of a Quasi-Steady MPD Arcjet," NASA NGL-31-001-005, Report 940 (Princeton University, AMS Dept., Thesis, 1970).

REFERENCES

[4-1] Volluz, R. J., Handbook of Supersonic Aerodynamics, Section 20, Wind Tunnel Instrumentation and Operation. NAVORD Report 1488, Vol. 6, (U.S. Govt. Printing Office, 1961), p. 4.

[4-2] Turchi, P. J., "The Cathode Region of a Quasi-Steady MPD Arcjet," NASA NGL-31-001-005, Report 940 (Princeton University, AMS Dept., Thesis, 1970), pp. 59,77,82.

[4-3] Devoto, R. S., "Transport Coefficients of Partially Ionized Argon," Phys. Fluids, 354-364, (1967).

[4-4] Oberth, R. C., "Anode Phenomena in High Current Discharges," NASA NGL-31-001-005, Report 961 (Princeton University, AMS Dept., Thesis, 1970), p. 125.

[4-5] Turchi, P. J., "The Cathode Region of a Quasi-Steady MPD Arcjet," NASA NGL-31-001-005, Report 940 (Princeton University, AMS Dept., Thesis, 1970), p. 137.

[4-6] Jahn, R. G., Physics of Electrical Propulsion, McGraw-Hill (1968), pp. 240-246.

[4-7] Malliaris, A. C., et al., "Quasi-Steady MPD Propulsion at High Power," NASA CR-111872 (1971).

REFERENCES

[5-1] Jahn, R. G., et al., "Acceleration Patterns in Quasi-Steady MPD Arcs," AIAA J., 9, pp. 167-172 (Jan. 1971).

[5-2] Clark, K. E., "Quasi-Steady Plasma Acceleration," NASA Grant NGL-31-001-005, Report 859 (Princeton University AMS Dept., Thesis 1969), p. 109.

[5-3] Jahn, R. G., Physics of Electrical Propulsion, (McGraw-Hill, 1968), pp. 240-246.

[5-4] Malliaris, A. C., et al., "Quasi-Steady MPD Propulsion at High Power," NASA CR-111872 (1971), p. 43f.

[5-5] Oberth, R. C., "Anode Phenomena in High Current Discharges," NASA NGL-31-001-005, Report 961 (Princeton University, AMS Dept., Thesis, 1970), p. 98.

[5-6] Turchi, P. J., "The Cathode Region of a Quasi-Steady MPD Arcjet," NASA NGL-31-001-005, Report 940 (Princeton University, AMS Dept., Thesis, 1970), p. 90f.

[5-7] Bruckner, A., Princeton University, AMS Dept., Ph.D. Thesis (To be issued in late 1971).

[5-8] Mollier Chart for Argon, Published by EOS, Prepared under AF33(657) - 7940.

[5-9] Jahn, R. G., Physics of Electrical Propulsion, (McGraw Hill, 1968), p. 101.

[5-10] Esker, D. W., et al., "Radiation Cooled MPD Arc Thrusters," NASA CR 72557 (1969).

[5-11] Apostol, F. M., Mathematical Analysis, Addison-Wesley, (1957), p. 20.